USC
UNIVERSIDADE DE SANTIAGO DE COMPOSTELA

CENTRO INTERNACIONAL DE ESTUDOS
DE DOUTORAMENTO E AVANZADOS
DA USC (CIEDUS)

TESE DE DOUTORAMENTO

MICROSTRUCTURING OF MATERIALS WITH LASER TECHNOLOGIES FOR BIOMEDICAL APPLICATIONS

María de la Inmaculada Aymerich López

ESCOLA DE DOUTORAMENTO INTERNACIONAL

PROGRAMA DE DOUTORAMENTO EN LÁSER, FOTÓNICA E VISIÓN

SANTIAGO DE COMPOSTELA

ANO 2019

DECLARACIÓN DA AUTORA DA TESE

Microstructuring of materials with laser technologies for biomedical applications

Dna. María de la Inmaculada Aymerich López

Presento a miña tese, seguindo o procedemento axeitado ao Regulamento, e declaro que:

1) A tese abarca os resultados da elaboración do meu traballo.
2) De selo caso, na tese faise referencia ás colaboracións que tivo este traballo.
3) A tese é a versión definitiva presentada para a súa defensa e coincide coa versión enviada en formato electrónico.
4) Confirmo que a tese non incorre en ningún tipo de plaxio doutros autores nin de traballos presentados por min para a obtención doutros títulos.

En Santiago de Compostela, 29 de abril de 2019

Asdo María de la
Inmaculada Aymerich
López

AUTORIZACIÓN DO DIRECTOR/TITOR DA TESE

Microstructuring of materials with laser technologies for biomedical applications

Dna. María Teresa Flores Arias

INFORMA:

Que a presente tese, correspóndese co traballo realizado por Dna. ***María de la Inmaculada Aymerich López****, baixo a miña dirección, e autorizo a súa presentación, considerando que reúne os requisitos esixidos no Regulamento de Estudos de Doutoramento da USC, e que como director desta non incorre nas causas de abstención establecidas na Lei 40/2015.*

En Santiago de Compostela, 29 de abril de 2019

Asdo María Teresa
Flores Arias

AGRADECIMIENTOS

Esta tesis, fruto del trabajo de varios años, no hubiera sido posible sin la ayuda y el respaldo de muchas personas a lo largo de esta época. Solamente puedo comenzar estas líneas mencionando a Maite Flores, mi directora de tesis. Gracias por todo su apoyo y su confianza en mi, por guiarme siempre con buen criterio a lo largo de este proyecto, por su esfuerzo y dedicación y por esos cinco minutos que siempre es capaz de encontrar para escucharme, aún cuando su día tiene más trabajo que horas. Siempre he sido consciente de la suerte que he tenido al haber trabajado en este grupo de investigación y de tener, sin ninguna duda, la mejor jefa posible. Tengo que dar las gracias también al resto de investigadores del grupo Photonics4Life. En especial, a Carmen Bao por ayudarme siempre que lo he necesitado y por haber podido disfrutar de la experiencia de impartir docencia a su lado; y a Justo Arines por su continuo buen humor.

Y cómo no, gracias a mis compañeros de despacho. A Manu por todos sus "sabías que", anécdotas y confabulaciones; a Ferran por toda la red de espionaje que tenemos montada; y a Ángel, que sé que algún día me hará estrella de cine. Aunque ya no estemos todos juntos, siempre serán las personas por las que ir a trabajar se convierte en algo divertido.

Gracias también a todos los miembros, pasados y actuales, del USCOSA Student Chapter por haber podido participar y divertirme en tantas actividades de divulgación que hemos hecho, recorriendo media ciudad y parte de los alrededores con las gafas de difracción y los ositos de gominola.

Al empezar esta etapa no pensaba que acabaría aprendiendo tantas cosas sobre temáticas tan alejadas de mi carrera y por ello le doy las gracias a todas aquellas personas que se implicaron en enseñarme. Gracias a los grupos de investigación de Cardiología y Oncología Traslacional del Instituto de Investigación de Santiago. En especial a Ezequiel Álvarez, por su paciencia al enseñar a una física a trabajar con cultivos celulares y por luchar juntos contra tantas burbujas que nos iban apareciendo; y a Miguel Abal por su ayuda y sus consejos para mejorar. Gracias también al Grupo de Física No Lineal de la USC y a Alberto Muñuzuri, por todo su apoyo en el análisis de fluidos y en todo este proyecto.

A lo largo de estos años he tenido la suerte de poder realizar experimentos en varios laboratorios. En particular, gracias a Silvia Soria del IFAC-CNR por la estancia en Florencia. Gracias también a todo el grupo de Aplicaciones del Láser y la Fotónica de la Universidad de Salamanca por su acogida esas dos semanas, en especial a Javier Rodríguez por darnos la oportunidad de colaborar con él. Es un placer encontrar grupos tan agradables como del que vienes. Querría agradecer también toda la ayuda prestada por David Canteli, del Centro Láser de la Universidad Politécnica de Madrid, por todas las pruebas realizadas en sus instalaciones.

Toda esta aventura viene precedida de cinco años de formación a lo largo de los cuales he conocido a gente maravillosa que han estado conmigo desde el primer día hasta hoy. Por eso, muchas gracias a Laura, a Ignacio y a Carmela por haber disfrutado juntos de nuestra etapa de grado y por seguir apoyándome. Gracias a Ana, que empezó siendo mi compañera de máster para pasar a acompañarme en la vida, en general. También a aquellos doctorandos con los que he compartido cafés, comidas y ocio. Y gracias a aquellas personas que estaban desde hace muchos más años y que siempre estarán ahí, contra viento y marea. Gracias a Nour, por sentirse siempre orgullosa de mi y a Marina, por esos veranos que me daban fuerzas para todo el invierno.

Me siento muy afortunada por la familia que tengo. Gracias, de todo corazón, a mis padres. Todo lo que a ellos les debo no se puede resumir en unas frases. Nunca estaré suficientemente agradecida por todo lo que me enseñan día a día, por su apoyo incondicional y por su cariño infinito. Gracias también a Ainé, por su tortilla, sus lentejas y por ser la abuela más moderna del planeta.

A Manuel, por nuestro día a día y nuestras escapadas. Por las visitas a media mañana y las palabras de ánimo. Por aparecer de imprevisto en mi vida y, sobre todo, por decidir quedarse. Gracias.

Este trabajo ha sido financiado parcialmente por diversas fuentes. Se agradece a la Xunta de Galicia, Consellería de Cultura, Educación y Ordenación Universitaria, por la ayuda de apoyo a la etapa predoctoral 2016 en las universidades del Sistema Universitario de Galicia (SUG), cofinanciada parcialmente por el programa operativo Fondo Social Europeo (FSE) Galicia 2014-2020. Se agradece a la Xunta de Galicia y al Fondo Europeo de Desarrollo Regional (FEDER) por el proyecto ED431B 2017/64, AGRUP2015/11 y ED431E 2018/08. Se agradece al Ministerio de Economía y Competitividad (MINECO) del gobierno de España por los proyectos MAT2015-71119-R y FIS2015-71933-REDT.

LIST OF CONTENTS

RESUMEN EXTENSO

A lo largo de los últimos años, la investigación en dispositivos fluídicos ha suscitado gran interés debido a las numerosas aplicaciones que estos poseen en diferentes áreas de conocimiento como química, biología o medicina. El origen de estos dispositivos está directamente ligado al nacimiento de los sistemas microelectromecánicos alrededor de 1960. Cuando las herramientas de fabricación para dispositivos microelectrónicos se aplicaron a problemas en la mecánica, óptica y fluídica, surgió una nueva rama de conocimiento, siendo en 1979 cuando se publicó la primera investigación sobre un dispositivo "lab-on-a-chip" o de laboratorio miniaturizado integrado. A partir de ese momento, se desarrolló un extenso trabajo relacionado con la fabricación y aplicabilidad de estos sistemas, lo cual se tradujo en un gran impulso en investigación y un creciente interés comercial.

La importancia de la fotónica en el desarrollo de este campo de conocimiento es innegable. Ello se evidencia en las técnicas de fabricación de estos dispositivos en las cuales se emplea luz, como la litografía o la ablación láser. También desempeñó un papel clave en la evolución del microscopio, necesario para inspecciones de los chips fabricados, análisis de los resultados finales o monitorización de los experimentos de fluídica.

Las técnicas de fabricación de estos dispositivos son muy diversas. De entre todas ellas destaca la ablación láser debido a las ventajas que posee, como versatilidad, rápida velocidad de procesado, precisión, no necesidad de contacto con la muestra ni de instalaciones especiales como salas limpias. Así mismo, es un proceso autosuficiente que no requiere de tratamientos posteriores para retirar el material. La ablación láser puede realizarse sobre diferentes

materiales. En particular, el vidrio se presenta como un material adecuado para la fabricación de dispositivos con esta técnica gracias a su trasparencia en el espectro visible, su biocompatibilidad, resistencia química y robustez.

Esta tesis se centra en el estructurado láser de materiales, tanto a escala micrométrica como milimétrica, para la fabricación de dispositivos con aplicaciones en biomedicina. Comienza en su Capítulo 1, con un estado del arte general sobre los dispositivos fluídicos y sus aplicaciones, así como las diversas técnicas de fabricación que existen y los materiales más adecuados para las aplicaciones que se presentan. Entre los métodos de fabricación que existen se menciona la litografía, las técnicas de moldeado, la litografía blanda y la ablación láser.

A continuación, en el Capítulo 2, se presenta el equipamiento y materiales que se van a utilizar a lo largo del trabajo. Como materiales principales encontramos el vidrio sodocálcido y el polidimetilsiloxano (PDMS). El vidrio sodocálcico empleado tiene una absorción de entorno al 80% para longitudes de onda del infrarrojo, en las que operan los láseres empleados para trabajar sobre este material. Además, la composición de ambas caras del sustrato es analizada mediante EDX, obteniendo que ésta es similar en ambos casos, donde predomina el dióxido de silicio, el óxido de sodio o el óxido de calcio, salvo por cierta presencia de dopantes de estaño en solo una de las caras. Estas impurezas derivan del proceso de fabricación del vidrio y serán claves para iniciar el proceso de ablación cuando se utilizan láseres de duración de pulsos de nanosegundos, debido a los mecanismos de absorción que ocurren en dicho régimen. El PDMS es un elastómero que se emplea para el replicado de estructuras mediante técnicas de litografía blanda y que destaca por su trasparencia, permeabilidad a gases, capacidad de replicado hasta el nanómetro y coste relativamente bajo, entre otras características. De entre los equipos láser que se van a emplear, cabe destacar los sistemas láser pulsados. En particular, se utilizan cinco equipos diferentes a lo largo de este trabajo con duraciones de pulso que abarcan de los

nanosegundos a los femtosegundos y con longitudes de onda desde 532 nm a 10.6 μm. Otros equipos que se utilizan a lo largo de esta tesis son hornos para aplicación de tratamientos térmicos estáticos o dinámicos, máquinas de activación de superficies con plasma, bombas peristálticas o incubadoras para cultivos celulares que validen la aplicación de los dispositivos previamente fabricados. En lo relativo a microscopía para estudio y caracterización de materiales y células, se emplean microscopios metalúrgicos, confocal, SEM y de fluorescencia.

El Capítulo 3 se centra en la fabricación de canales de diferentes dimensiones, desde micrómetros a milímetros, mediante tecnología láser sobre vidrio sodocálcico. Antes de proceder al estudio de la fabricación se realiza una introducción a los mecanismos de ablación láser de materiales según sean opacos o trasparentes a la longitud de onda y la duración de pulso que se emplee. En el caso de mecanizado láser de superficies con pulsos de nanosegundos, donde la duración de pulso es mayor que el tiempo de trasferencia de energía por parte del electrón a la red, la absorción ocurre por efecto Joule para materiales opacos mientras que se debe a procesos no lineales para materiales trasparentes. En este caso, el principal proceso de absorción se conoce como ionización en avalancha y depende en gran medida de la densidad de electrones libres presentes previamente en el material. Para duraciones de pulso mucho menores al tiempo de relajación de la red, la absorción de energía para la ablación de la superficie se debe principalmente al efecto de absorción multifotón y al efecto túnel, entre otros mecanismos. Todos estos procesos dan lugar a una ablación directa del material en la superficie sobre la que se focaliza el haz. Sin embargo, existen también técnicas de retirada de material de forma indirecta utilizando irradiación láser, como es el caso de la ablación inducida por láser y asistida por plasma, LIPAA de sus siglas en inglés. En este proceso, la ablación ocurre en la cara trasera del material, que se encuentra en contacto con una lámina de metal encargada de iniciar la ablación. El uso de técnicas directas o indirectas de mecanizado determinan las características finales de la estructura, así como sus dimensiones, obteniéndose profundidades del

orden de decenas de micras al trabajar directamente un material trasparente a la longitud de onda y generando estructuras de centenas de micras al milímetro al trabajar con métodos de ablación indirecta. Tras la introducción sobre los diferentes métodos de ablación, se fabrican microcanales sobre vidrio sodocácico con diferentes sistemas láser mediante ablación directa de la superficie. Los tres equipos empleados tienen longitudes de onda en el rango del infrarrojo pero con duraciones de pulso que varían, siendo de nanosegundo, picosegundo y femtosegundo, respectivamente. El objetivo de esta sección es hallar los parámetros de fabricación óptimos para obtener un canal semicircular en cada caso, con dimensiones similares entre ellos, así como comparar los resultados entre los diferentes equipos. En particular, con el equipo que opera con pulsos de nanosegundos, los parámetros láser de fabricación son 700 μJ de energía por pulso, 10 kHz tasa de repetición y 50 mm/s de velocidad de barrido, obteniendo tras 6 pasadas un canal de 8.7±0.1 μm de profundidad y 23.9±0.6 μm de ancho, con una rugosidad aritmética media de superficie de 178.7±15.6 nm. Para el caso de picosegundos, el valor de energía por pulso corresponde con 80 μJ, la tasa de repetición es de 10 kHz y la velocidad de barrido es de 20 mm/s. Las dimensiones con una pasada en este caso son similares al caso anterior, de 8.4±0.2 μm de ancho por 17.8±0.2 μm de profundidad, mientras que la rugosidad toma un valor de 1028.3±198.4 nm. Por último, con el equipo de femtosegundos, los parámetros láser corresponden a una energía por pulso de 40 μJ, 1 kHz de tasa de repetición y 0.6 mm/s de velocidad de barrido, obteniendo un canal semicircular de 20.7±1.4 μm diámetro y 10.1±0.6 μm de profundidad, con una rugosidad media de superficie de 1016.3±123.8 nm. Se observan importantes diferencias en la ablación al estructurar las dos caras del material. Mientras que en una de las caras se obtiene un microcanal de calidad, en la otra se generan grietas en la estructura o incluso, en el caso de duración de pulsos de nanosegundos, no se lleva a cabo la ablación. Esto se debe a la presencia de impurezas de estaño en solo una de las caras del material, derivadas del proceso de fabricación del vidrio. En el caso de ablación en el régimen de nanosegundos, estos dopantes son claves para iniciar el proceso de ionización en avalancha que dará lugar a la ablación del

material, por ello, en ausencia de estaño, no se genera ningún microcanal. Los microcanales obtenidos se someten a diferentes tratamientos térmicos con un horno estático. Se funden a temperaturas desde los 590 ºC a los 630 ºC de manera controlada, de modo que se modifique la rugosidad de la estructura, así como su perfil. En concreto, se consigue reducir la rugosidad a un rango entre los 43 y 12 nm. Teniendo en cuenta que diversas aplicaciones de estos microcanales requieren de valores diferentes de rugosidades para su correcto desarrollo, resulta interesante poder conseguir la rugosidad superficial necesaria en cada caso. En la siguiente sección del Capítulo 3, la técnica de fabricación láser de canales pasa a ser indirecta. En concreto, se empleará ablación inducida por láser y asistida por plasma para obtener canales en vidrio de mayores dimensiones que los anteriores. Los parámetros láser para la fabricación de dispositivos en este caso corresponden a una potencia media de 8 W, tasa de repetición de 12 kHz y velocidad de barrido de 1000 mm/s. La separación óptima entre pasadas láser consecutivas es 25 µm. Mediante este proceso se alcanzan canales de alrededor de 1 mm de profundidad y 2 mm de diámetro. La rugosidad media aritmética de línea en este caso toma un valor bastante elevado, de 5285.01±304.56 nm, debido a la naturaleza explosiva de la ablación. Con el objetivo de reducir este valor de rugosidad y modificar ligeramente el perfil del canal para obtener un perfil más parecido a un semicírculo, las estructuras se someten a diferentes tratamientos térmicos. Primero se somete la pieza aun tratamiento térmico con láser de CO_2 combinado con un horno de rodillos. La muestra se va calentando gradualmente a lo largo del horno para evitar choque térmico cuando el láser irradia la superficie y la funde. A pesar de ser una técnica interesante que sólo interactúa con la superficie del material y no funde toda la pieza, en este caso debido a las dimensiones del canal, no resulta el tratamiento más adecuado ya que se necesitan muchas pasadas para observar un cambio apreciable en la morfología. Por ello, se procede a aplicar un tratamiento térmico por encima de la temperatura de transición de vidrio (570 ºC) en un horno estático, resultando este proceso más eficiente que el anterior. Los canales se introducen en el horno durante dos horas para modificar su

topografía. Se aplican tratamientos a 590 ºC, 630 ºC y 670 ºC. De este modo la rugosidad se reduce hasta 27.18±4.52 nm en el caso de 670 ºC y en todos ellos el perfil se modifica hacia una forma más redondeada al redistribuirse el material fundido. El objetivo final de estas estructuras es imitar una bifurcación coronaria, de tal modo que se puedan utilizar como dispositivos preclínicos para estudios in vitro de patologías. Dado que se busca un modelo de vaso sanguíneo sobre el cual se puedan cultivar células en sus paredes, se elige otro material final diferente al vidrio que permita el intercambio de gases que las células necesitan para sobrevivir. Ese material es el PDMS, que destaca por propiedades como su biocompatibilidad, flexibilidad o permeabilidad a gases. La estructura realizada en vidrio con tecnologías láser se emplea como molde a replicar en este material final. La técnica de copiado se conoce como litografía blanda y, en nuestro caso, se requiere de un molde intermedio para recuperar totalmente la estructura realizada sobre vidrio. A lo largo del trabajo se describen dos técnicas para el replicado y sellado del dispositivo. La primera se basa en la mezcla de PDMS con diferentes proporciones de base y endurecedor para fabricar las diferentes partes. Antes de que los componentes se curen por completo, se unen y realizan las conexiones, obteniendo un dispositivo irreversiblemente sellado tras la total curación de la estructura. La segunda técnica consiste en la fabricación de ambas partes con la misma proporción y su curación por separado, siendo selladas posteriormente mediante la activación de la superficie por plasma en una atmósfera de oxígeno. Este último procedimiento resulta más adecuado al tener una tasa de error menor por manipulación de los elementos. En ambos casos, se puede obtener tanto una estructura de medio canal como una de canal completo. En el primer caso, basta con tapar el dispositivo con una superficie plana y en el segundo, con una estructura simétrica a la inicial.

En el Capítulo 4 se presentan algunas aplicaciones del dispositivo fabricado en PDMS en el capítulo anterior. Como ya hemos mencionado, el fin último de dicho dispositivo consiste en imitar un vaso sanguíneo funcional, por lo que células endoteliales se cultivan en sus paredes interiores para validarlo biológicamente. Para asegurar

la presencia de células en la totalidad del canal el cultivo se realiza en dos etapas, cultivando las células primero en una de las caras para después girarlo y cultivarlas en la otra. De este modo, no solo se consigue que las células crezcan en la parte superior e inferior del canal, sino que también en los laterales. Una vez que el dispositivo es validado biológicamente, se estudia la adherencia celular a las paredes en condiciones de flujo según la rugosidad del molde de vidrio a partir del cual se fabrican. Se observa que cuando los dispositivos se fabrican con rugosidades medias entre 400.84±20.31 nm y 27.18±4.52 nm, obtenidas mediante tratamientos de 630 ºC y 670 ºC respectivamente, la monocapa de células endoteliales cultivada se desprende al aplicar flujos a velocidades de 1 ml/min. En el caso de rugosidades entre 5285.01±304.56 nm y 1528.01±100.01 nm, correspondientes a moldes sin tratamiento térmico y con tratamiento a 590 ºC, las células resisten en las pareces sin desprenderse al pasar flujo a través del canal. En particular, la última configuración se ha determinado como óptima al tener un valor de rugosidad tal que las células se mantienen adheridas a la pared, pero también se modifica ligeramente el perfil de la estructura hacia una forma más semicircular en vez de rectangular. Con ello se mimetiza mejor la estructura de un vaso sanguíneo y se facilitan las inspecciones microscópicas en el dispositivo al ser menos rugoso que en el caso de no haberse sometido a ningún tratamiento. En la siguiente sección de este capítulo se presenta un problema común cuando el PDMS entra en contacto con algunos solventes orgánicos comúnmente empleados en laboratorios biomédicos, como puede ser el etanol. Cuando esto ocurre el material se degrada y, como consecuencia, el posterior crecimiento celular sobre las paredes del canal será totalmente anormal. Para solucionar este problema se propone recubrir la superficie con capas finas de diferentes composiciones de sol-gel. En este trabajo se realizan recubrimientos mediante la técnica de “dip coating” o recubrimiento por inmersión con tres composiciones: 60MTES/40TEOS, 70MTES/30TISP y 80MTES/20TISP. Tras cultivar células endoteliales sobre ellas, se determina que las tres son biocompatibles, pero que la composición 80MTES/20TISP es la que presenta mejores resultados en cuanto a crecimiento celular, observando en este caso

que las células crecen de forma normal llegando a formar una monocapa. Por último, en este capítulo, se utilizan los dispositivos fabricados para determinar zonas de baja velocidad en las bifurcaciones coronarias según el ángulo de la misma. En estas zonas la velocidad del flujo es menor de lo normal, pudiendo dar lugar a diferentes patologías como alteraciones del endotelio, enfermedades cardiacas o acumulación de células tumorales circulantes del torrente sanguíneo que puedan depositarse en esas zonas, anidar y llegar a causar metástasis. Para la determinación de estas áreas, se fabrican varios dispositivos preclínicos como los descritos en el capítulo anterior con diferentes geometrías. A través de ellos se hace pasar una solución de sucrosa y ferroína en modo pulsado. Mediante técnicas de imagen, se establece la zona en la que la ferroína pasa más tiempo al encontrarse en un área donde la velocidad del flujo es menor. Estos resultados se comparan con simulaciones numéricas, que no son objeto central de esta tesis, obteniendo concordancia entre ambos. Se determinan las zonas de baja velocidad para seis ángulos de bifurcación diferentes y se determina que el correspondiente a 90º es el que presenta un área de baja velocidad mayor frente al resto y, por tanto, podría dar lugar a ciertos problemas derivados de la alteración de la dinámica del flujo.

En el Capítulo 5 se presentan otras aplicaciones del estructurado láser de superficies en el área de la biomedicina. La primera de ellas es el microestructurado láser de superficies de titanio y tántalo (materiales biocompatibles) utilizando los focos de una matriz de microlentes en combinación con el efecto Talbot. Gracias a este fenómeno la imagen de los focos se forma a determinadas distancias de los mismos, evitando el deterioro de las microlentes debido al material expelido durante la ablación, dado que se aumenta en este proceso la distancia entre el sustrato a ablacionar y la matriz de microlentes. Además, gracias al efecto Talbot fraccionario, se consiguen patrones de menor período que el original. Con este método se modifica de forma controlada superficies de titanio y tántalo, materiales comúnmente empleados en biomedicina. Se evalúa la adhesión de células endoteliales a estos sustratos según el patrón de la

superficie, encontrando que en todos los casos la adhesión celular es mayor sobre una superficie microestructurada que sobre una lisa. En particular, los patrones obtenidos a partir de imágenes Talbot de los focos de las microlentes con período 45 μm promueven el crecimiento y adhesión celular en titanio, mientras que el de período 90 μm lo hace en tántalo. Otra aplicación del estructurado de superficies con tecnologías láser consiste en la fabricación de dispositivos sobre vidrio para capturar células tumorales circulantes en el torrente sanguíneo. El chip se fabrica por ablación inducida por láser y asistida por plasma con parámetros láser: 8 W potencia media, 10 kHz tasa de repetición y 500 mm/s de velocidad de barrido. Está compuesto por una matriz hexagonal de micropilares de 420 μm de diámetro, 250 μm de profundidad y 245 μm de separación entre ellos. Las estructuras se funcionalizan con anticuerpos EpCAM (molécula de adhesión de célula epitelial) de tal modo que las células tumorales que entren en contacto con los micropilares se queden adheridas a estos. El dispositivo se validada haciendo pasar a través de él células tumorales de la línea HEC-1A, correspondientes a cáncer de endometrio. El dispositivo muestra una eficacia superior al 75 %.

Por último, la tesis presenta las conclusiones principales obtenidas a lo largo del trabajo.

SHORT SUMMARY

This thesis presents the use of laser technologies for structuring different materials for applications in biomedicine. One of the aims of this work is the fabrication of fluidic chips for their employment as preclinical devices. During the past decades there has been a growing interest in the study and development of analysis devices due to the important applications they present in different scientific fields, such as Chemistry, Biology or Medicine. Different fabrication techniques have been described for this purpose but among them, laser outstands thanks to its accuracy, versatility or speed. By direct or indirect laser techniques, materials like soda-lime glass, titanium or tantalum are structured. In this work, main ablation mechanisms are reviewed regarding the temporal duration of the laser pulse as well as the response of the material to the laser wavelength. Microchannels with similar dimensions are fabricated over soda-lime glass by laser direct ablation using three different laser systems with same wavelength, in the infrared spectral range, but pulse durations of nano, pico and femtoseconds. Results are analysed and evaluated, finding significant differences depending on the side of the glass. Thermal treatments are applied to the microchannels to modify their initial roughness. Millimetre dimension channels are obtained in soda-lime glass by indirect laser ablation with a nanosecond laser system. These structures are employed as master that replicates its structure for creating a preclinical device that imitates a coronary bifurcation. The replica procedure is known as soft-lithography and is performed in polydimethylsiloxane (PDMS), biocompatible material suitable for long term cell cultures. The device is validated with human umbilical vein endothelial cells that adhere and attach to the totality of the inner surface of the channel. Optimal roughness value of the device is determined for cells to withstand flux conditions. Degradation of PDMS to some organic solvents commonly employed in biomedicine

is solved by coating the channels with sol-gel chemistry. Different compositions are employed: 60MTES/40TEOS, 70MTES/30TISP and 80MTES/20TISP. Cell behaviour is studied over the different coatings. These devices that imitate coronary bifurcations are employed to determinate low velocity areas in these blood vessels. In these zones, fluid dynamics is altered and can lead to the development of vascular pathologies. The experimental results are compared to numerical ones. Finally, other applications of laser structuring for biomedical applications are presented. Using a microlens array and the Talbot effect, biocompatible material titanium and tantalum are ablated with a pulsed laser. Thanks to the Talbot phenomenon, different patterns from the original can be achieved and damage of the microlens array during the ablation is avoided. The impact of the patterns in cellular growth is studied by culturing endothelial cells over the structured substrates. By laser indirect ablation, a microfluidic device for capturing circulating tumour cells is fabricated over soda-lime glass. The device if functionalized and validated, showing a trapping efficiency above the 75%.

Key words: laser ablation, laser-matter interaction, microfluidic devices, preclinical devices, coronary bifurcation, soft-lithography, glass, Talbot effect.

1. INTRODUCTION

During the past decades there has been a growing interest in the study and development of analysis devices due to the important applications they present in different scientific fields, such as Chemistry, Biology or Medicine. This concept involves, among other devices: lab-on-a-chip; organ-on-a-chip; total analysis systems and preclinical devices.

Lab-on-a-chip (LOC) consists in miniaturised integrated devices that allow performing same tests or experiments as in conventional laboratories but with fewer amounts of reagents, less process time and simplified procedures. On the other hand, organ-on-a-chip devices emulate the functioning and environment of certain body organs with the purpose of studying and understanding different pathologies and cellular behaviours. Total analysis systems (TAS) and miniaturised total analysis systems (μ-TAS) are more focused into chemistry assays whilst preclinical devices play an important role in biomedical investigation. Despite the specific particularities of the above-mentioned chips, they are englobed into the same idea and they share basic elements like fabrication techniques, materials and fluid or micro fluid handling.

The origin of these devices is directly linked with the advances in integrated circuits and the development of microelectronics. With the progresses in processing technologies and the employment of other materials than silicon, in the 1960s microelectromechanical systems (MEMS) born as a new field [1, 2]. This was boosted by Richard Feynman's talk "There's plenty of room at the bottom" in 1959, where he offered one thousand dollars for fabricating an electrical motor smaller than 400 μm [3], challenge not achieved until then. When fabrication tools for microelectronic devices were applied in

mechanics, optics and fluidic problems, a new branch of research emerged. Around the 1970s, interest in the fabrication of miniaturised devices aroused and it was in 1979 when the first paper of a lab-on-a-chip device was published. It was developed in Stanford University by S.C. Terry et al. and presented a miniature gas analysis system based on the principles of gas chromatography [4]. Between 1980 and 1990 there was a rapid development of these devices, as several research groups created micropumps [5, 6], microvalves [7] and flow sensors [8-10], needed for flux control in the chips. The term of total analysis system was first introduced in 1990 by Manz et al. when they proposed a general concept of miniaturised systems for analysis as well as their theoretical functions [11]. Since this date, there was an intense work about fabrication and applicability of these devices, which was translated into a big boost in research and into a growing commercial interest. This fact can be clearly noted by viewing the increasing number of publications about these topics during the past ten years. Figure 1.1 shows a histogram of the evolution of the number of papers related with the mentioned subjects (organ-on-a-chip, preclinical device, μ-TAS, lab-on-a-chip and microfluidic devices) in the past decade [12].

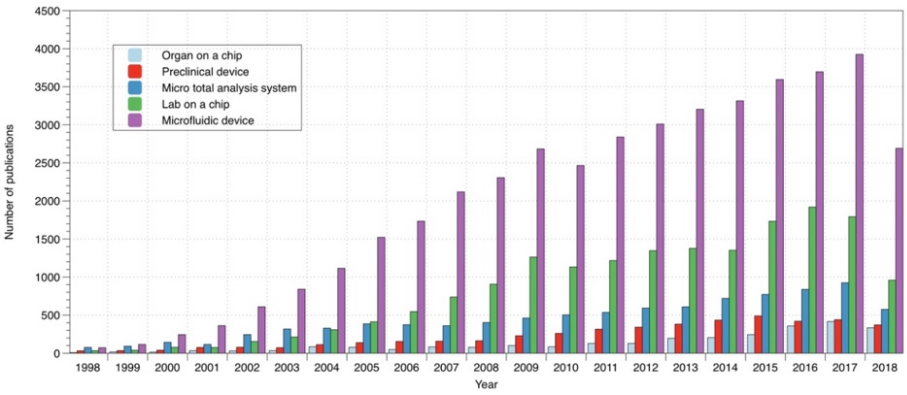

Figure 1.1: Histogram of the evolution of the number of publications in organ-on-a-chip, preclinical device, μ-TAS, lab-on-a-chip and microfluidic device topics from 1998 to 2018. Source: Web of Science.

In this graph, a significant growing tendency during the last ten years can be appreciated regarding the number of research work in the area of analysis devices, in their fabrication and applications in different fields. The "microfluidic device" topic collects the largest number of publications with a total amount of 42535 during the past decade. It should be noted that this theme may also include the subsequent searched topics since it is a more general concept that encompass the others and, therefore, gathers the largest amount of original research work. "Lab-on-a-chip" related papers are located in a second place with a total number of 17631. They are followed by "micro total analysis system" category, with 10568 publications in the last decade, reminding that this term is mostly used to refer to devices for chemical applications. Fourthly, there are 5003 "preclinical device" papers during these years and finally, 2833 publications about "organ-on-a-chip". Logically, this last topic reunites the smaller number of papers since it derives from all the microfluidic generated knowledge and from the development of fabrication techniques and flux control in the previous years. This know-how demonstrated the ability to control cellular environments and it made possible the creation of these mimetic systems, so it was in the late 2000s when the field started to become significant [13].

The increasing number of publications in these topics is mainly due to the significance and social impact of the applications they present. Some examples are in the field of cell biology, where these devices can be employed to chemically analyse the composition of a single cell [14], to understand the forces and mechanisms that cells exert over the substrates they grow and attach [15] or even to study the content of cells with subcellular selectivity [16]. In chemical synthesis, they have a huge importance in drug discovery since they reduce the time, reagents and resources needed for this laborious task and also, automatizes the process [17]. Another application is the fabrication of human organs models in laboratory conditions for pathology study or drug delivery research. It can be found models of kidney [18], liver [19], blood vessels [20] or gut [21], among others. Numerous reviews about the evolution, current situation and future of

these chips, as well as about their applications, can be found in the literature [22-24].

The importance of photonics in the development of these fields is undeniable. This role is evidenced in the fabrication techniques of microfluidic devices that employ light, such as lithography or laser ablation. It has also played a determinant function in the evolution of microscopy, which was necessary for inspections of the fabricated devices, analysis and evaluation of the final results or even monitoring of the experiment while it is carried out. Sensing inside the devices has always been linked with optics advances and during the past years a new field called optofluidics has became relevant. It combines microfluidic technology with optics, exploiting microfluidics flow control and optics capability of sensing [25].

1.1. FABRICATION TECHNIQUES IN LAB-ON-A-CHIP DEVICES

This subsection presents an overview of most employed manufacturing procedures in analysis devices. It is undeniable that the development of these chips is directly linked with the rapid advances of fabrication techniques. First devices were manufactured following the same procedures and materials as the ones used in microelectromechanical systems, mainly lithography methods to microstructure silicon [26], but soon diverged from this method and material. Several new fabrication techniques for these kinds of devices appeared [1]. The choice of one or another depends on the chosen material to structure as well as on the available laboratory facilities. Some of the main manufacturing techniques of analysis devices are described in the following subsections.

1.1.1. Lithography

Lithography is one of the first techniques employed for the fabrication of fluidic chips since it derives from the MEMS field. Basically, it consists in the exposure of a sensitive resist to electromagnetic or particle radiation in order to transfer a pattern to a

substrate (glass, silicon or polymer). The resist is a polymer that chemically reacts when it is exposed to radiation [27]. Electromagnetic exposure (photolithography) can be in the ultraviolet spectral range or even in the X-ray and usually needs a mask that transfers the pattern to the surface. Particle beam lithography involves exposure of the resist to electron beam or ion beam and does not need a mask. General steps of lithography are explained below and depicted in Figure 1.2 [28].

First, the substrate is prepared in order to ensure a proper adhesion of the resist to its surface. Usually it is baked in vacuum or in dry nitrogen. Then the resist is deposited over the substrate by spin coating, forming a uniform film. Once the materials are prepared, a mask, if needed, is properly aligned over the substrate and the resist is exposed to radiation. The mask is resistant to the radiation and selectively lay bare some areas of the polymer and not others in order to transfer the pattern to the resist. As it was mentioned, the resist changes its chemistry when exposed. If the polymer degrades and becomes more soluble, it is called positive lithography. On the other hand, if it crosslinks we call it negative lithography. When using a mask for transferring the pattern, it can be placed in contact with the resist or not. If it is in contact, diffraction effects are minimised but the mask is damaged in a few cycles. By separating them, the useful life of the mask increases. Failures in the structure should increase due to diffraction effects, but since working in the UV or X-ray regime they are considerably less than in other wavelengths. In the development step, the irradiated region (positive lithography) or the non-irradiated one (negative lithography) of the polymer is removed.

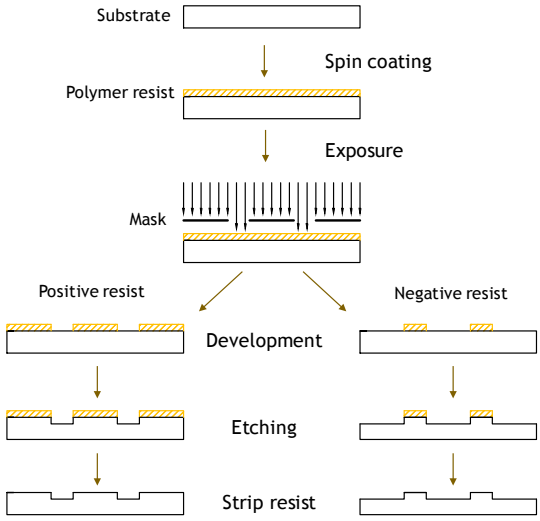

Figure 1.2: Schematic representation of the lithography process and their steps [29].

Next, the substrate is etched in order to transfer the structure from the resist to the final material. The resist owes its name to its resistance to the etching process, which only attacks the substrate that is not protected by the polymer. There are two different kinds of etching: wet and dry [30]. Wet etching is a cheap and easily handling technique that consists in using an etchant solution, such as acid, that chemically attacks the substrate isotropically. One drawback of this technique is that this isotropic etching can lead to substrate undercutting as it can be etched beneath the resist. On the contrary, dry etching is an anisotropic process. The problems of wet process are solved by replacing the etchant for a chemically reactive plasma. In this process, also called reactive ion etching (RIE), an electric field is applied forming a reactive gas plasma, ions are accelerated toward the sample, reacts with the surface and a directional etching is obtained. Finally, once the pattern is transferred to the substrate, the resist is stripped from the chip.

It has been previously mentioned that there is not always need of mask. Particle beam lithography with ions and electrons, and also

photolithography with laser beam, directly writes the pattern over the polymer resist. This kind of techniques are englobed under the name of scanning beam lithography [31]. They are slow processes in comparison with conventional photolithography methods but they obtain more resolution and precision. Indeed, scanning beam lithography is commonly employed for the fabrication of photomasks for further lithographic processes than for making final devices.

Lithography is a well-know and established technique but it presents some drawbacks as the requirement of cleanroom facilities, the high cost of the procedure and the toxic products involved in the process.

1.1.2. Moulding techniques

Other common procedures for the fabrication of fluidic devices are moulding techniques. Basically, moulding consists in the transference of a pattern from a structured mould to a polymer, reaching micron or even submicron precision. It employs polymers as final materials, which are inexpensive compared to glass or silicon [32]. These methods allow mass production of devices with relatively low costs, factors that are important in applications where the chips should de disposable for safety reasons, such as medicine ones, or when they cannot be recalibrated between usages. Some moulding techniques are injection moulding, hot embossing or thermofusing. A diagram of each of them is shown in Figure 1.3 and they are explained below.

In injection moulding (Figure 1.3.a) the structure is transferred to a polymer by injecting molten material into a closed mould. First, the plastic is introduced in form of granules into a barrel and is heated until the polymer becomes molten. Then, the soften material is introduced inside an already hot mould cavity by pressure. Material cools down and acquires the shape of the cavity. Finally, it is unmoulded. The total process lasts from a few seconds to a few minutes [33].

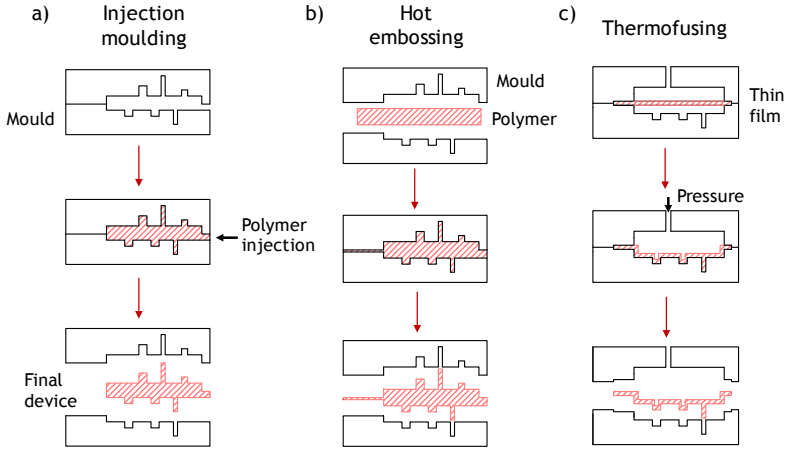

Figure 1.3: Representations of the a) moulding injection, b) hot embossing and c) thermofusing processes [34].

In hot embossing (Figure 1.3.b), an embossing master is mounted inside an embossing machine, which consists of a force frame that delivers pressure over the structured master. Master and polymer are mounted over heating plates that have also the capability to cool down. At the beginning of the cycle both are heated separately in a vacuum chamber. Then, the master is put in contact with the substrate and a controlled force is applied to them. Still with the pressure, the system is cooled down. The embossing mould is never fully closed, producing a residual layer characteristic of the process. Hot embossing cycles are little longer than injection moulding ones since melted polymer is not continuously being introduced into the mould and the master has to be heated over the transition temperature of the polymer to start the casting [35].

There are some variations of the mentioned techniques. Reaction injection moulding is similar to injection moulding but two components are introduced into the closed mould instead of one polymer. By this method, non-thermoplastic plastics can be structured. Injection compression moulding is a combination of hot embossing and injection moulding. In this technique, molten polymer is injected

into a semi-closed moulding tool and pressed with the master by closing the mould. In this way, the problem of heating the polymer in the hot embossing technique is overcome.

Finally, thermofusing methods (Figure 1.3.c) are employed for structuring thin polymer films. The film is introduced into a moulding tool, which is structured in one side, heated up and pressed against de mould with the help of a pressurised gas. Then, the film is cooled down and unmoulded. In contrast with the other techniques, the structures of the mould are not completely filled [36].

1.1.3. Soft-lithography

Among all techniques presented, soft lithography is the one that revolutionized the microfluidics field. It is based in the principle of replication and the material employed for this purpose is polydimethylsiloxane (PDMS), capable to accurately reproduce until the nanometre scale [37]. Advantages and drawbacks of this material will be mentioned in further sections in this chapter.

Soft lithography process can be separated in two steps. First, the elastomer is prepared. Usually, PDMS is presented in two parts, cure agent and base, that have to be mixed in proper proportions for further crosslinking of the material. Secondly, the elastomer is poured over the master substrate that transfer the pattern and it is cured by heating up. Then the PDMS is peeled off from the master and a replica of it is obtained. The process is schematically depicted in Figure 1.4.

Soft lithography was born as investigation work of a single research group in Harvard in the 1990s, led by G. M. Whitesides, and became one of the most employed techniques worldwide in device fabrication, both in academia and industry [23, 38, 39]. Nowadays, plenty of lab-on-a-chip devices, organ-on-a-chip and microfluidic devices are manufactured this way [40-44].

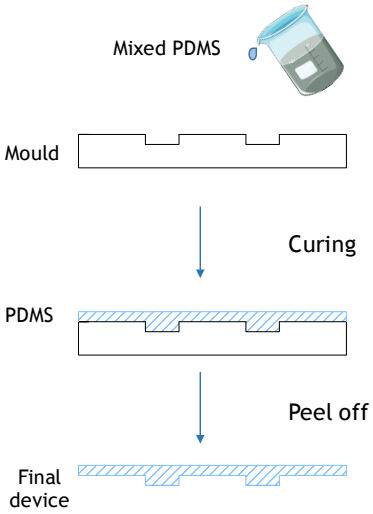

Figure 1.4: Scheme of soft lithography process [45].

1.1.4. Laser ablation

Laser ablation consists in the removal of material when high energy laser pulses are focused over it. Since the discovery of laser light, research in laser science and its application have never stopped. One of the first experiments carried out with focused laser beams were those who involved laser-matter interactions leading to the ejection of particles [46]. Nowadays, laser ablation and its applications play a key role in many areas of scientific research, as well as in industry, where lasers are completely implemented [47, 48]. Laser structuring was first employed for fabricating a microfluidic device in 1997, when the manufacturing of a polymer device and the characterization of the flow through it was reported [49]. Currently, numerous fluidic chips are fabricated by this technology [50-52] due to the advantages that laser ablation presents. It is a non-contact method that implies no thermal or mechanical deformation of the sample if properly used. It is very suitable for serial applications because of the speed of the ablation process and the low cost of it once the equipment is installed. It is a non-toxic process and does not require of special environments or clean rooms. It is an accurate and versatile manufacturing technique that allows fabricating very complex geometries reaching micrometric

precision. Also, it is a self-sufficient process since there is no need of posterior chemical treatments to obtain the pattern neither mask to write the structure on the surface [53, 54]. Figure 1.5 shows some examples of microfluidic devices manufactured by laser ablation.

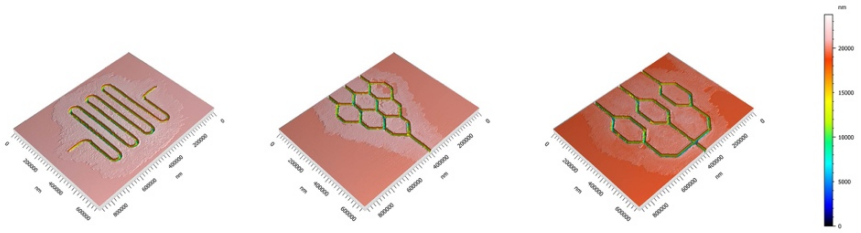

Figure 1.5: Confocal images of fluidic devices fabricated by laser ablation of a soda-lime substrate.

Laser ablation can be performed in plenty of materials, like polymers or glass, if working with the proper laser wavelength and pulse duration. Physical processes involved in ablation directly depend on the material due to the different interactions that occur with light. Most of the materials employed in fluidic assays are transparent for performing optical inspections. Since most of them are linearly absorbent in the UV, lasers with this wavelength were intuitively employed for this purpose [55]. Nevertheless, laser fabrication with infrared (IR) lasers, where transparent materials are quite non-absorbent, has also been performed [56] with the advantage that systems operating in the IR are more established in industry than the UV ones. Pulse duration is also a key factor in the physics of the process and in the aspect of the final structure. With the discovery femtosecond pulses, more accurate geometries are obtained and less thermal damage ablation can be performed. The physical aspects of laser ablation will be explained in Chapter 3.

1.2. MATERIALS IN LAB-ON-A-CHIP DEVICES

Lab-on-a-chip devices can be manufactured in many different materials. In this subsection, a general overview of some of the most employed ones is presented. Silicon devices mainly use techniques

derived from the field of integrated circuits and MEMS. In fact, one of the advantages of this material is the know-how generated from the years of research in this topic. Electrical conductivity can be a positive or negative aspect of silicon depending on the final application, as well as its rigidity and robustness [57]. What is clearly a disadvantage of the material in this field is its opacity in the ultraviolet (UV) and visible light spectral range, which avoids the possibility of optical inspections while performing experiments [24]. Moreover, it is not permeable to gases, which is problematic when working with long term cell culture, and usually silicon techniques require of cleanroom facilities, issue that increases the cost of production. Glass substrate shares a lot of properties with silicon: mechanical rigidity, chemical resistance, impermeability to gases or low permeability. On the contrary, glass does permit optical inspections since it is transparent in the wavelength range microscopes operate. Due to its properties, in this work glass will be chosen as suitable material for laser structuring for fluidic devices.

Polymeric materials are getting more attention nowadays since they overcome the problem of the high costs of chip fabrication in cleanroom facilities and allow a mass production by using moulding techniques. Polymers, in general, are long chains obtained during polymerisation processes. There is a wide variety of polymers with different optical properties, chemical resistance and permeability to gases. Thermoplastic polymers, such as polymethylmethacrylate (PMMA) or polycarbonate (PC), have emerged as the most employed polymers in the field. They are composed by chains weakly bonded together so they soften when heated and get hard when they cool down [58]. Thermoplastics can be optically transparent and their properties can significantly vary depending on the plastic. Therefore, they should be carefully chosen regarding the final application, fabrication technique and sealing process [27].

One polymer that stands out among the others is polydimethylsiloxane, commonly known by its acronym PDMS. This elastomer was first employed in 1998 by G. M. Whitesides research

group in Harvard for the fabrication of a microfluidic system by replication procedures, after several years investigating with PDMS material [59, 60]. The employed technique for fabricating microfluidic devices with this material is soft-lithography and was previously explained in this chapter. Nowadays, this method and material are the most widely employed for manufacturing these kinds of devices. The success of PDMS can be attributed to key factors such as relative cheap cost compared with other materials or easy mode of use, as well as characteristics like being permeable to gases, transparent in the UV and visible regimes and low autofluorescent. Moreover, it can be easily turned from hydrophobic to hydrophilic by oxygen plasma exposure, very attractive quality in flux experiments [61]. PDMS can be bonded reversibly or irreversibly to other materials like glass, polymers or even to itself and also has the capability to replicate structures until the nanometre. It is elastic, property that allow researchers to develop valves and pumps in PDMS, needed in some devices for flow control [62, 63]. All of these aspects, make this material very suitable for performing assays with cells and long-term cultures. This fact has led to numerous device designs and boosted the usage of PDMS. Nevertheless, this material has some disadvantages. PDMS degrades and dissolves in many organic components, very common in biological or chemical experiments [64]. To overcome this problem, solutions like glass like coatings of PDMS have been proposed [65]. Also, due to its permeability, evaporation can occur in long term experiments and it was shown that PDMS can absorb small molecules because of its porous nature, which could be problematic in cellular or drug experiments [66].

Other materials have recently been considered for the fabrication of diagnosis devices [67]. Hydrogels outstands in biological applications since they are excellent in 3D biocultures. They are biocompatible 3D networks of hydrophilic polymer into an aqueous medium. They present a high porosity with controllable porous size and allow the diffusion of small molecules or biological particles through them. The combination of aqueous medium and permeability make hydrogels similar to extracellular matrix and therefore, very

suitable for embedded cells in three-dimension cultures. Some drawbacks of these materials are the high cost they present or the non-reusability [68].

Other examples are paper-based microfluidic devices [69]. Paper is a porous matrix of cellulose and when specific zones of the device are hydrophobically modified, liquid is guided through the hydrophilic areas by capillary effect. Unlike the majority of devices, paper chips are not sealed and are an alternative to conventional materials when there is no need of closed devices. Other promising material is cloth, where the interstitial porosity of the material is exploited for liquid flow [70]. These two materials, paper and cloth, outstand due to their affordable cost, simplicity and easy way to incinerate if biological samples need to be destroy after their use. Because of all of these features, they are an attractive solution for developing economies or low resources situations, as well as in personalized medical care.

1.3. THESIS OUTLINE

The work presented in this thesis is devoted to the fabrication and characterization of preclinical devices with laser technologies for performing in vitro experiments under controlled laboratory conditions. The fabrication technology is mainly based on the use of pulsed lasers for structuring surfaces, in particular soda-lime glass. Different laser ablation techniques are employed to obtain channels with different dimensions. Direct laser ablation of glass is performed with several pulse durations in order to fabricate micrometric structures. For fabricating channels with millimetre dimensions that imitates blood vessels, for example coronaries bifurcations, laser-induced plasma-assisted ablation is carried out. Accuracy and versatility, derived from laser process, allow the fabrication of different channel geometries. In order to carry out bioassays, where the fabricated chips imitate a blood vessel and allow cell culture in their walls, channels are replicated in a more suitable biocompatible material: polydimethylsiloxane (PDMS). Final devices are sealed and closed, and proper connections are made in the chip. Finally, they are

biologically validated by culturing human endothelial cells that resist flux conditions over the channel walls.

Moreover, problems associated with the degradation of PDMS when in contact with some organic solvents are studied and solved by means of sol-gel technique. By coating the surface of the PDMS with certain sol-gel compositions, chemical robustness of the glass is obtained while biocompatibility properties of PDMS are maintained.

The results derived from flux assays performed in these devices with several bifurcation angles allow us to determine the low velocity zones in different vessel geometries. In these areas the velocity value of the flux and shear stress are smaller than in others areas and as a result, vascular disease risk is higher there than in other zones since endothelial cells are not exposed to the proper flux conditions of blood stream. Also in these zones, it is more probable for cells, such as circulating tumour cells (CTCs), to stop its trajectory and attach to the endothelium, increasing metastasis probability. By performing flux experiments with these devices, most hazardous geometries can be identified. This is directly linked with a better understanding of certain pathologies, early diagnosis and their treatment.

Finally, other applications of laser microstructuring in the biological field are presented. In particular, the surface modification of biocompatible metals like titanium or tantalum, elements present in materials that conform most of implantable prosthesis, is carried out with the aim of enhancing cellular attachment and growth on these surfaces. This microstructuring is performed in combination with a well-known optical phenomenon, the Talbot effect, which allows us to obtain by ablation, in an easy and fast way, surfaces with different morphological properties. Apart from this, but based in the same manufacturing principle of pulsed laser ablation, a glass device able to capture circulating tumour cells is manufactured and validated.

This thesis is organised as follows. Chapter 1 is devoted to the state of the art of preclinical devices, introducing their actual situation

as well as the most common materials and technologies employed for their fabrication. In Chapter 2, material and methods used for the development of this thesis are presented. Chapter 3 shows the manufacturing procedure of microchannels and preclinical devices that imitate coronary bifurcations. Fabrication process is based on laser technologies and soft lithography techniques. Chapter 4 is devoted to the applications of the devices described in the previous chapter. They are biologically validated with endothelial cells and degradation of PDMS material with some solvents is solved by means of sol-gel coating. These chips are also employed for the experimental validation of low velocity zones in blood vessel bifurcations. Chapter 5 presents other applications of laser structuring in biomedicine, such as the fabrication of a CTCs capturing device or the surface modification of biocompatible materials in combination with Talbot effect. Finally, the main conclusions of the work are presented.

REFERENCES

[1] K. H. Herold and A. Rasooly, Eds., *Lab on a chip technology. Volume 1: Fabrication and microfluidics.* Norfolk: Caister Academic Press, 2009.

[2] Y. Temiz, R. D. Lovchik, G. V. Kaigala, and E. Delamarche, "Lab-on-a-chip devices: How to close and plug the lab?," *Microelectron. Eng.*, vol. 132, pp. 156–175, 2015.

[3] R. P. Feynman, "There's plenty of room at the bottom," *J. Microeleciromechanical Syst.*, vol. 1, no. 1, pp. 60–66, 1992.

[4] S. C. Terry, J. H. Jerman, and J. B. Angell, "A gas chromatographic air analyzer fabricated on a silicon wafer," *IEEE Trans. Electron Devices*, vol. 26, no. 12, pp. 1880-1886, 1979.

[6] R. Zengerle, A. Richter, and H. Sandmaier, "A micro membrane pump with electrostatic actuation," In Proc. IEEE Micro Electro Mech. Syst., 1992, pp. 19–24.

[6] F. C. M. Van de Pol, H. T. G. Van Lintel, M. Elwenspoek, and J. H. J. Fluitman, "A Thermopneumatic micropump based on micro-engineering techniques," *Sens. Actuators A*, vol. 21, no. 1-3 pp. 198–202, 1990.

[7] A. Emmer, M. Jansson, J. Roeraade, U. Linderberg, and B. Hock, "Fabrication and characterization of a silicon microvalve," *J. Microcolumn Separations,* vol. 4, no. 1, pp. 13-15, 1992.

[8] K. D. Wise and K. Najafi, "Microfabrication techniques for integrated sensors and microsystems," *Science*, vol. 254, no. 5036, pp. 1335–1342, 1991.

[9] S. T. Cho, K. Najafi, C. E. Lowman, and K. D. Wise, "An ultrasensitive silicon pressure-based microflow sensor," *IEEE Trans. Electron Devices*, vol. 39, no. 4, pp. 825–835, 1992.

[10] C. Niemeyer and C. Mirkin, Eds., *Nanobiotechnology*. Weinheim: Wiley-VCH Verlag GmbH & Co. KGaA, 2004.

[11] A. Manz, N. Graber, and H. A. Widmer, "Miniaturized total chemical analysis systems: a novel concept for chemical sensing," *Sens. Actuators B,* vol. 1, no. 1-6, pp. 244-248, 1990.

[12] www.webofknowledge.com

[13] D. Huh, G. A. Hamilton, and D. E. Ingber, "From 3D cell culture to organs-on-chips," *Trends Cell Biol.,* vol. 21, no. 12, pp. 745-754, 2011.

[14] M. A. McClain, C. T. Culbertson, S. C. Jacobson, N. L. Allbritton, C. E. Sims, and J. M. Ramsey, "Microfluidic devices for the high-throughput chemical analysis of cells," *Anal. Chem.,* vol. 75, no. 21, pp. 5646–5655, 2003.

[15] H. Lu, L. Y. Koo, W. M. Wang, D. A. Lauffenburger, L. G. Griffith, and K. F. Jensen, "Microfluidic shear device for quantitative analysis of cell adhesion," *Anal. Chem.*, vol. 76, no. 18, pp. 5257–5264, 2004.

[16] S. Takayama, E. Ostuni, P. LeDuc, K. Naruse, D. E. Ingber, and G. M. Whitesides, "Selective chemical treatment of cellular microdomains using multiple laminar streams," *Chem. Biol.,* vol. 10, no. 2, pp. 123-130, 2003.

[17] P. S. Dittrich and A. Manz, "Lab-on-a-chip: microfluidics in drug discovery," *Nat. Rev. Drug Discov*., vol. 5, no. 3, pp. 210–218, 2006.

[18] K. J. Jang and K. Y. Suh, “A multi-layer microfluidic device for efficient culture and analysis of renal tubular cells,” *Lab Chip*, vol. 10, no. 1, pp. 36–42, 2010.

[19] P. J. Lee, P. J. Hung, and L. P. Lee, “An artificial liver sinusoid with a microfluidic endothelial-like barrier for primary hepatocyte culture,” *Biotech. Bioeng.,* vol. 97, no. 5, pp. 1340-1346, 2007.

[20] M. Shin, K. Matsuda, O. Ishii, H. Terai, M. Kaazempur-Mofrad, J. Borenstein, M. Detmar, and J. P. Vacanti, “Endothelialized networks with a vascular geometry in microfabricated poly(dimethyl siloxane),” *Biomed. Microdevices*, vol. 6, no. 4, pp. 269–278, 2004.

[21] H. Kimura, T. Yamamoto, H. Sakai, Y. Sakai, and T. Fujii, “An integrated microfluidic system for long-term perfusion culture and on-line monitoring of intestinal tissue models,” *Lab Chip*, vol. 8, no. 5, pp. 741–746, 2008.

[22] E. K. Sackmann, A. L. Fulton, and D. J. Beebe, “The present and future role of microfluidics in biomedical research,” *Nature*, vol. 507, no. 7491, pp. 181–189, 2014.

[23] G. M. Whitesides, “The origins and the future of microfluidics,” *Nature*, vol. 442, no. 7101, pp. 368-373, 2006.

[24] L. Gervais, N. De Rooij, and E. Delamarche, “Microfluidic chips for point-of-care immunodiagnostics,” *Adv. Mater.*, vol. 23, no. 24, pp. H151-H176, 2011.

[25] P. Minzioni, R. Osellame, C. Sada, S Zhao, F G Omenetto, K. B. Gylfason , T. Haraldsson ,Y. Zhang, A. Ozcan, A. Wax, F. Mugele, H. Schmidt, G. Testa, R. Bernini, J Guck, C. Liberale, K Berg-Sørensen, J. Chen, M. Pollnau, S. Xiong, A. Liu, C. Shiue, S. Fan, D. Erickson, and D. Sinton, “Roadmap for optofluidics,” *J. Opt.*, vol. 19, no. 9, pp. 093003-093053, 2017.

[26] E. Verpoorte and N. F. De Rooij, "Microfluidics meets MEMS," *Proc. IEEE*, vol. 91, no. 6, pp. 930–953, 2003.

[27] H. Becker and C. Gartner, "Polymer microfabrications methods for microfluidic analytical applications," *Electrophoresis*, vol. 21, no.1, pp. 12–26, 2001.

[28] D. Brambley, B. Martin, and P. D. Prewett, "Microlithography: An overview," *Adv. Mater. Opt. Electron*., vol. 4, no. 2, pp. 55–74, 1994.

[29] M. Kufner and S. Kufner, *Micro-optics and lithography*. Brussels: VUB Press, 1997.

[30] C. Mack, *Fundamental Principles of Optical Lithography*. Chichester, West Sussex: Wiley, 2007.

[31] B. D. Gates, Q. Xu, M. Stewart, D. Ryan, C. G. Willson, and G. M. Whitesides, "New approaches to nanofabrication: Molding, printing, and other techniques," *Chem. Rev*., vol. 105, no. 4, pp. 1171–1196, 2005.

[32] L. Weber, W. Ehrfeld, H. Freimuth, M. Lacher, H. Lehr, and B. Pech, "Micromolding: a powerful tool for large-scale production of precise microstructures," In Micromachining and Microfabrication Process Technology II, vol. 2879, International Society for Optics and Photonics, 1996, pp. 156-168.

[33] U. M. Attia, S. Marson, and J. R. Alcock, "Micro-injection moulding of polymer microfluidic devices," *Microfluid. and Nanofluidics*, vol. 7, no. 1, pp. 1–28, 2009.

[34] M. Heckele and W. K. Schomburg, "Review on micro molding of thermoplastic polymers," *J. Micromechanics Microengineering*, vol. 14, no. 3, pp. R1-R14, 2004.

[35] H. Becker and U. Heim, "Hot embossing as a method for the fabrication of polymer high aspect ratio structures," *Sens. Actuators A*, vol. 83, no. 1, pp. 130–135, 2000.

[36] R. Truckenmüller, S. Giselbrecht, N. Rivon, E. Gottwald, V. Saile, A. van den Berg, M. Wessling, and C. van Bitterswijk, "Thermoforming of film-based biomedical microdevices," *Adv. Mater.*, vol. 23, no. 11, pp. 1311–1329, 2011.

[37] J. C. Mcdonald, D. C. Duffy, J. R. Anderson, and D. T. Chiu, "Review general fabrication of microfluidic systems in poly (dimethylsiloxane)," *Electrophoresis*, vol. 21, no. 1, pp. 27-40, 2000.

[38] X. M. Zhao, Y. Xia, and G. M. Whitesides, "Soft lithographic methods for nano-fabrication," *J. Mater. Chem.*, vol. 7, no. 7, pp. 1069–1074, 1997.

[39] Y. Xia and G. M. Whitesides, "Soft lithography," *Angew. Chem Int. Ed.,* vol. 37, no. 5, pp. 550–575, 1998.

[40] K. Ziolkowska, E. Jedrych, R. Kwapiszewski, J. Lopacinska, M. Skolimowski, and M. Chudy, "Chemical PDMS/glass microfluidic cell culture system for cytotoxicity tests and cells passage," *Sens. Actuators B,* vol. 145, no. 1, pp. 533–542, 2010.

[41] J. Anderson, D. Chiu, R. Jackman, O. Cherniavskaya, J. McDonald, H. Wu, S. Whitesides, and G. M. Whitesides, "Fabrication of topologically complex three-dimensional microfluidic systems in PDMS by rapid prototyping," *Anal. Chem.,* vol. 72, no. 14, pp. 3158-3164, 2000.

[42] Y. Hongbin, Z. Guangya, C. F. Siong, W. Shouhua, and L. Feiwen, "Novel polydimethylsiloxane (PDMS) based microchannel fabrication method for lab-on-a-chip application," *Sens. Actuators B,* vol. 137, no. 2, pp. 754–761, 2009.

[43] T. Fujii, "PDMS-based microfluidic devices for biomedical applications," *Microelectron. Eng.,* vol. 62, pp. 907–914, 2002.

[44] K. C. Chaw, M. Manimaran, F. E. H. Tay, and S. Swaminathan, "A quantitative observation and imaging of single tumor cell migration and deformation using a multi-gap microfluidic device representing the blood vessel," *Microvascular Research,* vol. 72, no. 3, pp. 153–160, 2006.

[45] J. C. McDonald and G. M. Whitesides, "Poly (dimethylsiloxane) as a Material for Fabricating Microfluidic Devices," *Acc. Chem. Res*., vol. 35, no. 7, pp. 491–499, 2002.

[46] J. C. Miller, Ed., *Laser ablation. Principles and applications.* Berlin: Springer-Verlag, 1994.

[47] J. R. Vázquez De Aldana, P. Moreno, and L. Roso, "Ultrafast lasers: A new frontier for optical materials processing," *Opt. Mater.,* vol. 34, no. 3, pp. 572–578, 2012.

[48] M. Malinauskas, A. Zukauskas S. Hasegawa, Y. Hayasaki, V. Mizeikis, R. Buividas, and S. Juodkazis, "Ultrafast laser processing of materials: from science to industry," *Light Sci. Appl.,* vol. 5, no. 8, pp. e16133-e16147, 2016.

[49] M. A. Roberts, J. S. Rossier, P. Bercier, and H. Girault, "UV laser machined polymer substrates for the development of microdiagnostic systems," *Anal. Chem.,* vol. 69, no. 11, pp. 2035–2042, 1997.

[50] B. B. Xu, Y. L. Zhang, H. Xia, W. F. Dong, H. Ding, and H. B. Sun, "Fabrication and multifunction integration of microfluidic chips by femtosecond laser direct writing," *Lab Chip,* vol. 13, no. 9, pp. 1677-1690, 2013.

[51] S. C. Wang, C. Y. Lee, and H. P. Chen, "Thermoplastic microchannel fabrication using carbon dioxide laser ablation," *J. Chromatogr. A,* vol. 1111, no. 2, pp. 252–257, 2006.

[52] X. Zhao and Y. C. Shin, "Femtosecond laser drilling of high-aspect ratio microchannels in glass," *Appl. Phys. A Mater. Sci. Process.,* vol. 104, no. 2, pp. 713–719, 2011.

[53] E. Waddel, "Laser micromachinig," in *Lab on a chip technology. Volume 1: Fabrication and microfluidics,* K. H. Herold and A. Rasooly, Eds. Norfolk: Caister Academic Press, 2009, pp. 173-184.

[54] K. Sugiola and Y. Cheng, *Femtosecond laser 3D micromachinig for microfluidics and optofluidic applications.* London: Springer, 2014.

[55] T. L. Chang, Z. C. Chen, Y. W. Lee, Y. H. Li, and C. P. Wang, "Ultrafast laser ablation of soda-lime glass for fabricating microfluidic pillar array channels," *Microelectron. Eng.,* vol. 158, pp. 95–101, 2016.

[56] F. He, Y. Cheng, Z. Xu, Y. Liao, J. Xu, H. Sun, C. Wang, Z. Zhou, K. Sugioka, K. Midorikawa, Y. Xu, and, X. Cheng, "Direct fabrication of homogeneous microfluidic channels embedded in fused silica using a femtosecond laser," *Opt. Lett.,* vol. 35, no. 3, pp. 282–284, 2010.

[57] E. T. Carlen, J. G. Bomer, J. W. van Nieuwkasteele, and A. van den Berg, "Silicon and glass micromachining," in *Lab on a chip technology. Volume 1: Fabrication and microfluidics,* K. H. Herold and A. Rasooly, Eds. Norfolk: Caister Academic Press, 2009, pp. 83-114.

[58] P. Abgrall and A. M. Gué, "Lab-on-chip technologies: Making a microfluidic network and coupling it into a complete microsystem - A

review," *J. Micromechanics Microengineering*, vol. 17, no. 5, pp. R15-R49, 2007.

[59] A. Kumar and G. M. Whitesides, "Features of gold having micrometer to centimeter dimensions can be formed through a combination of stamping with an elastomeric stamp and an alkanethiol 'ink' followed by chemical etching," *Appl. Phys. Lett*., vol. 63, no. 14, pp. 2002–2004, 1993.

[60] D. C. Duffy, J. C. McDonald, O. J. A. Schueller, and G. M. Whitesides, "Rapid prototyping of microfluidic systems in poly(dimethylsiloxane)," *Anal. Chem.*, vol. 70, no. 23, pp. 4974–4984, 1998.

[61] M. K. Chaudhury and G. M. Whitesides, "Direct measurement of interfacial interactions between semispherical lenses and flat sheets of poly(dimethylsiloxane) and their chemical derivatives," *Langmuir*, vol. 7, no. 5, pp. 1013–1025, 1991.

[62] T. Thorsen, S. J. Maerkl, and S. R. Quake, "Microfluidic large-scale integration," *Science*, vol. 298, no. 5593, pp. 580–585, 2002.

[63] S. R. Quake and A. Scherer, "From micro to nanofabrication with soft materials," *Science*, vol. 290, no. 5496, pp. 1536-1540, 2000.

[64] J. N. Lee, C. Park, and G. M. Whitesides, "Solvent compatibility of poly(dimethylsiloxane)-based microfluidic devices," *Anal. Chem*., vol. 75, no. 23, pp. 6544–6554, 2003.

[65] A. R. Abate, D. Lee, C. Holtze, A. Krummel, T. Do, and D. A. Weitz, "Functionalized glass coating for PDMS microfluidic devices," in *Lab on a chip technology. Volume 1: Fabrication and microfluidics,* K. H. Herold and A. Rasooly, Eds. Norfolk: Caister Academic Press, 2009, pp. 17-30.

[66] M. W. Toepke and D. J. Beebe, “PDMS absorption of small molecules and consequences in microfluidic applications,” *Lab Chip*, vol. 6, no. 12, pp. 1484–1486, 2006.

[67] K. Ren, J. Xhou, and H. Wu, “Materials for microfluidic fabrication,” *Acc. Chem. Res*, vol. 46, no. 11, pp. 2396-2406, 2013.

[68] A. P. Golden and J. Tien, “Fabrication of microfluidic hydrogels using molded gelatin as a sacrificial element,” *Lab Chip*, vol. 7, no. 6, pp. 720-725, 2007.

[69] A. W. Martinez, S. T. Phillips, and G. M. Whitesides, “Diagnostics for the developing world: Microfluidic paper-based analytical devices,” *Anal. Chem*., vol. 82, no. 1, pp. 3–10, 2010.

[70] A. Nilghaz, D. H. B. Wicaksono, D. Gustiono, F. A. Abdul Majid, E. Supriyanto, and M. R. Abdul Kadir, “Flexible microfluidic cloth-based analytical devices using a low-cost wax patterning technique,” *Lab Chip*, vol. 12, no. 1, pp. 209–218, 2012.

2. MATERIALS, FABRICATION INSTRUMENTS AND CHARACTERIZATION TOOLS

The general aim of this work is to structure different materials with laser technologies for fabricating several fluidic devices for their application as biomedical devices. In this chapter, materials and instrumentation employed for this purpose are presented, as well as their characteristics. One of these devices is a particular structure of channel that imitates a blood vessel and its master is fabricated over soda-lime glass. Soda-lime glass is widely used throughout this theses, also for other devices, due to its low cost. This substrate is chemically and optically analysed by means of energy dispersive X-ray (EDX) analysis and photospectrometer techniques, respectively. Also polydimethylsiloxane, material for the replication of the channels, and sol-gel compositions, for the coating of the devices, are presented.

For the manufacturing of the structures, five different laser systems are employed through this thesis. For fabricating the master of the channels in soda-lime glass via indirect ablation (see Section 3.3), a nanosecond pulse duration diode pumped Nd:YVO_4 laser is employed. Posterior thermal treatments are sometimes required in order to modify the roughness of the surface in a controlled way. For this purpose, the applicability of a CO_2 laser combined with a roller furnace in comparison with a conventional treatment with a static furnace is evaluated. Moreover, for studying the dependence of direct ablation needed for fabricating other kind of devices (see Section 3.2) with the pulse duration, microchannels are fabricated over glass with three different laser systems: working in the nanosecond regime, the above-mentioned Nd:YVO_4, another with the same active medium working in the picosecond regime and a Ti:Shappire laser with pulse duration of a hundred femtoseconds. Finally, for one of the

applications of laser microstructuring to enhance the attachment of cells to the biomaterials used, a Nd:YAG laser is employed for ablation of titanium and tantalum surfaces.

Other instrumentation used through this work, like a plasma cleaner for bonding the PDMS channels or characterization tools such as microscopes, are also detailed in this chapter.

2.1. MATERIALS

2.1.1. Soda-lime glass

In this thesis soda-lime glass is employed as substrate for fabricating the structures by means of direct and indirect laser ablation. As it was mentioned in Chapter 1, glass presents valuable characteristics like robustness, chemical resistance or optical transparency. Moreover, soda-lime glass used for these experiments has the advantage of cheap price since it is obtained from local suppliers. The transmission spectrum of this material is analysed by using a PerkinElmer Lambda 25 spectrometer. The resulting graph is shown in Figure 2.1.

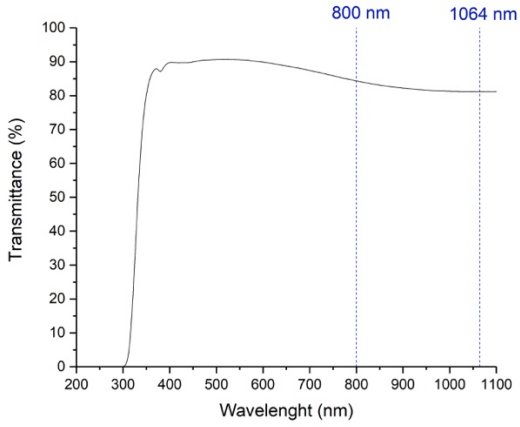

Figure 2.1: Optical transmission of commercial soda-lime glass from 190 to 1100 nm wavelength.

As it can be observed in Figure 2.1, soda-lime glass is highly absorbent in the ultraviolet region and transparent in the visible wavelengths, which is suitable for microscope inspections. In the infrared regime it is quite non-absorbent with a transmittance value of approximately 80% at 1064 nm and 85% at 800 nm. This is the spectral range where the lasers employed in this thesis for glass machining operate. Light absorbance of the material is not a linear process and ablation involves other physical phenomena that will be explained in Chapter 3.

Soda-lime glass is also chemically analysed using EDX in Zeiss FESEM-Ultra Plus scanning electron microscope (SEM). Both sides of the material are evaluated and results are presented in Table 2.1.

Undoped side elements	Weight %
O	50.25
Si	33.08
Na	9.08
Ca	4.87
Mg	2.19
Al	0.53

Doped side elements	Weight %
O	48.97
Si	32.34
Na	9.14
Ca	4.91
Mg	2.24
Al	0.49
Sn	1.91

Table 2.1: Chemical composition of areas of soda-lime glass in both sides of the substrate.

According to the data presented in Table 2.1, in both surfaces of soda-lime glass silicon dioxide (SiO_2) is the main component. To this fused silica proportion, a "soda" part is added, sodium oxide (Na_2O) from soda ash, which lows the transition temperature of the glass. "Lime" part is presented in form of calcium oxide (CaO) from limestone or dolomite, which confers durability to the material. Also for this purpose, magnesium oxide (MgO) from dolomite and aluminium oxide (Al_2O_3) from feldspar are added to the mix. The analysis reveals that there is a significant difference between both sides of the material: in one side of the glass there is a presence of tin

(doped side), whereas in the other one there is not (undoped side). These impurities derive from the fabrication process of glass, known as floating glass. In the first steps, all the raw materials are mixed and melted into a furnace that reaches temperatures up to 1500 ºC. Then, the molten glass is floated over a film of molten tin in order to cool it down, obtaining a plane sheet of glass with uniform thickness. Transference of tin to the side of the glass that is in contact with the metal occurs during this process. These dopants will play a key role in ablation process as we will explain in the next chapter. Due to its characteristics, soda-lime glass is presented as a suitable material for laser microstructuring but its impermeability does not allow to perform long term cell cultures.

2.1.2. Polydimethylsiloxane

Polydimethylsiloxane (PDMS) is employed for the replication of the soda-lime master in order to create the final device that imitates a coronary bifurcation, one of the purposes of this thesis. The PDMS employed in this work is Sylgard 184 from Dow Corning. It is presented in two parts, one elastomer base and one hardener. Following fabricant indications, this to parts should be mixed in a ratio 10:1, respectively, in order to obtain the elastomer. Nevertheless, in some parts of this work, this relation is modified for sealing the PDMS device.

Figure 2.2: Presentation of Sylgard 184 from Down Corning.

Table 2.2 shows the specifications of the material [1].

Property	Value
Viscosity (base)	5.2 Pa·s
Viscosity (uncured mix 10:1)	3.5 Pa·s
Specific gravity (uncured)	1.03
Specific gravity (cured)	1.04
Work life at 25 °C	1.4 hours
Cure time at 25 °C	48 hours
Cure time at 100 °C	35 minutes
Shelf life at 25 °C	24 months
Tensile strength	7.1 MPa
Elongation	120 %
Shore hardness (type A)	44
Refractive index at 589 nm	1.4118
Refractive index at 632.8 nm	1.4225
Refractive index at 1321 nm	1.4028

Table 2.2: Properties of 184 Sylgard, Dow Corning.

2.1.3. Sol-gel coatings

Sol-gel methods have been applied for the synthesis of gradient refractive index materials [2], thin film fabrication [3], sensors [4, 5], or to optimize optical and morphological properties of surfaces [6], among others. Advantages of this method are low temperature processing, the possibility to obtain thin coating, the control of chemical composition and the easy coating of large surfaces. Some limitations of the technique are long time process and the cost of the materials [7]. In this work, sol-gel films are employed for coating PDMS channels with the purpose of maintaining their biocompatibility after using organic solvents.

Sol-gel process basically consists in the evolution of inorganic networks through the formation of a colloidal suspension or sol and to its gelation to form a gel. A sol is a colloidal suspension of solid

particles in a liquid. In these suspensions, gravitational forces are negligible and the interactions are dominated by short-range forces. When a molecule reaches macroscopic dimensions and it extends through all the solution, it is called gel. Gel point is considered when the last bond that completes this big molecule is formed and a gel is understood as a solid skeleton that contains a liquid phase. Gels can be formed from sols when attractive forces cause them to stick together and to form a network [8].

Essentially, sol-gel processes follow the next steps: (i) preparation of a precursor solution, (ii) transformation of the starting compounds into a sol by applying a proper treatment with reagents, (iii) allowance of the sol to change into a gel by polycondensation, (iv) gel shaping to the final form and (v) thermal treatment application to convert the gel into the final material.

In this work, silica titania and silica (SiO_2-TiO_2 and SiO_2, respectively) thin films are prepared via sol-gel methods for coating the PDMS channels by following the next procedures:

- SiO_2-TiO_2 sol is fabricated using methyltriethoxysilane (MTES) and titanium isopropoxide (TISP) as precursors of silica and titania sol, respectively (MTES/TISP sol). First, MTES is pre-hydrolysed by using ethanol as solvent. Then HCl (0.1N) is added and the mix is stirred for one hour at room temperature with a magnetic agitator. TISP is complexed by mixing ethanol and glacial acetic acid and also maintaining the solution under agitation for one hour. Then, MTES and TISP solutions are mixed and distilled water is added, drop by drop, to complete the hydrolysis process. Solutions with molar ratios 70/30 and 80/20 MTES/TISP, respectively, are employed in this thesis.

- SiO_2 sol is made from MTES and tetraethoxysilane (TEOS) precursors in a molar ratio 60/40. This sol is prepared in ambient conditions by mixing MTES and TEOS with absolute ethanol. Then, acidulated water is added drop by drop. Finally,

distilled water is incorporated to the sol and it is refluxed in a water bath at 40 ºC for two hours under continuous magnetic agitation.

2.2. LASER SYSTEMS

2.2.1. Rofin PowerLine E

This diode end-pumped Nd:YVO_4 laser system is the most employed one through this thesis since is the one used for manufacturing the blood vessel like channels via indirect laser writing, microchannels by direct ablation and the CTCs capturing device . This Q-switched laser has a pulse duration of 20 ns and a fundamental wavelength of 1064 nm, which corresponds to the infrared spectral range. Beam quality factor is M^2<1.3. Laser average power is up to 20 W, adjustable by controlling the amperage applied to the diodes, which is up to 45 A. The number of pulses per second can also be selected from single shot to 200 kHz repetition rate. A picture of the system is shown in Figure 2.3.

Figure 2.3: Image of Rofin PowerLine E laser system.

For addressing the beam, the setup has a galvanometer system composed by two mirrors that address the beam and move to write the pattern over the substrate. The beam is focused by using a flat field lens of 100 mm focal length that ensures a homogeneous irradiance working area of 80x80 mm^2. In this case, beam radius at focal distance is 9 μm. Other lenses can also be implemented in this equipment in order to have a larger working area.

The system is equipped with a commercial software that allows us to design the desired pattern directly in the software or to import the design via CAD files. It also controls the laser parameters employed and the hatching of the designs if needed. Moreover, it allows suppressing the first laser pulses of the exposure, since those are more energetic than the others due to the Q-switch technique.

2.2.2. Coherent Lumera Super Rapid HE

Coherent Lumera Super Rapid HE laser is employed for the fabrication of microchannels over soda-lime glass via direct laser ablation in the picosecond temporal regime. This Q-switch Nd:YVO_4 laser has 12 ps pulse duration and 1064 nm fundamental wavelength. Beam quality factor is M^2<1.3. Repetition rate can be adjusted from 0 to 1000 kHz and average power depends on this parameter, going from 2 W at 10 kHz to 10 W at 1000 kHz.

The system is composed by a processing head with fixed lens and a motorized platform. In the assembly employed in this work, a 5x beam expander is used, achieving a beam radius of 16 μm. Stages can move at a velocity of up to 1000 mm/s and are controlled by laser processing system ILS 500x from InnoLas, which allows moving the sample in order to obtain the desired pattern.

Figure 2.4: General view of the Coherent Lumera Super Rapid HE installation.

2.2.3. Spectra Physics Spitfire

The Spectra Physics Spitfire system is a Ti:Shappire laser with two amplification stages, emitting pulses of 100 fs duration and central wavelength of 800 nm. One output delivers pulses with 50 mJ at 10 Hz and the other one, which is going to be employed in this work for manufacturing channels in the femtosecond regime, emits pulses with maximum energy of 1 mJ at a fixed repetition rate of 1 kHz. The nearly gaussian beam has a M^2<1.3 and it is focused by an achromatic lens of 200 mm focal length, obtaining a beam radius of 11 μm at focus. The sample is fixed on a computer-controlled 3 axes monitored stage that precisely moves the substrate to obtain the final structure. Stages can move from 1 μ/s to 5 mm/s.

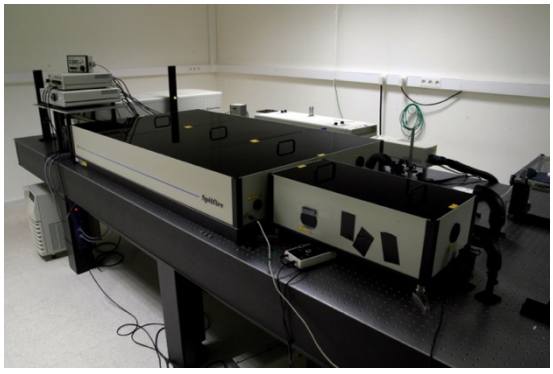

Figure 2.5: Image of the Spectra Physics Spitfire femtosecond system.

2.2.4. Easy Mark 100

Easy Mark 100 system is a Q-switch CO_2 laser, typically employed for materials treatment. In this work, it is employed as probe of concept to evaluate the suitability of this technique for reducing the roughness in the soda-lime channels that imitate the coronary bifurcations. It has a pulse duration of 10 μs and fundamental wavelength of 10.6 μm. The beam quality factor takes a value of M^2<1.25. Laser average power can be controlled from 0 to 124 W of maximum power. Repetition rate of pulses is also adjustable and goes from single shot to 100 kHz. In order to focus the beam over the sample, a flat field lens of 1 m focal length is employed, ensuring a working area of 120x120 mm^2. This system also has a galvanometer system composed by mirrors that can be controlled via computer to create a laser exposure pattern. For thermal treatments, this laser is combined with a roller furnace that will be presented in the next section [9]. An image of the system is depicted in Figure 2.6.

Figure 2.6: Easy Mark 100 laser system.

2.2.5. Spectra Physics Quanta Ray

Finally, Spectra Physics Quanta Ray laser is presented. This Q-switched Nd:YAG laser is employed in this work for the microstructuring of titanium and tantalum materials. The system operates in the nanosecond temporal regime and its central wavelength is 1064 nm. This equipment has the possibility to generate the second, third and fourth harmonic, obtaining the wavelengths of 532 nm, 355 nm and 266 nm, respectively. This covers from the near infrared spectral range to the ultraviolet, making this laser a very versatile system. Pulse duration is 7 ns for 532 nm wavelength. Repetition rate is fixed at 50 Hz and energy per pulse is 200 mJ at 1064 nm, 70 mJ at 532 nm, 30 mJ at 355 nm and 15 mJ at 266 nm. Beam quality factor is $M^2<1.2$.

Figure 2.7: Spectra Physics Quanta-Ray laser system.

2.3. OTHER EQUIPMENT

2.3.1. Nannetti LKN 86 furnace

The Nannetti LKN 86 furnace is employed for applying thermal treatments to the samples, both soda-lime glass and PDMS. It has external dimensions of 500x750x750 mm^3 and weights 86 kg. The inside of the furnace is made of insulating low density refractory brick and is 200x300x150 mm^3 dimension. It reaches a maximum

temperature of 1340 ºC. This furnace has a temperature ramp that allows controlling the initial, process and final temperatures of the samples, as well as the time of heat exposition. The furnace has a power of 4 kW and voltage of 230 V [10].

Figure 2.8: Nannetti LKN 86 furnace.

2.3.2. Nannetti ER20 roller furnace

Nannetti ER20 furnace is a roller furnace that allows gradually heating up or cooling down the sample through the different zones it possess. Moreover, it has a superior opening that allows combining furnace thermal treatment with laser exposure. In particular, in this work, it is combined with the Easy Mark 100 CO_2 laser (see Figure 2.6). Its dimensions are 3400x1100x1550 mm^3 and weights 350 kg. Samples advance through the furnace thanks to ceramic rolls, with 20 mm diameter and separation between them of 38.1 mm. They move thanks to a sprocket system of adjustable velocity, controlled by means of the amperage of the motor. It reaches 7700 mm/h with 1000 mA. The system is equipped with four independent temperature controllers, one for each zone: preheating, firing 1, firing 2 and cooling. It reaches a maximum temperature value of 1330 ºC [11].

Figure 2.9: Nannetti ER 20 roller furnace.

2.3.3. Diener Zepto plasma cleaner

Diener Zepto plasma cleaner is employed for sealing the PDMS devices. By means of this technique, PDMS-PDMS or PDMS-glass bonding can be achieved. The process consists in the chemical modification of the surface of materials when exposed to a plasma created from gases. For our purposes, the plasma process is performed under oxygen atmosphere. Plasma cleaning has other applications besides bonding such as cleaning by removing organic layers, surface activation prior gluing or lacquering, etching or coating by plasma polymerization [12].

The plasma cleaner has 425x450x185 mm^3 dimensions and the chamber has a diameter of 105 mm and 300 mm length. It has a generator of 13,56 MHz and power is adjustable up to 200 W. Time of plasma exposure is also adjustable. The machine is connected to a high purity oxygen bottle and to a rotatory pump Pfeiffer DUO 5.0 with maximum capacity of 5 m^3/h.

It has a rotatory control that guides us through the different steps of the process. First, vacuum is performed into the chamber. Once the pressure is achieved, gas comes into the chamber. This model has twos gas entries, allowing the mixture of gases. Then, the generators are activated and plasma exposure begins. Finally, atmospheric pressure is established and the process ends.

Figure 2.10: Diener Zepto plasma cleaner.

2.3.4. Ismatec Reglo Digital pump

This peristaltic pump is employed for performing flux assays with the fabricated devices. It has 178x100x135 mm^3 dimensions and weights 2 kg. This model has 12 roller pumps that does not allow as much flow rate as pumps with less rollers but less pulsation can be obtained in this way. It has two different channels where individual tubing can be selected, from 0.13 to 3.17 mm of internal diameter. Flow rate goes from 0.002 ml/min to 38 ml/min. The speed is digitally selected and the pump allows different operating modes, like pumping by flow rate, by drive speed (from 1.6 to 160 rpm), dispensing by volume or dispensing by time, among others [13].

Figure 2.11: Ismatec Reglo Digital peristaltic pump.

2.3.5. N-Biotek portable Mini CO_2 incubator

This compact incubator is employed for cell culture in incubation conditions (37 ºC temperature, 5% CO_2 and 80% humidity) and in a sterilized environment. It has 292x333x433 mm^3 total dimensions with a chamber of 15.2 litres and 224x200x340 mm^3 inner dimensions. It weights 6.8 kg and allows portable use with carrying handle. Temperature and CO_2 can be digitally controlled, with a range from 15 ºC to 45 ºC with an accuracy of 0.25 ºC and CO_2 range from 0 to 20% and 1% accuracy. The incubator is heated and cooled by Peltier effect and air circulates by fan. It has two stainless steel shelves and natural humidification by water pan. A hole of 12 mm in a lateral allows the performance of sterile flux experiments with the pump outside the incubator [14].

Figure 2.12: N-Biotek portable CO_2 incubator.

2.4. CHARACTERIZATION TOOLS

2.4.1. Nikon MM-400 microscope

This metallurgic microscope is employed for optical inspection of samples in transmission and reflexion mode. It has two light sources, diascopic and episcopic, composed by white LEDs. Optical head is binocular and has 300x600x638 mm^3 dimensions and 50 kg weight. Axis movement is manual and it allows non-contact measurements in the three axes. Maximum workpiece height in this instrument is

150 mm. The microscope is combined with a CCD camera and software that permits the acquisition and treatment of images. The microscope is equipped with three LU Pan Fluor series microscope objectives: 5x/0.15, 20x/0.45 and 100x/0.90 [15].

Figure 2.13: Nikon MM-400 microscope.

2.4.2 Sensofar S neox non-contact surface profiler

The Sensofar S neox non-contact surface profiler combines three measurement techniques in one apparatus. These technologies are: confocal microscopy, vertical scanning interferometry and focus variation [16].

Confocal microscopy is a wide know technique that basically consist in the employment of a pinhole for blocking out of focus light, prevented from entering the system, and only information in the focal plane is captured. By this method, optical resolution significantly increases. By scanning the aperture and capturing multiple two dimension images at different depths, 3D image of the sample can be reconstructed as well as 2D profiles. This technique is suitable for measuring very rough surfaces and sharp slopes.

Interferometry microscopy is based on the different path travelled by two separated beams (reference and sample) to yield a spatial interference pattern that contains information of the topography of the

sample. Great resolution is obtained but the main disadvantage of this technique is that the surface must be very smooth and it is difficult to measure step topographies.

Focus variation vertically scans the sample to obtain a continuous set of images of the surface. An algorithm determines which are the points in focus in each frame and creates an image of the sample as well as a 3D surface. It is the most resolution limited of the three techniques and has no international standard. It is also no suitable for mirror like surfaces. Nevertheless, is an easy to use and versatile technique very suitable for rapid measurements and for sharp slopes.

Maximum values, since are objective dependant, of some parameters of the abovementioned techniques are summarized in Table 2.3.

	Focus variation	Confocal	Interferometry
Z repeatability (nm)	200	1-40	1
Lateral resolution (μm)	0.8	0.3	0.5
Maximum slope (°)	86	72	40
Measurement range (mm)	37	37	10

Table 2.3: Comparison among field of view, confocal and interferometry techniques.

Figure 2.14: Sensofar S neox non-contact surface profiler.

The profiler has 600x569x389 mm^3 dimension and is equipped with four light sources: red, green, blue and white red, optimizing the light source for each application. In this moment, the equipment has six different objectives: one group of TU Plan Fluor objectives with magnifications 10x, 20x and 50x for confocal and focus variation techniques and other three with the same magnification for interferometry microscopy. In Table 2.4, some properties of the brightfield objectives are presented.

Magnification	10x	20x	50x
NA	0.30	0.45	0.80
Work distance (mm)	17.5	4.5	1
Field of view (µm)	1700x1420	850x710	340x284
Spatial sampling (µm)	1.38	0.69	0.28
Optical resolution (µm)	0.46	0.31	0.17

Table 2.4: Characteristics of the brightfield objectives of the Sensofar S neox profiler.

2.4.3. Zeiss Axio Vert.A1 microscope

Zeiss Axio Vert.A1 is an inverted transmitted light and reflected light fluorescence microscope that works under this phenomenon. Briefly, fluorescence consists in the excitation of an organic or inorganic compound with certain wavelength resulting in the subsequent emission of longer wavelength light from the sample. This emission of light is nearly simultaneous. Basically, a fluorescence microscope operates by irradiating the sample with a specific band of wavelengths and separating the excitation light from the fluorescent emitted radiation, which is much weaker than the first, by a dichroic mirror. There are plenty of materials that show autofluorescence under particular illumination. Moreover, numerous stains or fluorochromes, which attach to specific materials and allow fluorescence inspections, have been developed. Fluorescence microscopy has contributed enormously to biology and biomedical sciences, allowing identifying cells or even sub-cellular structures. Some characteristics of this microscope are showed in Table 2.5 [17].

Figure 2.15: Zeiss Axio Vert.A1 microscope.

Fluorescence reflected light illumination	Via exchangeable LED modules Selectable wavelengths: 365 nm, 385 nm, 420 nm, 445 nm, 455 nm, 470 nm, 505 nm,530 nm, 590 nm, 615 nm, 625 nm
Transmitted light illumination	LED illumination, wavelength from 400 nm to 700 nm, peak at 460 nm
LED illuminator (transmitted light)	Maximum power consumption 3 W Infinitely light source adjustability from <1.5 V to 12 V
Stand with objective focusing	Coarse focus 4 mm per rotation Fine focus 0.4 mm per rotation Total focusing range 13 mm
Objectives	Set of ICS objectives with M27 thread Manual change of objectives via five-position nosepiece A-Plan 10x/0.25 Dry EC Plan-Neofluar 20x/0.5 Dry LD A-Plan 20x/0.35 Dry LD A-Plan 40x/1.54 Dry Plan-APOCHROMAT 63x/1.4 Oil
Field of view	23 mm
Dimensions	235x560x560 mm
Weight	10.5 kg

Table 2.5: Some properties of fluorescence microscopy Zeiss Axio Vert.A1.

2.4.4. Leica TSC SP8 confocal microscope

Figure 2.16: Leica TSC SP8 confocal microscope.

Leica TSC SP8 microscope combines two techniques that were previously mentioned: confocal and fluorescence microscopy. By employing a pinhole, any fluorescent signal coming from out-of-focus planes is supressed and high resolution images are obtained. As in non-fluorescent confocal microscopy, 3D images are acquired by scanning different focal planes and stacking the images. Some characteristics of this equipment are listed in Table 2.6 [18].

Continuous wave lasers	UV diode 405 nm Solid state laser 20 mW 488 nm Solid state laser 20 mW 552 nm Solid state laser 20 mW 549 nm Solid state laser 30 mW 638 nm
Detection range	400 - 800 nm
Pinhole	Stable single pinhole Pinhole diameter motorized by software
Resolution	From 512 x 512 px to 8000 x 8000 px
Objectives	HC PL FLUOTAR 5x/0.15 Dry HC PL APO CS 2 10x/0.4 Dry HC HC PL APO CS 2 20x/0.75 Dry FluotarVISIR 25x/0.95 Water HC PL APO CS 2 40x/1.30 Oil HC PL APO CS 2 63x/1.4 Oil
Field of view	22 mm
Dimensions	1100x2300x1750 mm
Weight	330 kg

Table 2.6: Some properties of confocal fluorescence microscopy Leica TSC SP8.

2.4.5. Zeiss FESEM-Ultra Plus scanning electron microscope

Scanning electron microscopy (SEM) is a microscopy technique that produces images by focusing a beam of electrons over the sample. Electrons interact with the atoms in the sample and the emitted signals contain information about the topography and composition of the sample. The electron beam scans over the sample and a 2D image of the surface is obtained with nanometre resolution.

This Zeiss FESEM-Ultra Plus SEM [19] works at high vacuum with field emission scanning electron microscope (FESEM) illumination system, which differs from conventional SEM in the electron generation, providing much focused electron beams and subsequently, higher resolution. Taken together with its charge compensation system by nitrogen injection, minimises charging effects on non-conductive samples.

It is equipped with energy dispersive X-ray (EDX) spectroscopy system that chemically analyses a localized area, line or point of the sample by detecting the X-ray radiation emitted by the sample. Since X-ray scattered energy is characteristic of each element, it offers a qualitative and semi-quantitative microanalysis of the composition of the sample. In this system, a resolution of 129 eV at working distance of 8.5 mm and voltage of 20 kV is obtained.

Figure 2.17: Zeiss FESEM-Ultra Plus scanning electron microscope.

Some characteristics of Zeiss FESEM-Ultra Plus SEM are listed below in Table 2.7.

Detectors	Secondary electron detector In Lens Secondary electron detector Everhart-Thornley Electron selective backscattered electron EsB Angles selective backscattered electron AsB STEM X-ray Oxford Inca
Resolution	0.8 nm at 30 kV (STEM mode) 1 nm at 15 kV and working distance 2 mm 1.7 nm at 1 kV and working distance 2 mm 3.5 nm at 0.2 kV and working distance 2 mm 4 nm at 0.1 kV and working distance 2 mm
Acceleration voltage	0.02 kV-30 kV, adjustable with 10 V steps
Magnification	12-1 000 000x
Working distance	1-50 mm
Chamber dimensions	330 mm ∅ x 270 mm length
Maximum sample weight	0.5 kg

Table 2.7: Characteristics of the Zeiss FESEM-Ultra Plus microscope.

2.4.6. PerkinElmer Lambda 25 spectrometer

PerkinElmer Lambda 25 spectrometer is employed for obtainig the transmittance spectrum of samples from 190 to 1100 nm wavelength. Its bandwidth is fixed with a slit of 1 nm. Wavelength accuracy at D_2 peak (656.1 nm) is ±0.1 nm. Wavelength reproducibility with 10 measurements at 656.1 nm is ±0.5 nm. This tool has applications in routine UV/Vis testing, in liquid analysis or pharmacopeia and regulatory test, among others [20].

Figure 2.18: PerkinElmer Lambda 25 spectrometer.

REFERENCES

[1] Dow Corning, "184 Silicone Elastomer", 11-1792-01, Jan. 2010.

[2] S. Konishi, K. Shingyouchi, and A. Makishima, "r-GRIN glass rods prepared by a sol-gel method," *J. Non-Cryst. Solids*, vol. 100, no. 1-3, pp. 511-513, 1988.

[3] C. J. Brinker, A. J. Hurd, P. R. Schunk, G. C. Frye, and C. S. Ashley, "Review of sol-gel thin film formation," *J. Non-Cryst. Solids*, vol. 147, pp. 424-436, 1992.

[4] B. C. Dave, B. Dunn, J. S Valentine, and J. I. Zink, "Sol-gel encapsulation methods for biosensors," *Anal. Chem*., vol. 66, no. 22, pp. 1120A-1127A, 1994.

[5] R. Zusman, C. Rottman, M. Ottolenghi, and D. Avnir, "Doped sol-gel glasses as chemical sensors," *J. Non-Cryst. Solids*, vol. 122, no. 1, pp. 107-109, 1990.

[6] D. Nieto, A. I. Gómez-Varela, Y. C. Martín, G. M. O'Connor, and M. T. Flores-Arias, "Improvement of the optical and morphological properties of microlens arrays fabricated by laser using a sol–gel coating," *Appl. Surf. Sci*., vol. 351, pp. 697-703, 2015.

[7] A. I. Gómez-Varela, Y. Castro, A. Durán, P. A. A. De Beule, M. T. Flores-Arias, and C. Bao-Varela, "Synthesis and characterization of erbium-doped SiO 2 -TiO2 thin films prepared by sol-gel and dip-coating techniques onto commercial glass substrates as a route for obtaining active GRadient-INdex materials," *Thin Solid Films*, vol. 538, pp. 115-121, 2015.

[8] C. J. Brinker and G. W. Scherer, *Sol-Gel Science: The Physics and Chemistry of Sol-Gel Processing*. San Diego Academic Press, Inc., 1990.

[9] L.C. Estepa and G.F. De la Fuente, "Continuous furnace with coupled laser for the surface treatment of materials," U.S. Patent 20090230105 A1, 7 March 2006.

[10] https://www.nannettisrl.it/Joomla/index.php/it/forno-serie-lkn

[11] https://www.nannettisrl.it/Joomla/index.php/it/forno-a-rulli-serie-er

[12] Diener, "Plasma Technology", Sep. 2007.

[13] http://www.n-biotek.com

[14] http://www.ismatec.com/int_e/pumps/t_reglo/reglo.htm

[15] Nikon, "Measuring Microscopes, MM-Series", 2CE-IHMH-4, Apr. 2018.

[16] https://www.sensofar.com/metrology/sneox

[17] Zeiss, "Operating Manual Axio Vert.A1 Inverted Microscope", 431030-7044-001, Jan. 2012.

[18] Leica, "Leica TCS SP8 Technical Documentation", Mar. 2018.

[19] http://www.usc.es/gl/investigacion/riaidt/microscopia/modules/equipamento/varrido/equipamento_0005.html

[20] PerkinElmer, "Lambda 25/35/45", 006658F_01, 2011.

3. FABRICATION OF PRECLINICAL DEVICES BY LASER TECHNOLOGIES

In this chapter, the fabrication of preclinical devices by laser ablation over soda-lime glass is presented. As it was explained in the introduction of this work, the applications of these chips are numerous and there are several fabrication techniques for obtaining these structures. Among all of them, laser ablation outstands due to characteristics like versatility, accuracy, non-contact nature or process speed. Depending on the final dimension of the channels, there exist different ablation techniques for their fabrication. For manufacturing micrometre structures for microfluidic devices, direct laser ablation is presented as the most suitable method. Channels with dimensions in the in the range of microns can be fabricated with high precision thanks to the size of the laser beam at the focal plane. If millimetre sizes are required, indirect methods are more appropriate. In particular, these structures will be employed for the fabrication of devices that imitate large structures like blood vessels, which are in the millimetre order. Main ablation mechanism, as well as physical phenomena involved regarding the laser pulse duration and the substrate material, are explained in this chapter. Direct and indirect methods are employed for the fabrication of micrometer and millimeter channels, respectively. In the case of direct ablation, channel fabrication is studied for three different temporal regimes. For larger channels, which will be employed for organ-on-a-chip applications, glass substrate results problematic for long term cell cultures due to its non-permeability to gases. For this reason, the channels are replicated in PDMS, which allow gas exchange and is presented as in ideal material for our purpose.

3.1. PRINCIPLES OF LASER ABLATION

As it was mentioned in Chapter 1, laser ablation consists in the removal of material by focusing an intense laser beam on a material. This technique outstands due to its accuracy, versatility and process speed, among other characteristics. By this method, micrometer scale features can be obtained over different material surfaces. Physical phenomena involved in laser ablation depend on the substrate to structure and on the characteristics of the laser beam, in particular wavelength and pulse duration. Basically, a target under laser irradiation absorbs the energy and a subsequent transformation of matter occurs. The first step in this process is the absorption of light energy by the material. These mechanisms are different in absorbent materials to the laser wavelength, such as metals, from the ones in transparent dielectric substrates, like glasses or plastics [1]. These absorption phenomena also depend on the pulse duration of the laser. Electron-lattice relaxation time (τ_r) is in the range of picoseconds, so material behaviour is conditioned by the relation between relaxation time and laser pulse duration (τ_p). Pulses are considered long when τ_r is shorter than pulse duration, like in nanosecond pulses. When the time of energy transference to the lattice is longer than the pulse duration, laser pulses are considered ultrashort.

When working with absorbent materials to the laser wavelength and long pulse durations, where $\tau_p >> \tau_r$, linear absorption is the main dominant effect. There is a large density of free electrons that absorb energy via inverse Bremsstrahlung. Valence electrons have an ionization potential lower than the photon energy and, since photon energy is larger than the bandgap, valence band electrons can promote to conduction band by single photon absorption [2]. The material is heated up by Joule effect, where part of kinetic energy of electrons is converted into thermal energy or heat due to the collision of the electrons with the lattice. When the material reaches the melting or vaporizing temperature, it is broken down and irreversibly damaged. This process also includes acoustic waves and optical radiation. For moderate laser intensities, the dominant ablation mechanism is the

normal vaporization, but leads to phase explosion or explosive boiling when laser intensity increases [3].

Absorption mechanisms are totally different in the case of dielectric materials. For dielectrics, ionization energy is higher than photon energy and electrons cannot directly promote from valence to conduction band. In this case, the transparent surface must be first transformed into an absorbent plasma by the laser irradiation. Then, the plasma absorbs the laser energy causing heating and irreversible damage of the material. Therefore, absorption mechanism strongly depends on few conduction or free electrons presented in the materials that act as seed electrons and initiates the process. These electrons can come from metallic impurities of the material, inclusions or thermal ionization. They absorb energy via inverse Bremsstrahlung and are accelerated in the conduction band. When kinetic energy of a free electron exceeds the ionization potential and it collides with a bound electron, the free electron transfers nearly all their kinetic energy to a bound electron in the valence band, resulting in two free electrons with low kinetic energy in the conduction band. This process is called impact ionization (Figure 3.1) and its repetition leads to the avalanche ionization process, responsible of dielectric light absorption [1, 4]. In this way, the number of free electrons in the conduction band increases exponentially and when this density reaches a critical value, the transparent material is laser-induced broken down. That means that the substrate becomes absorbent and there is a temporal and spatial variation of optical properties from a fully transparent substance to a metal-like state. Electrons transfer energy to the lattice and the material is heated up leading to the ejection of material. In the case of damage threshold in transparent materials, where there exists a need of seed electrons, the ablation process takes a statistical nature due to the fact that laser-induced optical breakdown threshold is determined by the probability of seed electrons in the material [5].

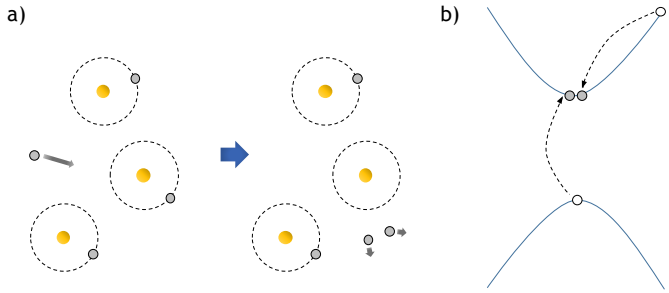

Figure 3.1: a) Scheme and b) band diagram of impact ionization process. Electrons are in grey and holes in white [1, 6].

Processes of laser matter interaction following intense ultrashort laser pulses are more complex than in the long pulse case, particularly for wide bandgap dielectrics since more absorption mechanisms are involved. This is the framework corresponding to ultrashort laser pulses ($\tau_p << \tau_r$), in this case, the interaction with opaque and transparent materials to the wavelength proceeds in a similar non-linear way, contrary to what happens with long pulses, where ablation of metals occur at relatively low intensities in a linear process opposite to transparent materials with low absorbance. Opaque materials in ultrashort temporal regime are almost ionized at the beginning of the laser pulse arrival. Conduction band electrons are already presented and the laser energy is absorbed by the free electrons via inverse Bremsstrahlung mechanism [7-9]. It has been shown that due to the extreme intensities of ultrashort laser pulses, absorption is increased by nonlinear processes [10, 11], leading to a nonlinear dependency of laser ablation with the laser pulse, unlike the nanosecond situation [12]. Moreover, it was reported that as pulse width decreases, ablation enters in a regime where threshold energy does not depend on pulse duration [13]. One of the most employed models in literature for describing the ablation behaviour of ultrashort pulses over metals is the "two temperature" model [14-16].

In the case of transparent materials to the wavelength of the employed laser the main difference with metals is that, initially, there are not free carriers in the material and energy is first employed for

their creation. Electrons are in valence band and they have to promote to conduction band considering that, as it was previously mentioned, bandgap is larger than photon energy. There are several absorption mechanisms for this purpose. One of these mechanisms is multiphoton absorption. In this process, bound electrons can promote from valence to conduction band absorbing simultaneously more than one photon during the laser pulse interaction, being the total energy of them larger than the bandgap one. This multiphoton absorption process has two roles: first, when the laser field is strong and the frequency is high it acts as main ablation mechanism and second, it serves as source of free electron for further free carrier absorption and avalanche ionization processes [17]. At high laser intensities and low frequencies, the predominant absorption effect is tunnel ionization, rather than multiphoton absorption. In tunnel ionization, the potential barrier formed by valence and conduction bands is drastically deformed by the electric field and the barrier length is reduced. In this way, electrons can tunnel through the barrier and promote to conduction band [18]. Keldysh was the first that presented a theory of photoionization in dielectrics under strong electromagnetic field in 1965 [19]. He defined the called Keldysh parameter that determines the probabilities of tunnel ionization and multiphoton process in a material, depending on the laser intensity and frequency. Also, at high intensities, already excited electron from tunnelling or photoionization can sequentially absorb several photons from the same laser pulse and be excited in a higher energy state. This free carrier absorption is called electron heating and results in no-thermal bond breaking [20]. When energy of an electron in an excited state exceeds the conduction band minimum by more than the bangdap energy, it can ionize other electron from the valence band, resulting in two excited electrons in the minimum energy of the conduction band by impact ionization [21]. This process can repeat itself as long as the intense laser field is presented, leading to avalanche ionization. Moreover, the possibility of Coulomb explosion mechanism of ablation is presented in femtosecond transparent materials that are transparent to irradiation. This consists in positive charging of the surface and, consequently, in the disintegration of the surface when the repulsion strength of ions

exceeds the lattice binding force [22, 23]. Unlike long pulse ablation, ultrashort processes do not exhibit the statistical fluctuation that nanosecond ablation does, being a more deterministic phenomenon. Some of the absorption mechanisms for transparent materials under femtosecond irradiation are illustrated in Figure 3.2.

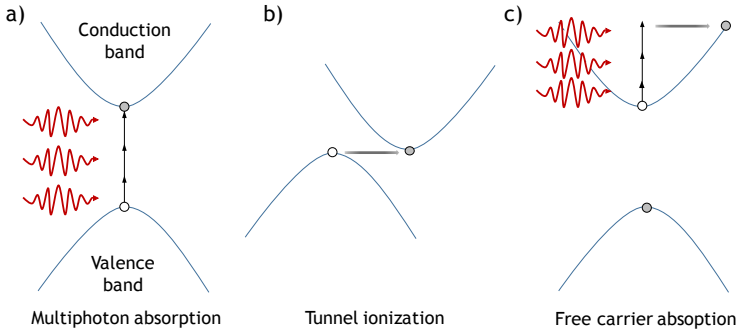

Figure 3.2: Bands diagrams of a) multiphoton absorption, b) tunnel ionization and c) free carrier absorption. Electrons are in grey and holes in white [6].

The way energy is transferred through the material once it is absorbed also depends on the pulse width, since its duration is usually different from relaxation time electron photon. After several picoseconds, laser excited electrons transfer their energy to the lattice. In the case of nanosecond pulses, where $\tau_p >> \tau_r$, the energy is transferred to the lattice in form of heat and there is enough time for the thermal wave to propagate in the substrate. First, laser energy first heats the target until the melting point and then, to the vaporization temperature. Since evaporation occurs from liquid to vapour, the final structure is characterised by more irregular edges, derived from the thermal ablation, debris, collateral damage and a significant heat affected zone [24]. On the contrary, for ultrashort pulses where $\tau_p << \tau_r$, the electron-lattice coupling can be neglected. After laser irradiation, electrons rapidly cool down. Due to the short time scales involved in this process, the material transition is considered a direct solid-vapour step. This process is a pure electron driven ablation, resulting in a negligible heat affected zone and a very precise material structuring, with no debris or thermal effects. The comparison between long and

ultrashort pulses is depicted in Figure 3.3. For the picosecond situation, where $\tau_p \approx \tau_r$, ablation is accompanied by the formation of a melted zone in the material and electronic heat conduction. It is possible that it happens a direct transition solid-vapour in the surface, but the presence of a liquid phase inside the material can reduces the quality of the ablation [25].

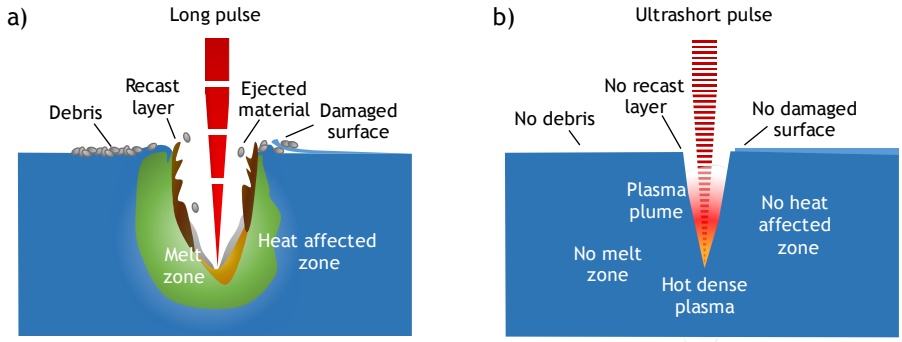

Figure 3.3: Scheme of laser ablation with a) long and b) ultrashort pulses [26].

Nevertheless, and despite all of the application of lasers, the fundamental mechanisms of laser-matter interaction are still under discussion, finding different opinions among authors and disagreements between theoretical predictions with experimental results. Further studies in the topic are required to reach a better understanding of the physical phenomena involved.

3.1.1. Laser-induced plasma-assisted ablation

Besides direct laser ablation, there is also the possibility of structure materials by indirect ablation. This method is known as laser-induced plasma-assisted ablation (LIPAA) and, contrary to direct laser writing techniques, allows fabricating big dimensional structures and is a suitable procedure when required dimensions are larger than a few micrometres, as it will be presented in Section 3.3. It was first reported in literature in 1998 by Mirodikawa group in Japan [27]. Essentially, this technique is based on the employment of a laser wavelength that is transparent to the substrate to ablate, like infrared

for glass. A metal foil, which is opaque to the laser energy, is placed below the substrate. Moreover, the fluence employed should be below the glass threshold but above from the metal one. In this way, the beam passes through the substrate and is absorbed by the metal. Laser-induced plasma is generated over the metal and, due to interaction between the plasma and the laser beam, ablation occurs at the rear side of the glass [28]. Irradiation without metal foil does not lead to ablation and also, if laser irradiation is not perpendicular to the sample there will not be interaction of the plasma with the beam and hence no structuring of the material [29]. The plasma is composed by ions, clusters and large particles that change the target surface when they reach it, creating absorbing sites for the laser beam, resulting in ablation [30]. Nevertheless, mechanisms involved in this plasma-beam interaction are still not clear. It has been demonstrated that distance between metal and substrate affects to the quality of the ablation. Intuitively, if they are too distant, the influence of plasma is very weak and does not ablate the target, but some metal species can be found over it. On the contrary, when in contact, the ablation rate is higher [31]. If a thinner ablation mark is desired, few microns are the suitable distance to have between the materials [32]. This LIPAA process has always been reported with nanosecond lasers, since laser induced plasma is generated a hundred picoseconds after the irradiation. When using femtosecond pulse durations, two different pulses are needed for LIPAA. One to initiate the process that does not generate ablation and other with a certain delay respect to the first one, to interact with the plasma and remove material [33]. Figure 3.4. shows a scheme of laser-induced plasma-assisted ablation.

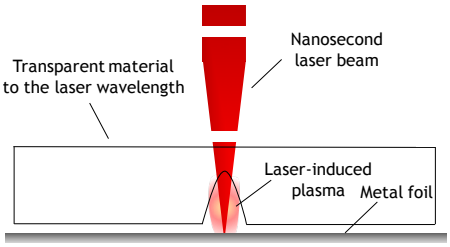

Figure 3.4: Schematic representation of laser-induced plasma-assisted ablation [34].

3.2. FABRICATION OF MICROCHANNELS BY DIRECT LASER ABLATION IN SODA-LIME GLASS WITH DIFFERENT PULSE DURATIONS

Microfluidics has emerged in the past years as a field that aroused huge interest in research due to the applications it presents. From chemistry analysis to biomedical assays, microfluidics has revolutionized scientific research by approaching problem in a smaller scale. It consists in the miniaturization of devices to the micrometric scale for the manipulation of very small volumes of fluids. These chips can be very complex, with several layers and structures inside, but one of the basic units of these devices is the channel. In this section, microchannels over soda-lime glass are fabricated by laser direct ablation. Glass, as it was introduced in the previous chapter, is presented as a very suitable material for this purpose due to its robustness, resistance and transparency. The structures are manufactured by direct laser ablation in the infrared spectral range with different pulse durations. From nano to femtosecond ranges, the obtained structures are analysed and studied. Their roughness value can be modified by different thermal treatments regarding the final application of the channel.

3.2.1. Microchannel fabrication with nano, pico and femtosecond pulse durations

For the fabrication of the microchannels with different pulse durations, three different laser systems are employed. In particular, the Rofin PowerLine E (Nd:YVO_4) nanosecond laser, the Coherent Lumera Super Rapid HE (Nd:YVO_4) picosecond one and the Spectra Physics Spitfire (Ti:Sapphire) in the femtosecond regime. Specifications of each system can be found in Chapter 2 but briefly, both Nd:YVO_4 lasers have a central wavelength of 1064 nm and pulse durations of 20 ns in the case of the Rofin setup and 12 ps for the Coherent system. The femtosecond laser has a wavelength of 800 nm and 100 fs pulse duration. In Figure 3.5, schemes of the laser setups are depicted.

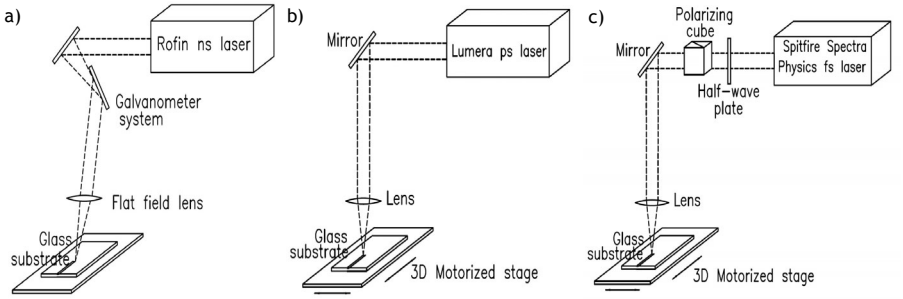

Figure 3.5: Schemes of the setups employed for the fabrication of the channels by laser direct writing. a) Nanosecond, b) picosecond and c) femtosecond systems.

For determining the optimal laser parameters that ensure a homogenous ablation of a microchannel over soda-lime, a previous study of the processing setting is carried out with each laser system. It is found that the optimal laser parameters for working with soda-lime glass are: for the nanosecond laser 700 μJ pulse energy, 10 kHz repetition rate and 50 mm/s scan speed, with a pulse overlapping of 73%. For the picosecond pulse duration regime, laser parameters are found to be 80 μJ pulse energy, 10 kHz repetition rate and 20 mm/s scan speed, resulting into a pulse overlapping of 96%. Finally, when working in the femtosecond regime, 40 μJ pulse energy, 1 kHz repetition rate and 0.6 mm/s scan speed are employed. The overlapping defines the shared area of one laser pulse with the subsequent one and in this case, it takes a value of 97%

Threshold mean fluences are experimentally measured in the three scanning cases. It was defined as the minimum fluence value that generates ablation in the material with no overlapped pulses. For the nanosecond case, it was 138 J/cm^2, 49 J/cm^2 for the picosecond regime and 5 J/cm^2 for the femtosecond laser. Energy per pulse to carry out the microchannels is chosen in all cases to be the double of the threshold energy in order to ensure a homogenous ablation process along the channels but avoiding an energy excess that may be detrimental for the quality of the ablated channels. As it was expected, the fluence needed for material removal decreases as the pulse duration becomes shorter [35-37]. Scanning speed and repetition rate

are chosen in order to obtain the suitable overlapping of the pulses for generating a quality channel. The evolution of the channel dimensions with the number of laser scans is studied and results are shown in the graphics of Figure 3.6. As expected, depth and diameter of the structures increase with the number of laser scans. Measurements are acquired with Sensofar S Neox confocal microscope and Nikon MM-400 metallurgic microscope when the depth of the channel was too large for confocal inspections.

As it is presented in the graphics of Figure 3.6, the evolution of the depth and diameter of the channels is different depending on the temporal regime employed. In the case of nanosecond pulse duration (Figure 3.6.a), channels with a depth around 1.5 μm are fabricated with one laser scan and a plateau of around 8.8 μm is reached at the sixth laser scan. The diameter of the microchannel increases with the scans from 19 to 28 μm, from one to ten laser scans, respectively. For channels obtained with picosecond pulse duration (Figure 3.6.b), the depth achieved with one laser scan is around 8 μm and increases gradually with each laser scan until 60 μm in the tenth scan. In this case, no plateau is achieved. The diameter of the microchannel starts with a value around 20 μm until a plateau of 24 μm in the sixth scan. Finally, in the femtosecond regime (Figure 3.6.c), with the first laser scan a channel with depth of 10 μm is obtained that increases up to 35 μm in the tenth laser scan. Diameters go from 21 μm to 27 μm, accordingly.

For comparison, fabrication parameters that result into channels with an aspect ratio 2:1 diameter depth are chosen for the three laser systems. For this purpose, six laser scans are stablished as the optimal number when working in the nanosecond regime, obtaining a channel of 8.7±0.1 μm depth and 23.9±0.6 μm diameter. For the picosecond pulse duration laser, only one laser scan is needed for obtaining a depth of 8.4±0.2 μm and 17.8±0.2 μm of diameter, as well as in the femtosecond regime, where a channel with 10.1±0.6 μm depth and 20.7±1.4 μm diameter is ablated. In each case, three channels are manufactured and characterised in order to calculate the measurement

errors (standard deviation). SEM and 3D confocal images of the microchannels fabricated with the three different laser systems are shown in Figure 3.7.

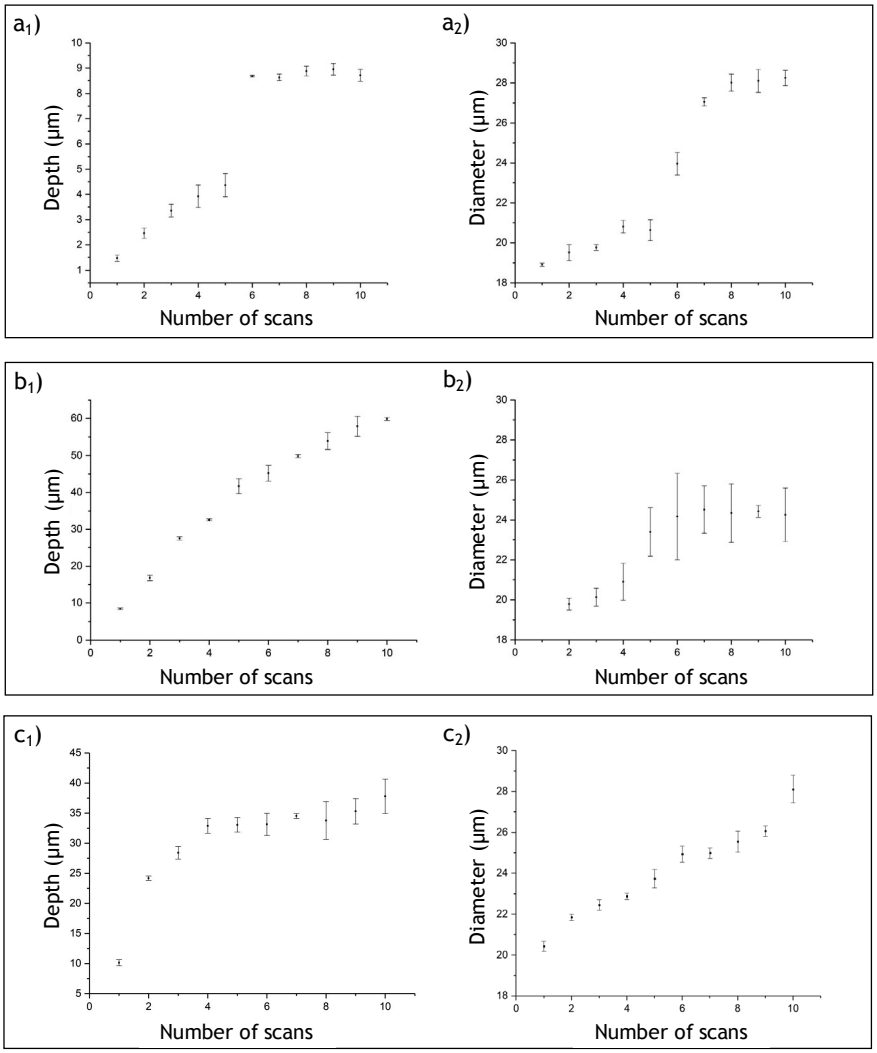

Figure 3.6: Evolution of the depth (subscript 1) and diameter (subscript 2) of the microchannels fabricated when using a) the nanosecond b) the picosecond and c) the femtosecond temporal regimes.

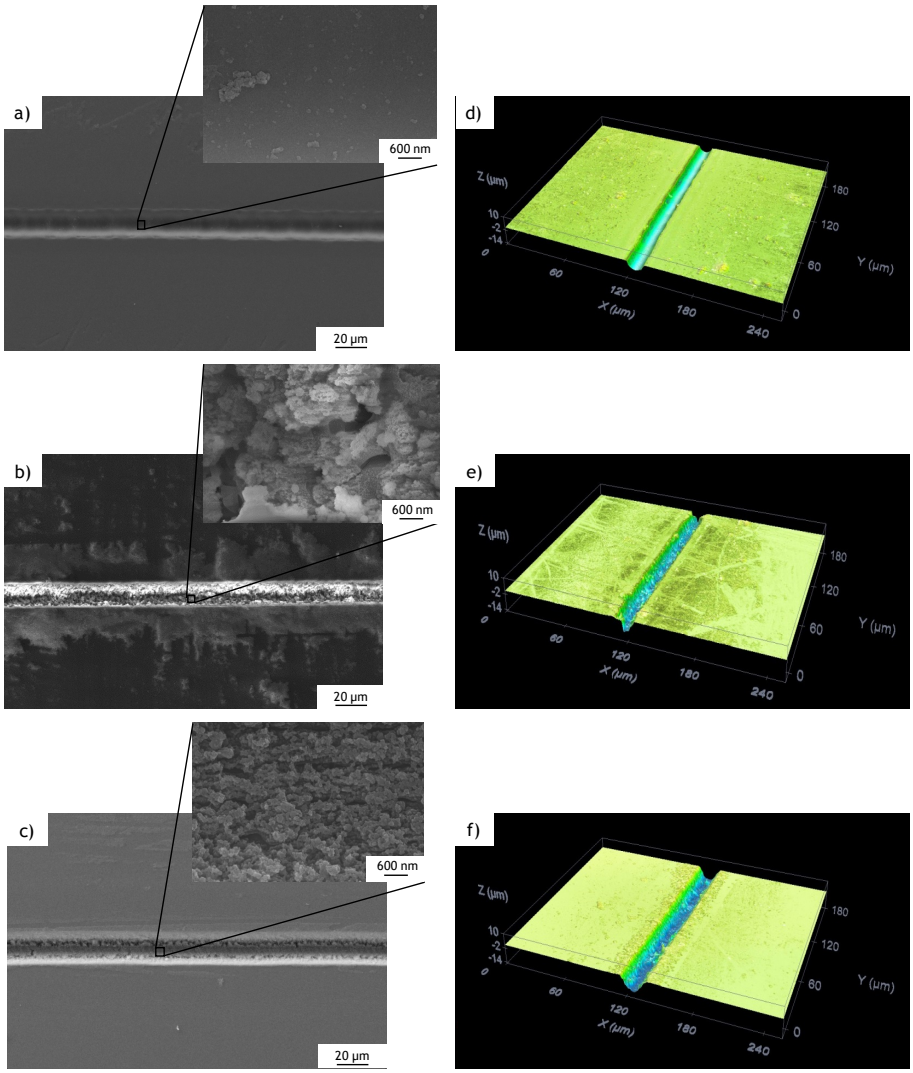

Figure 3.7: SEM and 3D confocal images of the microchannels fabricated with: a) and d) nanosecond, b) and e) picosecond and c) and f) femtosecond lasers. Enlarged views of the bottom of each channel are shown at the top of the first column.

In Figure 3.7 it can be seen that the microchannels fabricated with the different laser systems have similar dimensions and aspect ratio. It should be noticed that surface roughness of the structures is very different due to the nature of ablation process in the three temporal regimes. As it was previously explained in this chapter, for long pulses, the material is expelled by heat deposition; it is melted and then vaporized. In the ultra-short pulse regime, removal is more explosive, resulting into a direct vaporization of the material with minimal heat affection and melting. The process is then more disruptive and leads to a structure with a high roughness value but with sharp and well-defined borders, in contrast with the smooth surface of the nanosecond channel. In the picosecond situation, a combination of both effects occurs, resulting in a process where part of the material is directly vaporized but also have a significant transference of heat to the lattice and, therefore, melted material may appear [38]. Arithmetical mean roughness of the surface (S_a) is measured according to ISO 25178. Values for the channels fabricated with the nanosecond pulse duration are 178.7±15.6 nm, 1028.3±198.4 nm for the picosecond and 1016.3±123.8 nm for the femtosecond situation. As it was expected, the surface roughness value of the picosecond and femtosecond channels is higher than the ones manufactured with nanosecond pulse duration.

3.2.2. Role of impurities in laser ablation

As it was explained in Chapter 2, the chemical composition of both surfaces of soda-lime glass is different. In one of the sides there is a presence of tin impurities derived from the fabrication process of glass that it is not in the other face of the substrate. These dopants play a key in the microstructuring of the material with laser. All microchannels shown in Figure 3.7 have been manufactured by writing over the doped side. Comparison of the results when working over the doped and undoped surfaces, with the same laser parameters as previously, is shown in Figure 3.8.

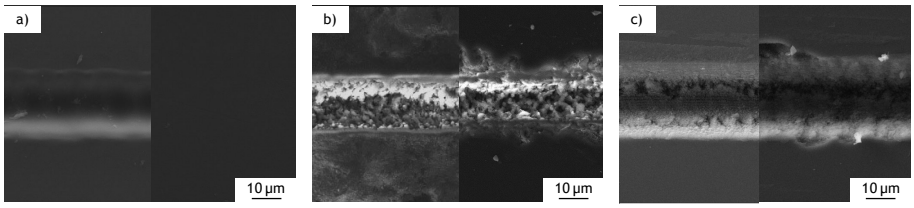

Figure 3.8: SEM images of the structures obtained on both surfaces of soda-lime glass when irradiating with the a) nanosecond, b) picosecond and c) femtosecond lasers. In each sub picture, left-side corresponds to the doped surface and right-side to the undoped surface.

In Figure 3.8.a it can be seen that in the nanosecond regime impurities are essential for performing ablation. While working over the face with tin, a quality microchannel is obtained but when irradiating the undoped surface with the same parameters, no material is removed. This is due to the tin dopants critical role to initiate the ionization of the material, providing seed electrons that will lead to impact ionization and subsequent avalanche ionization [39-41]. If there was no presence of them, ablation will not occur since there will be no presence of free electrons in the material. In picosecond and femtosecond regimes, Figures 3.8.b and 3.8.c respectively, ablation happens in both sides of the glass independently of the presence of dopants. This occurs due to the physical mechanisms of absorption in those temporal regimes, where no seed electrons are needed to start the process in transparent materials. Nevertheless, there are important differences in the morphological quality of the generated structures depending on the side to be ablated. Whereas in the doped side of the glass the channel shows straight and sharp edges (left-side images in Figure 3.8), in the undoped one the structure presents several cracks and edge chipping (right-side images in Figure 3.8). The formation of such defects in the micromachining of glasses with ultrashort pulses appears frequently and it is related to the low thermal diffusivity of these materials. When the heat deposited in the focal volume by the laser pulse has not enough time to be diffused in the material during processing, very high temperature gradients are created that may lead to the formation of mechanical fractures and cracks. The processing parameters (pulse energy, repetition rate, beam size at focus and

number of scans) can be then optimized in order to prevent such defects to appear [42]. In our case, the irradiation conditions are chosen in order to get direct morphological comparison of the channels produced with the three laser systems, but no initial care was taken in order to avoid the presence of cracks at the edges. Therefore, results observed in the undoped side of the sample are not surprising. In order to elucidate the role of the dopant in the excellent quality of the microchannels in the other side of the sample, we determined the threshold fluence and channel dimensions in both sides, obtaining exactly the same values as reported. It means that the presence of dopants has significant effect neither in the generation of the free-electron plasma during the pulse irradiation nor in the critical density for producing ultrafast ablation. Then, the role of the Sn dopants in the morphology of the channels is expected to be closely linked with an increase in the thermal diffusion of the irradiated volume of the glass, thus reducing the high temperature gradients created during the irradiation, and consequently minimizing the mechanical stresses that lead to the formation of cracks and edge chipping. In general, it was found that tin impurities, presented in one side of the glass and derived from the fabrication process of the material, play a key role in the ablation process and are crucial for the manufacturing of good quality microchannels, regardless the pulse duration employed.

3.2.3. Post-thermal treatment

Once microchannels are fabricated with the three laser systems and characterised, thermal treatments are applied to them in order to modify their topography and to reduce their roughness. As it was introduced in Chapter 1, microfluidic is relevant in different fields. Depending on the particular application microchannels are created for, a particular roughness value in the bottom of the channel can be more suitable than other. For example, for performing bioassays where cell attachment is needed it was demonstrated that high roughness structures promotes cell adhesion [43]. On the other hand, if experiments only involve fluid manipulation, channels with low roughness are desirable to facilitate optical inspections and to avoid

the alteration of the fluid dynamics. Moreover, the interaction of the fluids with light from embedded optical waveguides in optofluidic chips and lab-on-a-chip devices [6] requires excellent quality and flatness of the channel walls. With the treatment described in this subsection, roughness can be modified in a controlled way according to the final value needed for each particular application. These treatments are applied by using a Nannetti static furnace working at five different temperatures. Taking into account that the transition temperature for soda-lime glass is 570 °C, the range of applied temperatures goes from 590 °C to 630 °C in steps of 10 °C, ensuring to achieve significant changes in the samples between each gap. Each sample is heated for two hours with a pre-heating of 30 minutes until reaching the treatment temperature. As temperature rises, material melts and redistributes into the channel. Figure 3.9. shows the variation of the channel profile with the thermal treatments in each situation. Table 3.1 records the surface roughness value variation of the microchannels with the temperature.

Roughness (nm)	Nanosecond	Picosecond	Femtosecond
No treatment	178.7±15.6	1028.3±198.4	1016.3±123.8
590 °C	136.1±5.9	349.4±35.1	184.1±29.7
600 °C	148.9±1.4	232.6±13.8	143.2±13.7
610 °C	140.3±1.4	217.2±27.4	143.2±13.7
620 °C	94.2±24.2	117.9±4.5	56.7±17.5
630 °C	12.1±1.7	43.2±1.6	12.9±8.1

Table 3.1. Variation of the arithmetical mean roughness of the surface according to ISO 25178 for the microchannels manufactured with the different laser systems when thermal treatments are applied.

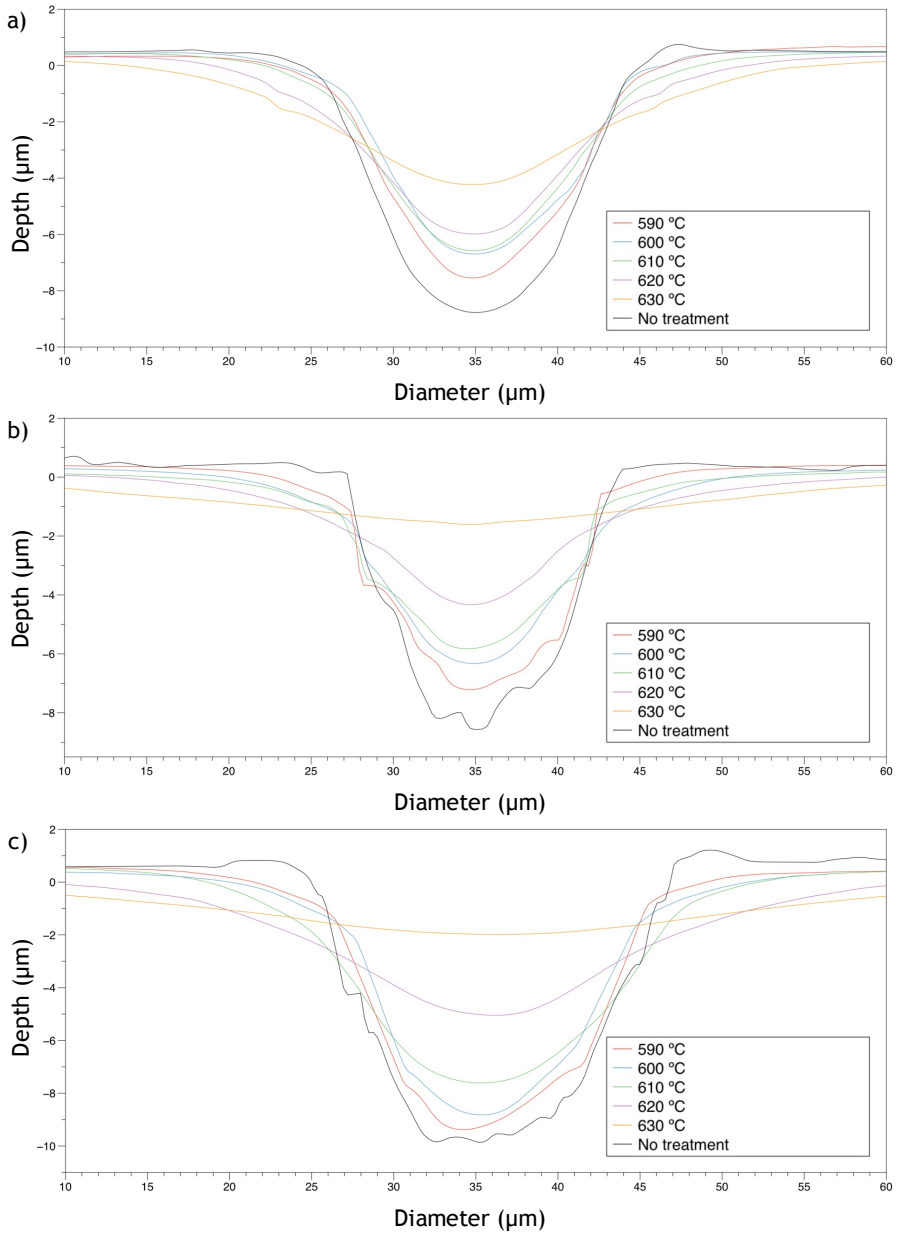

Figure 3.9: Evolution of the profile of the microchannels manufactured with the a) nanosecond b) picosecond and c) femtosecond laser systems with temperature.

In Figure 3.9, it can be seen how above the transition temperature of soda-lime glass channels melt and become shallower structures with lower roughness value. Moreover, they become wider as the temperature increases. When working at 590 °C, all channels approximately maintain the same aspect ratio as the non-treated ones. Nevertheless, for this temperature the structures generated with the picosecond and femtosecond lasers experience a significant reduction of the surface roughness. As it was expected, as temperature increases, the depth of the channels decreases and the aspect ratio is modified, reaching a complete loss of their initial shape at 630 °C. In that case, surface roughness takes a similar value to non-processed glass.

Ultimately, we may stress that by applying a thermal treatment at a selected temperature the roughness and shape of the microchannels can be modified in a controlled manner.

3.3. FABRICATION OF CORONARY LIKE PRECLINICAL DEVICES BY INDIRECT LASER ABLATION

Despite microfluidic research is getting a lot of attention, there is also the need to manufacture structures with larger dimensions. For example, organ-on-a-chip field, which mimics the functioning of parts of the body, requires of devices that are in the same dimension order as organ components, which are sometimes far from the micron size. In this section, the fabrication of preclinical devices that imitate coronary bifurcations with millimetre dimensions by laser technology is presented. In recent years, there has been a huge and increasing interest in this kind of chips for studying cardiovascular diseases in vitro conditions since these pathologies are some of the principal causes of morbidity worldwide [44, 45]. By fabricating a functionalized blood vessel-like model, flow experiments can be performed in laboratory under controlled conditions in order to observe changes in endothelial cells [46-48]. As investigation in pharmacology and detection techniques are crucial to treat these illnesses and minimise their consequences, in vitro studies are also very important for a better understanding of the sickness dynamic and

are directly linked with early detection and diagnosis. For example, in this thesis, as it will be explained in next chapter, one of the fabricated devices is employed to determine low velocity zones in coronary bifurcations where normal blood flux is altered. In these areas, endothelial cells are more prone to be injured, leading to higher risk of arteriosclerosis lesions [49, 50]. These conflictive zones depend on the bifurcation geometry and, by means of in vitro studies of these configurations, critical coronary angles can be identified. This knowledge is undoubtedly valuable for clinical specialist and it is not limited to this subject. Future research lines with these devices are focused on the impact of these low velocity zones and the deposition of circulating tumour cells in the blood stream. The aim is to identify geometries more susceptible to tumour cell deposition and subsequent extravasation, resulting in metastases [51-54]. These devices could also be employed in the future in the development of new drugs, evaluating their effectiveness in simulated environments [55].

Different channel geometries to perform bioassays have been described, most of them in the micron order, to simulate a blood capillary [56-58] but the study of larger structures that imitate bigger vessels is also relevant. Laser techniques, in particular laser-induced plasma-assisted ablation, allow obtaining a millimetre depth structure with high precision that mimics large blood vessels. The master is manufactured on a soda-lime glass using a Q-switch laser working in the nanosecond regime, temporal range more implemented in industry that the femtosecond one. In this study, we focus on coronary bifurcations, but laser technologies would enable us to create channels with very different structures, like arteries with atheroma plaques or even to design personalised blood vessel with any particular geometry obtained from a patient by image procedures.

The initial roughness of the glass structure, derived from the laser fabrication process, can be modified in a controlled manner by applying a thermal treatment to the substrate. Although in this chapter only fabrication methods are presented, as the final objective of this device is to mimic blood vessels, the device should be totally

functionalized with endothelial cells that attach and grow on their walls. It has been demonstrated that physical aspects like elasticity, topography or roughness of the substrate play and important role in the growing and spreading process of the cell [43], depending on the kind of material and type of cell. In our case, this initial roughness is exploited as an easy and low-cost way to enhance cell adhesion to the walls and it is modified in a controlled way to obtain different masters of devices with different roughness characteristics. While fabrication results are presented in this subsection, the cellular functionalization of the device is shown in the next chapter. Two different thermal treatments are performed. First, laser-assisted treatment with a CO_2 laser combined with a roller furnace is carried out. After considering that this is not the most suitable method for these channels, a thermal treatment with a static furnace is applied.

Since biological validation is the final aim of these devices, they are replicated in a more suitable material for this purpose: PDMS. By soft-lithography methods the master structures fabricated in soda-lime glass are obtained in a material that allows long term cell cultures. Particular properties of PDMS can be found in Chapter 2. This replication procedure is carried out in two different ways in terms of sealing but final device results the same in both situations. Moreover, since half channel structure is obtained in the master fabrication, in this step the possibility to fabricate a whole channel device is presented by sealing two halves. Hence, circular or semi-circular coronary like devices can be fabricated with different wall roughness depending on the final application.

3.3.1. Fabrication of the master by laser-induced plasma-assisted ablation in soda-lime glass

Indirect laser writing technique LIPAA is employed to manufacture big dimension channels over soda-lime glass substrate. AutoCAD software is employed for the design of the structure. The designed CAD structure has a Y shape with semi-circular profile and modifiable angle between the branches of the bifurcation. Dimensions

are 2 mm width and 1 mm depth, in order to fabricate devices with half blood vessel geometry or entire channels by sealing two symmetric halves. For this purpose, the Rofin PowerLine E laser system is employed. The system has a commercial software able to read CAD files, transferring the design to movement of the galvanometric mirrors of the equipment. Detailed specifications of this setup can be found in Chapter 2 but succinctly, is has 1064 nm central wavelength and 20 ns pulse duration. Soda-lime glass is a very suitable material for the fabrication of the master due to its hardness and resistance, among other properties already mentioned in the introduction of this thesis. This material is non-absorbent in the infrared, spectral range where the laser operates, so a variation of conventional direct laser writing techniques is employed in order to create millimetre structures over this substrate. This procedure is laser-induced plasma-assisted ablation and has been explained in previous sections in this chapter. Briefly, it consists in focusing the laser beam over a metal target that it is placed below the glass substrate. Laser generates a plasma when reaching the metal and its interaction with the laser beam leads to ablation of the rear side of the glass substrate. Once superficial roughness has been induced in the target, the material becomes absorbent and the metal foil is no longer needed [27]. In order to remove more than 1 mm of material, desired depth for fabricating coronaries like models, several laser passes have to be applied to the substrate. During this process, the laser beam must be refocused on the channel bottom surface to continue the ablation.

As a first step for the fabrication process, a study of proper laser parameters should be carried out. In particular, this laser setup allows controlling average power, repetition rate and beam velocity. Also, the distance between subsequent laser scans when filling the design is an important parameter to control in order to obtain a good quality channel. Intensity provided to diode pumps, related with laser average power, is fixed at its maximum at 33 A (it corresponds to 8 W average power at 12 kHz repetition rate, with an energy per pulse of 666.6 μJ). Thus, ablation is ensured in all the process. For setting the working parameters, only one scan to the Y structure is applied, looking for a

homogeneous ablation from the beginning of the process and not due to accumulative process in subsequent laser scans. First, optimal repetition rate is searched. In this case, velocity is fixed at 1000 mm/s and distance between laser passes is 25 μm. Figure 3.10 shows images acquired with metallurgic microscope Nikon MM-400 of channel surfaces with different repetition rates, from 1 to 48 kHz. As it was expected, when repetition rate increases, more overlapping is observed in the glass surface. In the case of 1 kHz frequency (Figure 3.10.a), repetition rate is too low to fill the designed channel. On the contrary, 48 kHz (Figure 3.10.f) is an excessively high frequency so energy per pulse it is not enough to properly structure the rear side of the material and only a damaged structure with signs of metallization is observed. The repetition rate of 12 kHz (Figure 3.10.d) seems like the proper value that generates a homogeneous overlapping, since in the case of 6 kHz (Figure 3.10.c) single marks of laser-induced plasma can be still distinguished and 24 kHz (Figure 3.10.e) presents an excessive overlapping.

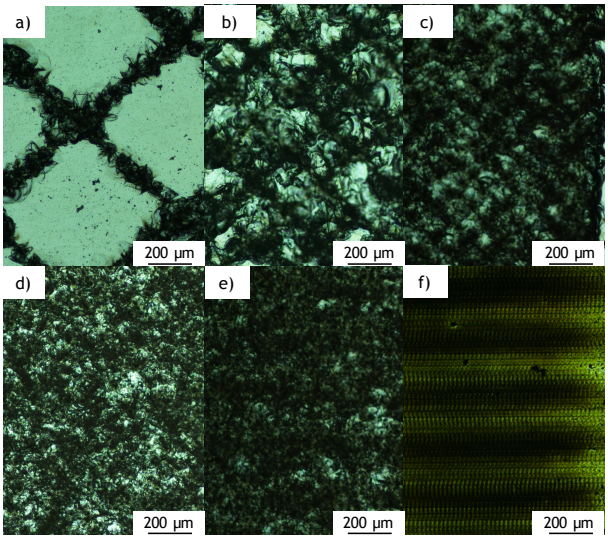

Figure 3.10: Metallurgic microscope images of channels fabricated by LIPAA over soda-lime glass with repetition rates of a) 1 kHz, b) 3 kHz, c) 6 kHz, d) 12 kHz, e) 24 kHz and f) 48 kHz. Velocity is 1000 mm/s and distance between consecutive laser scans is 25 μm.

As second step, other parameter to study is the velocity of the beam. For this purpose, velocities from 50 to 5000 mm/s are evaluated. Repetition rate is fixed at 12 kHz and distance between laser scans is 25 μm. In Figure 3.11 it can be seen that as velocity increases, overlapping decreases, leading to an inhomogeneous material removal. For velocities from 50 to 100 mm/s (Figures 3.11.a and 3.11.b, respectively), overlapping is excessive. Velocity of 500 mm/s (Figure 3.11.c) provides a suitable surface but this value can be optimised. For velocities above 2000 mm/s (Figures 3.11.e and 3.33.f), the beam moves too fast, leading to a structuring where single impacts can be appreciated. In conclusion, 1000 mm/s is the highest velocity that provides a homogeneous structure, thus is the one that optimises the process and makes it faster. Of course, there could be other combination of repetition rate and speed parameters that results into to an appropriate overlapping, but this frequency leads to the proper energy per pulse that allows ablation.

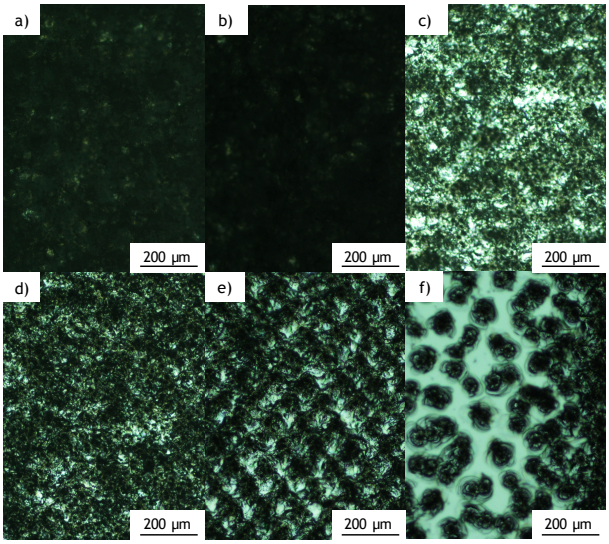

Figure 3.11: Metallurgic microscope images of channels fabricated by LIPAA over soda-lime glass with velocity values of a) 50 mm/s, b) 100 mm/s, c) 500 mm/s, d) 1000 mm/s, e) 2000 mm/s and f) 5000 mm/s. Repetition rate is 12 kHz and distance between consecutive laser scans is 25 μm.

Finally, the influence of the distance between consecutive laser scans in ablation is analysed. Structures with 12 kHz repetition rate and 1000 mm/s velocity are manufactured with spacing from 6 to 200 µm. Figure 3.12 shows the importance that this parameter plays, crucial for a proper filling of the design. For spacing above 50 µm (Figures 3.12.d to 3.12.f), the surface is not homogeneously ablated. A proper superposition of lines is obtained when the distance is 50 µm (Figure 3.12.c). It is not optimal to work below this value (Figures 3.12.a and 3.12.b) since it will take more time to manufacture the sample and will result in a unnecessary overlapping of lines.

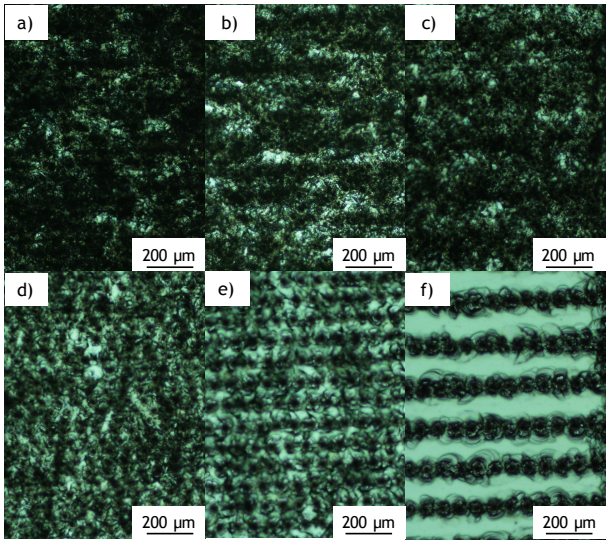

Figure 3.12: Metallurgic microscope images of channels fabricated by LIPAA over soda-lime glass with distance between consecutive laser scans of a) 6 µm, b) 12 µm, c) 25 µm, d) 50 µm, e) 100 µm and f) 200 µm. Repetition rate is 12 kHz and beam velocity 1000 mm/s.

After this study, the optimal laser parameters for fabricating the millimetre channels are: repetition rate of 12 kHz and average power of 8 W corresponding with an energy per pulse of 666.6 µJ, scan speed of 1000 mm/s and distance between consecutive laser scans of 25 µm. Thirty laser scans are needed to reach the millimetre depth with a refocus of 400 µm from the metal foil to the surface of the

channel in the middle of the process. As mentioned in previous sections, ablation rate in LIPAA process is enhanced when the substrate is in contact with the metal. Nevertheless, in order to facilitate the evacuation of debris derived from ablation, the materials are separated 200 μm. In this way, glass powder can leave the generated structure, avoiding its resolidification and consequently, obtaining the proper channel profile. Figure 3.13 shows a SEM image of the bottom of the glass channel and a 3D image of the result.

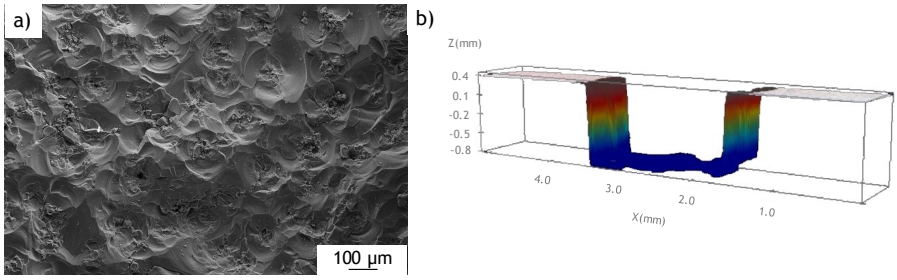

Figure 3.13: a) SEM image of the bottom of the channel and b) 3D confocal image of the obtained structure.

In Figure 3.13.b it can be seen that, by using this technique, channels with millimetre dimensions over a non-absorbent material in the infrared, like soda-lime glass, are achieved [59]. The obtained structure presents a high roughness value, due to the ablative nature of the process, as it can be appreciated in the SEM image of the bottom of the channel (Figure 3.13.a). The removal of the material is not like in the nanosecond direct ablation, where material is melted and vaporised, leading to a soften surface in the structure characterised by heat-affected zones. In this case, the structuring is more abrupt since it comes from the interaction of a laser-induced plasma and the laser beam. Material removal in this case is more similar to "impacts" in the target. Moreover, due to the nature of this LIPAA process, no significant dependency of tin dopants was found. Unlike in the direct ablation case, the different composition sides of glass are irrelevant for the structuring, obtaining same results in both faces of the target.

3.3.2. Post-thermal treatments

Due to the nature of the ablative process, the generated structures have a high roughness value. As this aspect has been demonstrated as key factor in cell adhesion to the surface, this value is modified in order to obtain different masters in soda-lime glass with different roughness values. Hence, preclinical devices with same geometry but distinct average roughness value will be later manufactured from these masters and cell adhesion over them will be evaluated.

By means of thermal treatments, material melts and redistributes inside the channel, smoothening the surface. The shape of the channel is also altered since they become shallowest due to the molten glass that is deposited on the bottom from the walls. Moreover, their profile is modified, becoming more semi-circular instead of rectangular. In this work, two different thermal treatments are carried out. First, a method that combines CO_2 laser irradiation in combination with a roller furnace is considered. Nevertheless, this treatment does not prove to be the most suitable for these millimetre channels and thermal treatments with static furnaces are applied to the samples.

3.3.2.1. CO_2 laser treatment combined with a roller furnace

The CO_2 laser, with a wavelength of 10.6 μm, pulse duration of 10 μs and maximum power of 124 W, operates in Q-switch regime with a repetition rate of 12 kHz and a scan speed of 90 cm/s. In order to avoid a thermal shock of the soda-lime glass that will lead to its break, the sample is previously heated in a roller furnace at a speed of 1000 mm/h gradually reaching a temperature of 500 ºC. This temperature is below the transition temperature of the soda-lime glass, which has a value of 570 ºC, and is enough to avoid possible cracks during the process due to thermal shocks. When the channel arrives at the central part of the roller furnace, the CO_2 laser interacts with the surface of the soda-lime glass, reaching a temperature in the top of the material above the transition one. This results in a local melting of the glass in the upper part of the sample. The material in the channel melts

and redistributes, generating a structure with lower roughness. After the thermal treatment with laser, the sample leaves the roller furnace in a cooling region. In Figure 3.14 a scheme of this setup is depicted.

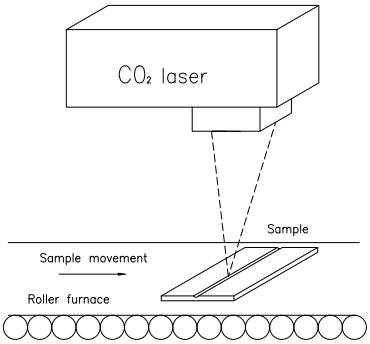

Figure 3.14: Scheme of CO_2 laser thermal treatment combined with a roller furnace.

As it can be seen in Figure 3.14, the CO_2 laser deposits its energy perpendicularly over the material and only interacts with the surface of the substrate. In order to observe significant change in the channel morphology, the process has to be repeated at least four times. By applying this technique, channels with 1.215±0.010 mm depth and 5.29±0.30 μm roughness value becomes into structures of 1,005±0.010 mm depth and 1.31±0.26 μm roughness. SEM images of the channel without and with thermal treatment are shown below in Figure 3.15.

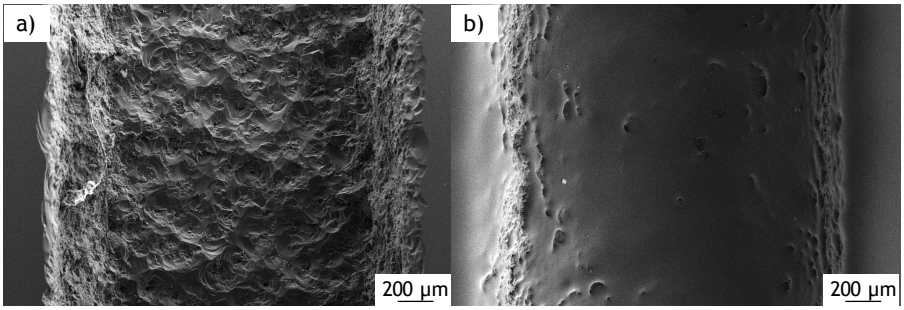

Figure 3.15: SEM images of the soda-lime glass channels a) without any thermal treatment and b) with the post-treatment with a CO_2 laser combined with a roller furnace.

It can be noticed in Figure 3.15 that the channel notably modifies its topography with this thermal treatment. Nevertheless, this process takes one hour and a half. It is not until the fourth time the process is repeated that significant changes are obtained, so the whole treatment of each soda-lime master is six hours. This method has been demonstrated to be useful in the thermal treatments of micrometric structures [60], significantly enhancing the quality of the device but it does not seem to be the more suitable for millimetre structures. Moreover, one advantage of this technique is that the glass substrate is not altered in the process. In conventional treatments, the entire substrate is heated up at a temperature above the transition one for certain time but in this situation, energy only locates on the surface of the structure for a brief period of time, when the laser deposits its energy over the surface. In the rest of the travel of the piece along the furnace, the sample is below the transition temperature. This results into the preservation of initial properties of the soda-lime glass such as transparency and flatness, which are crucial in microfluidics when this material is going to be employed as final device. Nevertheless, this is not the situation presented in this work, where the structure is employed as master for replication and certain turbidity of the glass does not prevent this purpose. In our opinion, this thermal treatment does not result optimal and there are other kind of processes that can be performed that do not require that amount of time and offers good results, as it is shown next.

3.3.2.1. Static furnace treatment

The alternative proposed method consists in a thermal treatment using a static furnace. As it was mentioned, the transition temperature of soda-lime glass material is 570 ºC and samples are heated up during 2 hours at several temperatures above the transition one: 590 ºC, 630 ºC and 670 ºC. These intervals are selected in order to see significant differences among the temperatures. In this process, as in the case of the laser irradiation treatment, material in the channel melts and redistributes from the top to the bottom, leading to a structure with a lower roughness and a different depth and profile. A channel with no thermal treatment is used as control. Figure 3.16 shows the change in the channel profile when different thermal treatments are applied. Table 3.2 records the arithmetical average profile roughness value (R_a) and depth for each one.

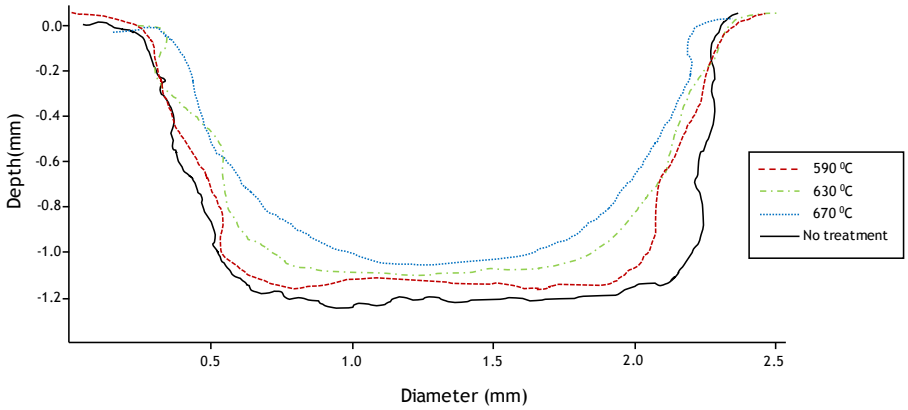

Figure 3.16: Profile of the different soda-lime glass masters after the thermal treatment at different temperatures above the transition one.

	No treatment	590 ºC	630 ºC	670 ºC
Depth (mm)	1.215±0.010	1.107±0.010	1.069±0.010	1.030±0.010
R_a (nm)	5285.01±304.56	1528.01±100.01	400.84±20.31	27.18±4.52

Table 3.2: Experimental values of the depth and arithmetical average profile roughness (R_a) of each soda-lime master after the different thermal treatments.

Figure 3.16 shows shallowest channels with more semi-circular profiles as the temperature of the thermal treatment increases. This modification of the structure helps the final device in the imitation of a blood vessel [61]. It can also be noticed that the roughness of the channel walls drastically decreases as the temperature increases. In particular, channels with roughness from microns to nanometres are obtained. In Figure 3.17, SEM images of the soda-lime channels with different thermal treatments are shown.

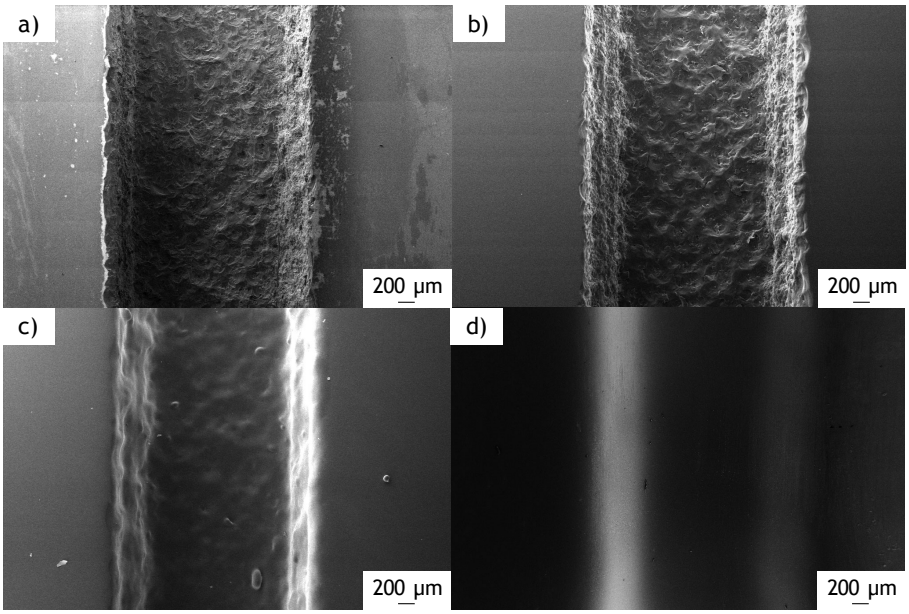

Figure 3.17: SEM images of the soda lime masters a) without and with thermal treatments at b) 590 ºC, c) 630 ºC and d) 670 ºC.

In Figure 3.17 the change in the roughness value as temperature of the treatment increases can be visually appreciated. It can be noticed how material melts and surface becomes smoother, reaching the limit situation at 670 ºC (Figure 3.17) where roughness is similar to non-processed glass and SEM technologies have difficulties to obtain the image.

3.3.3. Replication in PDMS by soft-lithography methods

Once the masters with different roughness are fabricated, they are replicated to obtain the final device in PDMS. Basics of soft-lithography method were explained in Chapter 1. Nevertheless, there are variations of this procedure for bonding purposes. Since these devices have to be closed, conversely some microfluidic devices that act by capillary, chip sealing is a key factor for the success of the experiments. Moreover, most of conventional sealing techniques, like the ones that include thermal treatments or glues, are not suitable when employing PDMS since they are ineffective or even toxic for the future cell culture in the device. There are numerous factors that determine the quality of the bonding, such as the cleanliness of the surfaces, the ratio of the PDMS parts or the time and temperature of the curing process. Also, the selected bonding technique depends on the final application of the devices and the flux pressure that they will support [62].

There are several techniques for PDMS-PDMS bonding. One relies on the inherit adherence of cured PDMS to surfaces. When two PDMS layers are put in contact, they form a reversible sealing [63]. Nevertheless, this method does not resist high pressure flux experiments without leaking. Other technique very employed in microfluidics is oxygen plasma exposure, which oxidizes the surface and activates PDMS [64]. By this method, silanol groups (OH) are created in the surface of PDMS and when two layers are brought together, they form a covalent siloxane irreversible bond (Si-O-Si), losing a molecule of water [65]. This procedure also makes surfaces hydrophilic (initially PDMS is highly hydrophobic) which helps when filling the channel with liquid and has also been reported to increase cell adhesion to the surface [66]. Main drawback of plasma activation is the high cost of the procedure in comparison with other techniques. One inexpensive method was first proposed by Quake research group in Pasadena [67] and it relates to the fabrication of the two PDMS layers with different ratios of base and curing agent. Nevertheless, this procedure is not valid when the ratio of the mix has to be the same in

both sides of the device or when a specific ratio value is required regarding a particular cellular behaviour on the substrate [68]. Other reported techniques consist in using PDMS curing agent as glue between layers [69] or partial curing of the elastomer, where PDMS sheets are put together when they are hard enough to manipulate but still not fully crosslinked. PDMS can also be bonded to other substrates, like glass, by means of its natural adherence or by oxygen plasma activation [70].

In this chapter, devices are replicated from the masters following two different procedures. One involves the sealing technique of PDMS based on the different proportions of base and curing agent and the other maintains the ratio suggested by the fabricant and bonds the two parts by oxygen plasma exposure. In both cases, the final device is identical and the choice of one or another depends on the available laboratory facilities. Moreover, in both techniques, both a whole and half channel can be obtained. Even though in further explanations we will work with half channel, the flat cover of the device can be replaced by a symmetric channel.

3.3.3.1. Different PDMS ratios technique

Once the masters with different roughness values are manufactured on soda-lime glass, they are replicated in PDMS by using soft-lithography methods and sealed by mixing the two PDMS parts, cover and channel, with different base-curing agent proportions. A scheme of this replication process is shown in Figure 3.18. Firstly, the soda-lime glass master is filled with silicone to obtain an inverse mould of the structure. Secondly, in order to obtain a sealed and covered channel, the protocol proposed by Quake group [67] is followed. PDMS in a ratio 5:1 (base monomer:curing agent), with an excess of curing agent according to the supplier specifications, is mixed and the silicone mould of the channel is completely covered with this mixture. For fabricating the final device, a PDMS cover for the structure is prepared by mixing the material in a ratio 20:1 (base monomer:curing agent), with an excess of monomer. As it was

mentioned, in order to obtain a circular profile device instead half, the cover is replaced by a replica of the channel with an excess of base. The two pieces (channel and cover) are both degasified into a vacuum chamber at 120 mbar for 1 hour in order to remove all the bubbles that could interfere in the final device. Then, both parts are partially cured at a furnace for 2 hours at 40 ºC. At this point, the silicone is peeled out from the PDMS to recover the initial channel. The holes for the connections are made with a punch of 3 mm and the PDMS channel and the cover are put together. The whole device is totally cured at 80 ºC for another 2 hours. The same procedure is carried out for the four soda-lime glass masters with different roughness, obtaining four closed devices that mimic half blood vessels with different roughness. The cover is around 2 mm thick and the height of the closed channel in PDMS is about 7 mm.

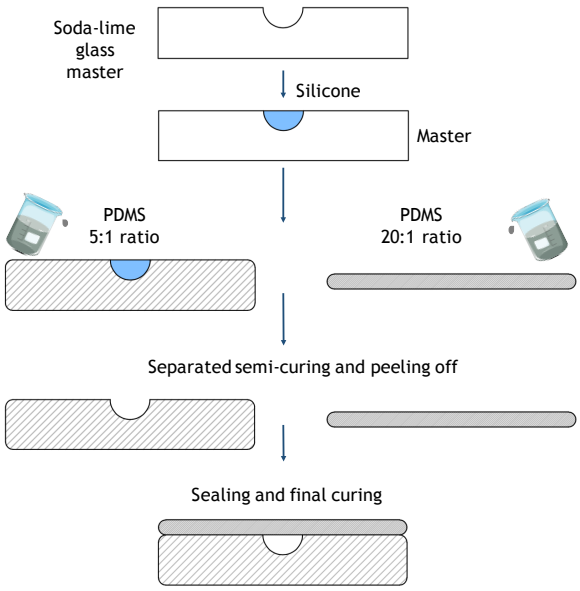

Figure 3.18: Scheme of soft-lithography process by different ratios procedures. Soda-lime glass master is fabricated with laser and thermal treatment. An inverse mould is obtained from the master with silicone. The inverse mould is covered with PDMS in a ratio 5:1 and it is partially cured. PDMS is peel off from the mould and totally cured with a cover of PDMS made in a ratio 20:1, obtaining the final device.

3.3.3.2. Oxygen plasma treatment

Other technique for fabricating sealed and close preclinical devices consist in the employment of oxygen plasma for oxidize the surface and bond the two parts. In this case, PDMS is always prepared by following the fabricant specifications so the ratio 10:1 base:curing agent is maintained. The silicone mould of the soda-lime masters is also performed, as in the above-mentioned bonding technique. This silicone is covered with PDMS and also degasified for one hour into a vacuum chamber at 120 mbar. Then, PDMS is totally cured in a furnace at 40 ºC for 3 hours. This temperature cannot be higher due to the presence of the silicone. The cover, or other symmetric channel, is done by following the same procedure. Once that both layers of PDMS are cured, connections are drilled and the parts are introduced into the chamber of a plasma cleaner for their surface activation. First, vacuum is performed in the chamber, reaching 0.1 mbar. Then, extra pure oxygen is introduced into the chamber for 3 minutes until a pressure of 0.4 mbar is reached. Then, the generator is activated and the plasma is initiated. Power is set up at 50 W and exposure lasts 30 seconds. Finally, the plasma cleaner vents and reaches ambient pressure. In this moment, the channel and the cover get in contact and introduced into a furnace to receive a thermal treatment of 20 minutes at 100 ºC. After this time, the device is ready for performing flux assays. A scheme of this process is shown in Figure 3.19.

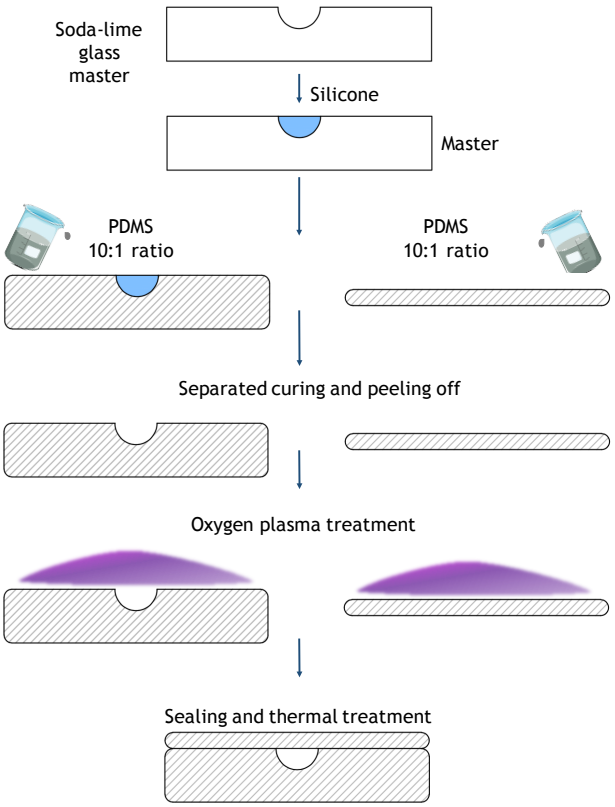

Figure 3.19: Scheme of soft-lithography process by plasma activation. Soda-lime glass master is fabricated with laser and thermal treatment. An inverse mould is obtained from the master with silicone. The inverse mould is covered with PDMS in a ratio 10:1 and it is totally cured. PDMS is peel off from the mould and the device and the cover are activated by oxygen plasma. They are put together and a thermal treatment is applied.

The device has identical dimensions and characteristics by both sealing procedures. Figure 3.20 shows photographs of the final device in PDMS.

Figure 3.20: Photographs of the final device in PDMS. The structure is embedded in a PDMS disc of 6 cm.

3.4. CONCLUSIONS

In this chapter, the techniques based in laser ablation for fabricating preclinical devices with different dimensions, from micrometre to millimetre, were stablished. Different absorbing mechanisms of direct laser ablation were presented. The physical aspects involving laser-matter interaction for different materials, laser wavelengths and pulse duration were reviewed. Shortly, for transparent materials in short pulses the main absorption mechanism is avalanche ionization, whilst in opaque substrates linear absorption domains. In the case of ultrashort pulses, the phenomena are non-linear, highlighting multiphoton absorption and tunnelling ionization. Also, indirect ablation methods were explained, in particular, laser-induced plasma-assisted ablation.

Microchannels, as basic unit of microfluidic devices, were manufactured over soda-lime glass using three pulsed laser systems operating in the near-infrared spectral region with different temporal regimes: nanosecond, picosecond and femtosecond. Optimal laser parameters for each situation were determined, as well as the effect of the number of laser scans in the depth and diameter of the structure. It was found that tin impurities presented in one side of the glass and derived from the fabrication process of the material, play a key role in the ablation process, being crucial for the manufacturing of good quality microchannels, regardless the pulse duration employed.

Structures with similar diameter and depth were obtained with the three lasers but significant differences were found among the resulting channels. Whilst in the nanosecond regime low roughness channels were fabricated, the structures manufactured with the picosecond and femtosecond pulses had a high roughness value in the walls of the channel. Moreover, more material was removed with shorter pulses than with the long ones. Thermal treatments into a static furnace were applied to the channels. By this method, the roughness of the structures has been modified in a controlled manner depending on the final applications that the channels will be used for.

In the last part of this chapter, a laser-based technique combined with a thermal treatment and soft-lithography methods were employed to fabricate PDMS devices that mimic coronary bifurcations with the final aim of performing biomedical assays and studying pathologies in-vitro conditions. This technique consisted in two main steps: first the master is fabricated and then it is replicated in PDMS material for future cell culture. The initial structure was manufactured over soda-lime glass by LIPAA process employing a nanosecond laser in the infrared spectral range. As roughness of the walls of the channel is a key factor for the future adhesion of endothelial cells to the device, it was modified in a controlled manner by applying thermal treatments to the samples. Two approaches were taken in this chapter. One was a process that combined CO_2 laser irradiation with a roller furnace. Due to the long process time involved in this step, other method was applied. It consisted in conventional thermal treatments into a static furnace to melt the sample and reduce the roughness. Once the master of the device was manufactured, the structure was replicated in PDMS by soft-lithography. For this purpose, two different replication and sealing methods were carried out. One consisted in the fabrication of the device parts with different PDMS ratios and the other involved the use of oxygen plasma exposure for bonding the elements. In both cases, the final device was the same, obtaining a structure that imitates blood vessels and that was ready for its cellular functionalization for biomedical assays. Nevertheless, oxygen plasma technique was presented like a more repeatable method with less error margin in the

fabrication, while the technique based in different PDMS ratios were more delicate due to the handling of a very soft part of the device.

REFERENCES

[1] X. Liu, D. Du, and G. Mourou, "Laser ablation and micromachining with ultrashort laser pulses," *Quantum Electron. IEEE J.*, vol. 33, no. 10, pp. 1706–1716, 1997.

[2] J. C. Miller, Ed., *Laser ablation. Principles and applications.* Berlin: Springer-Verlag, 1994.

[3] N. M. Bulgakova and A. V Bulgakov, "Pulsed laser ablation of solids: transition from normal vaporization," *Appl. Phys. A*, vol. 73, no. 2, pp. 199–208, 2001.

[4] B. C. Stuart, M. D. Feit, A. M. Rubenchik, B. W. Shore, and M. D. Perry, "Laser-induced damage in dielectrics with nanosecond to picosecond pulses," *Phys. Rev. Lett.*, vol. 74, no. 12, pp. 2248–2251, 1995.

[5] A. A. Manenkov, "Fundamental mechanisms of laser- induced damage in optical materials: today' s state of understanding and problems problems," *Opt. Eng*., vol. 53, no.1, pp. 010901, 1-7, 2018.

[6] R. Osellame, G. Cerullo, and R. Ramponi, Eds., *Femtosecond laser micromachining: photonic and microfluidic devices in transparent materials (Vol. 123)*. Berlin: Springer Science & Business Media, 2012.

[7] E. G. Gamaly, A. V. Rode, B. Luther-Davies, and V. T. Tikhonchuk, "Ablation of solids by femtosecond lasers: Ablation mechanism and ablation thresholds for metals and dielectrics," *Phys. Plasmas*, vol. 9, no. 3, p. 949-957, 2002.

[8] K. Furusawa, K. Takahashi, H. Kumagai, K. Midorikawa, and M. Obara, "Ablation characteristics of Au, Ag, and Cu metals using a femtosecond Ti: sapphire laser," *Appl. Phys. A*, vol. 366, no. 1, pp. 359–366, 1999.

[9] S. Nolte, C. Momma, H. Jacobs, A. Tünnermann, B. N. Chichkov, B. Wellegehausen, and H. Welling, "Ablation of metals by ultrashort laser pulses," *J. Opt. Soc. Am. B*, vol. 14, no. 10, pp. 2716–2722, 1997.

[10] K. Leitz, B. Redlingshöfer, Y. Reg, A. Otto, and M. Schmidt, "Metal ablation with short and ultrashort laser pulses," *Phys. Proc.*, vol. 12, pp. 230–238, 2011.

[11] C. Ropers, D. R. Solli, C. P. Schulz, C. Lienau, and T. Elsaesser, "Localized multiphoton emission of femtosecond electron pulses from metal nanotips," *Phys. Rev. Lett.*, vol. 98, no. 4, pp. 043907, 1-4 , 2017.

[12] T. E. Itina, M. Mamatkulov, and M. Sentis, "Nonlinear fluence dependencies in femtosecond laser ablation of metals and dielectric materials," *Opt. Eng.*, vol. 44, no. 5, pp. 051109, 1-8, 2005.

[13] P. P. Pronko, S. K. Dutta, J. Squier, J. V Rudd, D. Du, and G. Mourou, "Machining of sub-micron holes using a femtosecond laser at 800 nm," *Opt. Comm.*, vol. 114, no. 1-2, pp. 106–110, 1995.

[14] S. I. Anisimov, B. L. Kapeliovich, and T. L. Perelman "Electron emission from metal surfaces exposed to ultrashort laser pulses," *Sov. Phys. JETP*, vol. 66, no. 2, pp. 375-377, 1974.

[15] J. K. Chen, and J. E. Beraun, "Numerical study of ultrashort laser pulse interactions with metal films," *Numer. Heat Transfer A*, vol. 40, no. 1, pp. 1–20, 2001.

[16] J. K. Chen, "A semiclassical two-temperature model for ultrafast laser heating," *Int. J Heat Mass Transfer*, vol. 49, no. 1-2, pp. 307–316, 2006.

[17] M. Lenzner, J. Krüger, S. Sartania, Z. Cheng, C. Spielmann, G. Mourou, W. Kautek, and F. Krausz, "Femtosecond optical breakdown in dielectrics," *Phys. Rev. Lett.*, vol. 80, no. 18, pp. 4076-4079, 1998.

[18] K. Sugiola and Y. Cheng, *Femtosecond laser 3D micromachinig for microfluidics and optofluidic applications.* London: Springer, 2014.

[19] L. V. Keldysh, "Ionization in the field of a strong electromagnetic wave," *Soviet Phy. JEPT,* vol. 20, no. 5, pp. 1307-1014, 1965.

[20] S. K. Sundaram and E. Mazur, "Inducing and probing non-thermal transitions in semiconductors using femtosecond laser pulses," *Nature Mat*., vol. 1, no. 4, pp. 217-224, 2002.

[21] S. S. Mao, F. Quéré, S. Guizard, X. Mao, R. E. Russo, G. Petite, and P. Martin, "Dynamics of femtosecond laser interactions with dielectrics," *Appl. Phys. A*, vol. 79, no. 7, pp. 1695-1709, 2004.

[22] N. M. Bulgakova, R. Stoian, A. Rosenfeld, I. V. Hertel, W. Marine, and E. E. B. Campbell, "A general continuum approach to describe fast electronic transport in pulsed laser irradiated materials: The problem of Coulomb explosion," *Appl. Phys. A*, vol. 81, no. 2, pp. 345-356, 2005.

[23] M. V Shugaev, C. Wu, O. Armbrustervb, A. Naghilau, N. Brouwer, D. S. Ivanov, T. J. Y. Derrien, N. M. Bulgakova, W. Kautek, B. Rethfeld, and L. V. Zhigilei, "Fundamentals of ultrafast laser – material interaction," *MRS Bulletin*, vol. 41, no. 12, pp. 960–968, 2016.

[24] B. N. Chichkov, C. Momma, S. Nolte, F. von Alvensleben, and A. Tünnermann, "Femtosecond, picosecond and nanosecond laser ablation of solids," *Appl. Phys. A,* vol. 63, no. 2, pp. 109–115, 1996.

[25] A. H. Hammad, "Effects of different laser pulse regimes (nanosecond, picosecond and femtosecond) on the ablation of materials for production of nanoparticles in liquid solution," in *High Energy and Short Pulse Laser,* R. Viskup, Eds. InTechOpen, 2016. pp. 305-325.

[26] K. C. Phillips, H. H. Gandhi, E. Mazur, and S. K. Sundaram, "Ultrafast laser processing of materials: a review," *Adv. Opt. Photonics*, vol. 7, no. 4, p. 684-712, 2015.

[27] J. Zhang, K. Sugioka, and K. Midorikawa, "High-quality and high-efficiency machining of glass materials by laser-induced plasma-assisted ablation using conventional nanosecond UV, visible, and infrared lasers," *App. Phys. A*, vol. 69, no.1, pp. 879–882, 1999.

[28] S. Nikumb, Q. Chen, C. Li, H. Reshef, H.Y. Zheng, H. Qiu, and D. Low "Precision glass machining, drilling and profile cutting by short pulse lasers," *Thin Solid Films,* vol. 477, no. 1-2, pp. 216-221, 2015.

[29] J. Zhang, K. Sugioka, and K. Midorikawa, "Laser-induced plasma-assisted ablation of fused quartz using the fourth harmonic of a Nd+: YAG laser," *Appl. Phys. A*, vol. 67, no. 5, pp. 545–549, 1998.

[30] J. Zhang, K. Sugioka, and K. Midorikawa "Direct fabrication of micrograting in fused quartz by laser-induced plasma-assisted ablation with a KrF excimer laser," *Opt. Lett.*, vol. 23, no. 18, pp 1486-1488, 1998.

[31] A. Castelo, D. Nieto, C. Bao, M. T. Flores-Arias, M. V. Pérez, c. Gómez-Reino, C. López-Gascón, and G. F. de la Fuente, "Laser backwriting process on glass via ablation of metal targets," *Opt. Commun*., vol. 273, no. 1, pp. 193–199, 2007.

[32] Y. Hanada, K. Sugikiola, Y. Gomi, H. Yamaoka, O. Otsuki, I. Miyamoto, and K. Midorikawa, "Development of practical system for

laser-induced plasma-assisted ablation (LIPAA) for micromachining of glass materials," *Appl. Phys. A*, vol. 79, no. 4-6, pp. 1001-1003, 2004.

[33] Y. Hanada, K. Sugioka, I. Miyamoto, and K. Midorikawa, "Double-pulse irradiation by laser-induced plasma-assisted ablation (LIPAA) and mechanisms study," *Appl. Surf. Sci.,* vol. 248, no. 1-4, pp. 276–280, 2005.

[34] K. Sugioka, K. Obata, M. H. Hong, D. J. Wu, L. L. Wong, Y. F. Lu, T. C. Chong, and K. Midorikawa, "Hybrid laser processing for microfabrication of glass," *Appl. Surf. Sci.,* vol. 77, no. 2, pp. 251–257, 2003.

[35] H. Varel, D. Ashkenasi, A. Rosenfeld, R. Herrmann, F. Noack, and E. E. B. Campbell, "Laser-induced damage in SiO_2 and CaF_2 with picosecond and femtosecond laser pulses," *Appl. Phys. A*, vol. 62, no. 3, pp. 293–294, 1996.

[36] D. Nieto, J. Arines, G. M. O´Connor, and M. T. Flores-Arias, "Single-pulse laser ablation threshold of borosilicate, fused silica, sapphire, and soda-lime glass for pulse widths of 500 fs, 10 ps, 20 ns," *Appl. Opt.*, vol. 54, no. 29, pp. 8596-8601, 2015.

[37] D. Du, x. Liu, G. Korn, J. Squier, and G. Mourou"Laser induced breakdown by impact ionization in SiO_2 with pulse widths from 7 ns to 150 fs," *Appl. Phys. Lett*., vol. 64, no. 23, pp. 3071-3073, 1994.

[38] A. Weck, T. H. R. Crawford, D. S. Wilkinson, H. K. Haugen, and J. S. Preston, "Laser drilling of high aspect ratio holes in copper with femtosecond, picosecond and nanosecond pulses," *Appl. Phys. A*, vol. 90, no. 3, pp. 537–543, 2008.

[39] T. Koyama and K. Tsunemoto, "Laser micromachining of silicate glasses containing silver ions using a pulsed laser," *Jpn. J. Appl. Phys.*, vol. 36, no. 2B, pp. 244-247, 1997.

[40] J. Bonse, J. Solis, L. Urech, T. Lippert, and A. Wokaun, "Femtosecond and nanosecond laser damage thresholds of doped and undoped triazenepolymer thin films," *Appl. Surf. Sci.,* vol. 253, no. 19, pp. 7787-7791, 2007.

[41] M. Aymerich, D. Canteli, J. R. Vázquez de Aldana, C. Molpeceres and M. T. Flores-Arias "Comparative study of high-quality microchannels fabricated over soda-lime glass with near-infrared nano, pico and femtosecond pulses," Under preparation.

[42] E. Bulushev, V. Bessmeltsev, A. Dostovalov, N. Goloshevsky, and A. Wolf, "High-speed and crack-free direct-writing of microchannels on glass by an IR femtosecond laser," *Opt. Lasers Eng*., vol. 79, pp. 39–47, 2016.

[43] A. M. Ross, Z. Jiang, M. Bastmeyer, and J. Lahann, "Physical aspects of cell culture substrates: Topography, roughness, and elasticity," *Small*, vol. 8, no. 3, pp. 336–355, 2012.

[44] C. J. Mcaloon, L. M. Boylan, T. Hamborg, N. Stallard, F. Osman, P. B. Lim, and S. S. Hayat, "The changing face of cardiovascular disease 2000 – 2012: An analysis of the world health organisation global health estimates data," *Int. J. Cardiol*., vol. 224, pp. 256–264, 2016.

[45] L. J. Laslett, P. Alagona, B. A. Clark, J. P. Drozda, F. S. Saldivar, S. R. Wilson, C. Poe, and M. Hart, "The worldwide environment of cardiovascular disease: prevalence, diagnosis, therapy, and policy issues. A report from the American College of Cardiology," *JAC*, vol. 60, no. 25, pp. S1–S49, 2012.

[46] A. Rezvan, C.W. Ni, N. Alberts-Grill, and H. Jo, "Animal, in vitro, and ex vivo models of flow-dependent atherosclerosis: role of oxidative stress," *Antioxid. Redox Signal.*, vol. 15, no. 5, pp. 1433–1448, 2011.

[47] M. Tsai, A. Kita, J. Leach, R. Rounsevell, J. N. Huang, J. Moake, R. E. Ware, D. A. Fletcher, and W. A. Lam, "In vitro modelling of the microvascular occlusion and thrombosis that occur in hematologic diseases using microfluidic technology," *J. Clinical Inv.,* vol. 122, no. 1, pp. 408-410, 2012.

[48] M. Shin, K. Matsuda, O. Ishii, H. Terai, M. Kaazempur-Modrad, J. Borestein, M. Detmar, and J. P. Vacanti "Endothelialized networks with a vascular geometry in microfabricated poly(dimethyl siloxane)," *Biomed. Microdevices*, vol. 6, no. 4, pp. 269–278, 2004.

[49] C. Wang, B. M. Baker, C. S. Chen, and M. A. Schwartz, "Endothelial cell sensing of flow direction," *Arterioscler. Thromb. Vasc. Biol*., vol. 33, no. 9, pp. 2130–2136, 2013.

[50] J. S. Uzarski, E. W. Scott, and P. S. McFetridge, "Adaptation of endothelial cells to physiologically-modeled, variable shear stress," *PLoS One*, vol. 8, no. 2, pp. 17–19, 2013.

[51] S. Chung, R. Sudo, V. Vickerman, I. K. Zervantonakis, and R. D. Kamm, "Microfluidic platforms for studies of angiogenesis, cell migration, and cell-cell interactions," *Ann. Biomed. Eng.,* vol. 38, no. 3, pp. 1164-1177, 2010.

[52] E. L. Fong, M. Santoro, M. C. Farach-carson, F. K. Kasper, and A. G. Mikos, "Tissue engineering perfusable cancer models," *Curr. Opin. Chem. Eng*., vol. 3, pp. 112–117, 2014.

[53] J. W. Song, S. P. Cavner, A. C. Walker, K. E. Luker, M. Gupya, Y. C. Tung, G. D. Luker, and S. Takayama "Microfluidics endothelium for studying the intravascular adhesion of metastatic breast cancer cells," *PLoS One,* vol. 4, no. 6, pp. 5756, 1-10, 2009.

[54] K. C. Chaw, M. Manimaran, F. E. H. Tay, and S. Swaminathan, "A quantitative observation and imaging of single tumor cell

migration and deformation using a multi-gap microfluidic device representing the blood vessel," *Microvas. Res*., vol. 72, no. 3, pp. 153–160, 2006.

[55] A. M. Ghaemmaghami, M. J. Hancock, H. Harrington, H. Kaji, and A. Khademhosseini, "Biomimetic tissues on a chip for drug discovery," *Drug Discov. Today*, vol. 17, no. 3–4, pp. 173–181, 2012.

[56] L. K. Fiddes, N. Raz. S. Srigunpalan, E. Tumarkan, C. A. Simmosn, A. R. Wheeler, and E. Kumacheva, "A circular cross-section PDMS microfluidics system for replication of cardiovascular flow conditions," *Biomaterials*, vol. 31, no. 13, pp. 3459–3464, 2010.

[57] A. D. van der Meer, V. V. Orlova,P. ten Dijke, A. van den Berga, and C. L. Mummery, "Three-dimensional co-cultures of human endothelial cells and embryonic stem cell-derived pericytes inside a microfluidic device," *Lab Chip,* vol. 13, no. 18, pp. 3562-3568, 2013.

[58] Y. Zheng, Y. Zheng, J. Chen, M. Craven, N. W. Choi, S. Totorica, A. Diaz-Santana, and P. Kermani, "In vitro microvessels for the study of angiogenesis and thrombosis," *Proc. Natl. Acad. Sci*., vol. 109, no. 24, pp. 9342–9347, 2012.

[59] M. Aymerich, E. Álvarez, C. Bao-Varela, I. Moscoso, J. R. González-Juanatey, and M. T. Flores-Arias, "Laser technique for the fabrication of blood vessels-like models for preclinical studies of pathologies under flow conditions," *Biofabrication*, vol. 9, no. 2, pp. 025033, 1-7, 2017.

[60] T. Delgado, D. Nieto, and M. T. Flores-Arias, "Fabrication of microlens arrays on soda-lime glass using a laser direct-write technique and a thermal treatment assisted by a CO2 laser," *Opt. Lasers Eng*., vol. 73, pp. 1–6, 2015.

[61] X. Li, S. M. Mearns, M. Martins-Green, Y. Liu, "Procedure for the development of multi-depth circular cross-sectional

endothelialized microchannels-on-a-chip," *J. Visualized Experiments,* vol. 80, pp. 1-2, 2013.

[62] M. A. Eddings, M. A. Johnson, and B. K. Gale, "Determining the optimal PDMS-PDMS bonding technique for microfluidic devices," *J. Micromechanics Microengineering*, vol. 18, no. 6, pp. 1-4, 2008.

[63] C. S. Effenhauser, G. J. M. Bruin, A. Paulus, and M. Ehrat, "Integrated capillary electrophoresis on flexible silicone microdevices: analysis of DNA restriction fragments and detection of single DNA molecules on microchips," *Anal. Chem*., vol. 69, no. 17, pp. 3451–3457, 1997.

[64] B. H. Jo, L. M. Van Lerberghe, K. M. Motsegood, and D. J. Beebe, "Three-dimensional micro-channel fabrication in polydimethylsiloxane (PDMS) elastomer," *J. Microelectromechanical Syst*., vol. 9, no. 1, pp. 76–81, 2000.

[65] S. Bhattacharya, A. Datta, J. M. Berg, and S. Gangopadhyay, "Studies on surface wettability of poly(dimethyl) siloxane (PDMS) and glass under oxygen-plasma treatment and correlation with bond strength," *J. Microelectromechanical Syst*., vol. 14, no. 3, pp. 590–597, 2005.

[66] D. Fuard, T. Tzvetkova-Chevolleau, S. Decossas, P. Tracqui, and P. Schiavone, "Optimization of poly-di-methyl-siloxane (PDMS) substrates for studying cellular adhesion and motility," *Microelectron. Eng.*, vol. 85, no. 5–6, pp. 1289–1293, 2008.

[67] M. A. Unger, H. P. Chou, T. Thorsen, A. Scherer, and S. R. Quake, "Monolithic microfabricated valves and pumps by multilayer soft lithography.," *Science*, vol. 288, no. 5463, pp. 113–116, 2000.

[68] X. Q. Brown, K. Ookawa, and J. Y. Wong, "Evaluation of polydimethylsiloxane scaffolds with physiologically-relevant elastic moduli: Interplay of substrate mechanics and surface chemistry effects

on vascular smooth muscle cell response," *Biomaterials*, vol. 26, no. 16, pp. 3123–3129, 2005.

[69] B. Samel, M. K. Chowdhury, and G. Stemme, "The fabrication of microfluidic structures by means of full-wafer adhesive bonding using a poly(dimethylsiloxane) catalyst," *J. Micromechanics Microengineering*, vol. 17, no. 8, pp. 1710–1714, 2007.

[70] L. Xiong, P. Chen, and Q. Zhou, "Adhesion promotion between PDMS and glass by oxygen plasma pre-treatment," *J. Adhes. Sci. Technol*., vol. 28, no. 11, pp. 1046–1054, 2014.

4. DEVICE APPLICABILITY: FUNCTIONALIZATION, SOL-GEL COATINGS AND DETERMINATION OF LOW VELOCITY AREAS

In this chapter, we present the validation of the preclinical devices previously fabricated in PDMS. In order to obtain a functional device that imitates a blood vessel, in particular a coronary bifurcation, the walls of the device must be fully covered with endothelial cells that resist flux conditions when experiments are carried out. Human umbilical vein endothelial cells (HUVEC) are employed for this purpose and they are cultured all over the channel inner structure to create the simulated environment of the inside of a vessel. In the former chapter, chips with different roughness values were obtained by means of thermal treatments of the master. The impact of the roughness of the walls in cell attachment and spreading is evaluated, finding the optimal device configuration for preforming flux assays. Moreover, the problem of PDMS degradation with organic solvents is solved in this chapter. When PDMS is exposed to certain organic solvents commonly employed in biomedical laboratories, such as ethanol, the material deteriorates and leads to an anomalous cellular growth in the next cell culture. This fact makes the devices non-reusable, since when they are cleaned between usages the surface becomes unserviceable. This situation is overcome by coating the PDMS surface with sol-gel films that confers to the elastomer the resistance of glass. By dip-coating technique, different sol-gel compositions are employed and cellular results are analysed regarding the type of sol-gel. Finally, the devices are employed for experimentally verifying the low velocity zones in coronary bifurcations regarding the angle between the branches. In these areas, fluid velocity and shear stress are lower and there is turbulent and

oscillating flow. Fluid behaviour becomes anomalous and an alteration of proper hemodynamic factors may lead to a higher risk of vascular problems like stenosis or atherosclerosis. Hence, the identification of these zones will help in the understanding of these pathologies. Experimental results are compared with theoretical ones derived from numerical simulations.

4.1. CELLULAR VALIDATION

In Chapter 3, a method for fabricating preclinical devices that imitate coronary bifurcations was presented. It combines laser technologies to manufacture the master in soda-lime glass with soft-lithography methods for obtaining the final chip in PDMS, suitable material for long term cell cultures. The aim of this device is to simulate the environment of a blood vessel in laboratory in vitro conditions, so cellular lining of the walls is required for its functionalization. Some studies report structures with several cell layers in the channel to obtain a more realistic device with the three kinds of cells presented in blood vessels: a layer of endothelial cells in the inner wall (tunica intima), dense populations of smooth muscle cells in the middle (tunica media) and a collagenous extracellular matrix with fibroblast and nerve cells in the outer zone that act as a protective coating for the vessels (tunica externa) [1, 2]. This multi-layer approach is important when interaction between layers and cell migration is object of study but when the analysis of the impact of flux in vessels is the main goal of the research, the simplest approach and most important aspect is to have an endothelial monolayer attached to the channel walls that withstands the flow through the device while bioassays are carried out [3]. These perfusable in vitro 3D models of blood vessels are really important for understanding the functioning of vasculature and the development of cardiovascular diseases that are one of the major causes of fatalities in the world. There exists the need of tissue engineered artificial blood vessels for the study of atherosclerosis, stenosis, heart attack or hypertension, among others [4]. Whilst cells have been traditionally cultured in 2D,

they should be seeded in 3D environments that imitate the real one for a better comprehension of the behaviour of the human body [5, 6].

Typically, cells do not grow and adhere properly to PDMS surfaces [7], so surface pre-treatments are required in order to create a proper model to which the endothelial cells adhere. One of the most common pre-treatments consist on the use of hydrogels. Hydrogels are 3D networks of polymers that share characteristics with natural extra-cellular environments, promoting the growth and adhesion of cells [8, 9]. Some of these are polyethylene glycol diacrylate (PEGDA) [10], polyethylene glycol methacrylate (PEGMA) [11] or gelation methacrylate (GelMA) [12, 13]. Their employment allows 3D culture of cells but they present some important disadvantages, like their cost or the complex protocols that these materials need.

One efficient solution to overcome the adherence problem of cells to the PDMS is to manipulate the roughness of the device to enhance the attachment of the endothelial cells to the walls. Surface properties of materials affect cell behaviour, determining cell attachment, proliferation and differentiation [14]. It has been demonstrated that physical aspects like elasticity, topography or roughness of the substrate play an important role in the growth and spread process of the cell [15-18], depending on the kind of material and type of cell. In our case, the roughness is presented as a key factor for functionalizing the surface in an easy and low cost way. The initial roughness of the master structure, derived from the laser fabrication process, can be modified in a controlled manner by applying a thermal treatment to the substrate. This roughness is replicated in the PDMS final device. In this section, the cell culture procedure to fully cover the channel is presented. Moreover, the impact of roughness in HUVEC attachment is evaluated by comparing cell adhesion and resistance to flux in the devices manufactured from four masters with different roughness values.

4.1.1. Cell culture procedure

For the cell culture, human umbilical vein endothelial cells (HUVEC) are employed. They are obtained from umbilical cords donated after informed consent from the mothers. This protocol was approved by the Ethics Committee for Human Studies in Galicia (Spain) in accordance to the Declaration Helsinki in 1975. HUVEC are isolated and cultured following the protocol described by Rodiño-Janeiro et al. [19]. Briefly, HUVEC are cultured in endothelial growth medium (EGM-2, Lonza, Basle, Switzerland) with gentamicin/amphotericin B, under standard incubation conditions: 37 ºC temperature, more than 80% humidity and 5% CO_2. Cells are stained with calcein AM (Invitrogen, Thermo Fischer Scientific, Waltman, MA, USA) for 4 minutes at 37 ºC. This is a cell-permanent dye that converts in green-fluorescent calcein when cells are alive, so in fluorescence microscopy inspections it serves as a viability indicator. In order to remove the excess of calcein after its cell loading, the HUVECs are washed twice in EGM-2.

To mimic a blood vessel and to perform preclinical bioassays, the device must be completely covered by endothelial cells. Due to the large dimensions of the channel, the cell culture is carried out in two steps. First of all, the PDMS device is sterilized in an autoclave at 120 ºC for 30 minutes, as it was reported to be a suitable protocol to clean the device that does not degrades the material [20]. As it will be explained later, organic solvents can damage the PDMS and lead to an anomalous cell growth in the surface of the material. Once the channel is sterilized, endothelial growth medium (EGM-2) is perfused through the channel for 30 minutes. Then, HUVEC are cultured in the PDMS device in order to achieve an in vitro model that simulates a blood vessel. Cells are seeded over the bottom surface of the channel at a concentration of 10^6/200 µl. The device is placed inside an incubator at standard cell culture conditions overnight to let the cells attach the surface and form a monolayer. The holes for the connections are closed to avoid the evaporation of the medium, which could lead to a failure of the experiment. At this point, only the bottom wall of the

channel has endothelial cells. In order to achieve attached cells over the whole channel, the same protocol is repeated the next day once the device is turned around and stained cells are cultured over the other wall. The same concentrations and procedure times are employed in both cases. The lateral walls are covered by the excess of the cultured cells seeded during this two-day process. Figure 4.1 depicts the results of this cell culture procedure under fluorescence illumination for the situation of a channel with semi and circular profile.

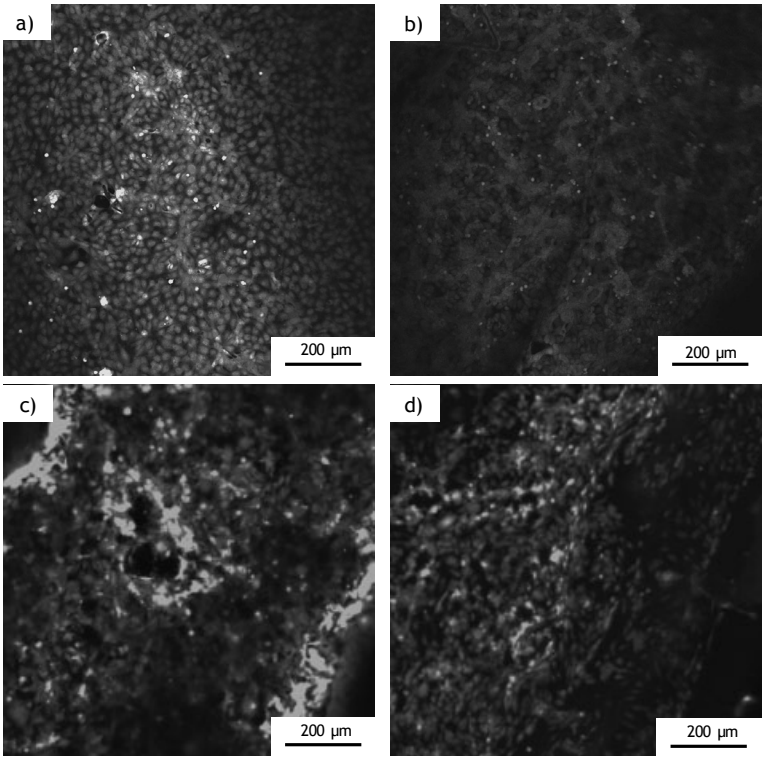

Figure 4.1: Fluoresencence microscpy images of the a) top and b) bottom of the channel when it has a semi-circular profile and c) top and d) bottom of the whole circular channel.

In Figure 4.1 it can be seen that an endothelial cell monolayer is formed in the totality of both PDMS surfaces by following this two-step culture process. Figures 4.1.a and 4.1.b show the cover and the

bottom of the channel, respectively, when a channel with semi-circular profile is manufactured. The differences between the images are due to the different topographic characteristics of the surfaces. Whilst the channel recovered from the soda-lime master (Figure 4.1.b) has a curved surface, the manufactured cover is practically flat (Figure 4.1.a) and thus, a clearer image is obtained. Figures 4.1.c and 4.1.d present the cell culture performed in both walls of a circular profile channel.

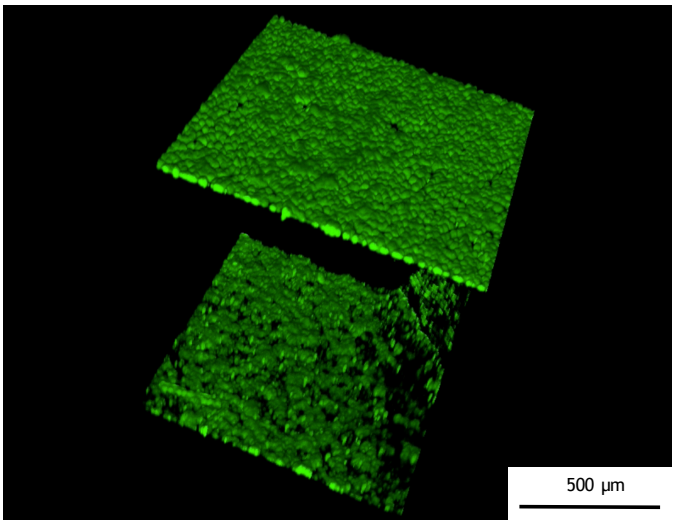

Figure 4.2: 3D fluorescence confocal image of the endothelial coating of the channel.

Figure 4.2 shows a 3D fluorescence confocal image of the channel that imitates half a blood vessel. We can see that the channel is totally coated by endothelial cells that are also present in the lateral walls of the PDMS device thanks to the cell culture in two steps explained above [21]. When working with a semi-circular profile channel, cells are not strictly needed in the top of the device, since the channel has a flat cover that does not share topography characteristics with the rest of the device and cellular response on that part could not be the same as in the rest of the channel. In fact, when the blood vessel approach is considered as a symmetry problem, the cover role

is only to avoid leaks in the device. Nevertheless, this two-step culture process is still needed since is the only way to ensure cell attach to the laterals of the walls. If HUVEC were only cultured in the bottom of the channel, cells would not adhere to the wall but remained in the lower part of the structure, obtaining a non-fully coated device. No 3D confocal image of the circular profile channel can be acquired with the available equipment due to the large height of the chip in comparison with the working distance of the microscope objectives.

4.1.2. Role of device roughness in cell adhesion

In order to have a proper blood vessel model for studying cardiovascular pathologies, the endothelial cell adhesion to the surface when flux experiments are carried out is a key factor. As it was already mentioned, surface roughness has a direct impact in cell attachment to the material [22]. The influence of the roughness of the channel walls in cell attachment when media (EGM-2) is perfused through the device is studied in order to find the best design to carry out biomedical assays avoiding cell detachment. For this purpose, PDMS devices are fabricated from four glass masters with different roughness values, presented in Chapter 3. The masters fabricated by laser-induced plasma-assisted ablation had an initial arithmetical average profile roughness of 5285.01±304.56 nm. When the glass was exposed to a thermal treatment of two hours at 590 ºC, it was reduced to 1528.01±100.01 nm. When the treatment was at 630 ºC, roughness was of 400.84±20.31 nm and 27.18±4.52 nm for the treatment at 670 ºC (see Table 3.2). The PDMS channels obtained from the masters are coated with HUVEC cells following the above-mentioned protocol and flux is implemented in the devices. Figure 4.3 shows the results before and after EGM-2 media perfusion through the four different channels. Flux is implemented in the devices at a flow rate of 1 ml/min during 8 hours.

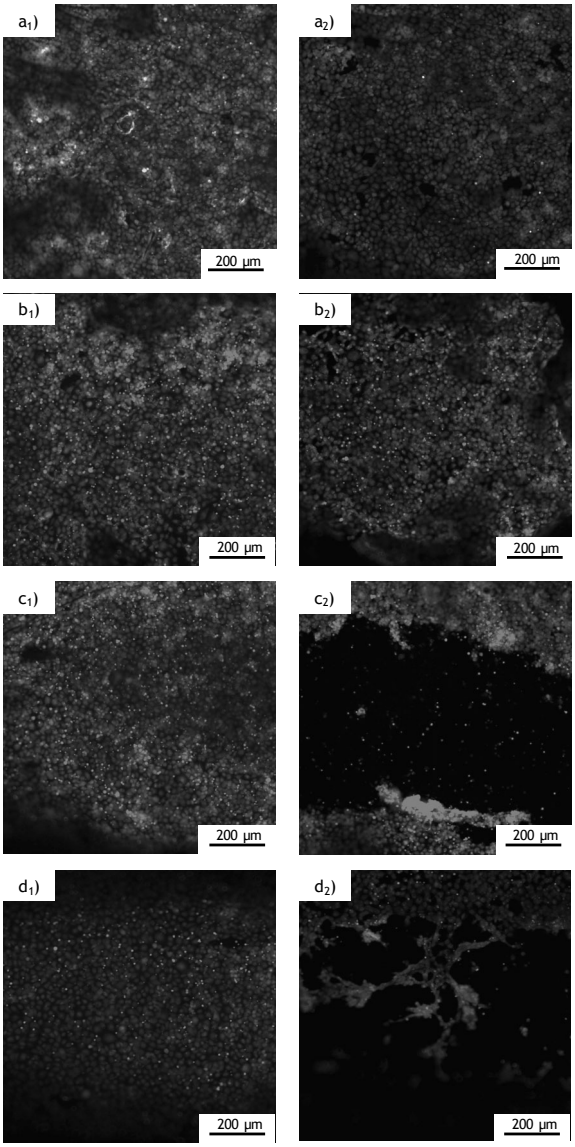

Figure 4.3: Fluorescence microscopy images of the surfaces of the PDMS channels with HUVECs cultured over them. Device fabricated from a master with a) no thermal treatment and R_a=5285.01 nm, b) with a thermal treatment at 590 ºC and R_a=1528.01 nm, c) at 630 ºC and R_a=400.84 nm and d) 670 ºC and R_a=27.18 nm. Figures with subscript 1 show the channels before flow application whereas figures with subscript 2 show the same channel after flow application.

Figures 4.3 with subscript 1 show the endothelial cell growth over the channels after the cell seeding, before any flux experiment was performed. In all of the situations, as it can be appreciated, the cells grow and spread forming a confluent monolayer. No significant differences between the designs are observed besides the image acquisition, which presents a better quality in the case of flatter surfaces due to the absence of roughness in the material. After perfusing media through the channels, corresponding to images with subscript 2 in Figure 4.3, important differences can be observed among the channels with different roughness. In the channel without thermal treatment and therefore with the higher roughness value (Figure 4.3.a), practically all HUVECs remain on the surface. As roughness value decreases and surface become smoother, cellular detachment is higher, reaching situations depicted in Figures 4.3.c and 4.3.d. When the masters with arithmetical average profile roughness values of 400.84 nm and 27.18 nm are employed for manufacturing the device, flow drags cells, suggesting that cell attachment is not as firm as in the rougher surfaces. So, although these devices present a less sharp profile, we can say that these designs are less suitable for performing experiments under real flow conditions. Figure 4.3.b presents the design created from a soda-lime master with thermal treatment at 590 ºC. It represents the best model between the four since it presents enough arithmetical average profile roughness value (1.528 μm) to avoid the cellular detachment under flow conditions and, at the same time, good optical properties to observe the cells. This device is validated until a flow rate of 10 ml/min, in the same order as coronary bifurcations [23]. In this situation, cells remain in the walls and resist the flux. Nevertheless, it should be indicated that this value is reached by gradually increasing the flow until that value in order to avoid cell detachment with a sudden change of conditions.

4.2. SOL-GEL COATINGS TO OVERCOME PDMS DEGRADATION

As it was previously mentioned, PDMS is a very suitable material for manufacturing the final preclinical devices due to properties like biocompatibility, capability to accurately reproduce the master,

competitive cost, gas permeability, transparency or non-toxicity, among others. Nevertheless, it presents a significant drawback: due to its permeability, the material degrades when is in contact with organic solvents and drugs commonly employed in cell biology. These substances, which are commonly employed in biomedical assays, degrade and deteriorate PDMS, making the device non-reusable. Due to the permeable and hydrophilic nature of PDMS, it can absorb small hydrophilic molecules [24] and organic solvents swells the material [25-27]. We propose solution to overcome this problem consists on coating the PDMS surface via sol-gel chemical route. This procedure provides the structure with the chemical robustness of the glass but retain the positive attributes of PDMS, as well as its geometry [28]. In this way, physical properties of the elastomer can be extensively modified by sol-gel chemistry, drastically reducing the absorption of drugs in cell biology, but preserving the biocompatibility, transparency and oxygen permeability of the material [29]. Sol-gel chemistry was introduced in Chapter 2 and offers some opportunities for the synthesis of materials like the control of the composition and the low processing temperature, giving an excellent control of purity since it starts with pure materials [30].

In order to depict this issue, human umbilical vein endothelial cells (HUVECs) are culture over a PDMS channel without sol-gel coating. The device is cleaned with ethanol between usages for sterilization purposes and it is reused for three times. Cells are cultured by following the same procedure as in the previous section [19] and also stained with calcein, a viability indicator. Cells are seeded at a concentration of 10^6 cells/ml and observed after one-day culture. Figure 4.4 shows the HUVEC culture in the channel when it is employed for the first and third time.

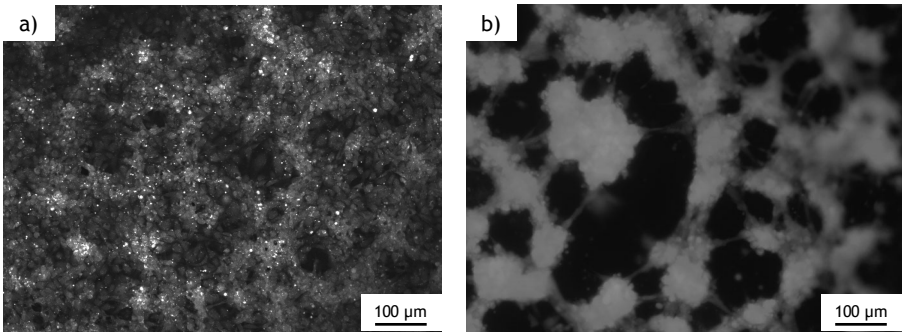

Figure 4.4: Representative fluorescence microscopy images of human umbilical vein endothelial cells growing over PDMS channel after a) the first and b) the third use of the device. The channel was cleaned between usages with ethanol.

Figure 4.4.a depicts a fluorescent image of the PDMS surface after a one-day endothelial cell culture when the device is used for the first time. In these conditions, HUVECs grow forming a confluent monolayer of cells, with the characteristic "cobblestone" morphology of endothelial cells. Figure 4.4.b shows cell growth over the same channel when it is reused three times and washed with ethanol between usages for sterilization purposes. In this situation, HUVECs growth is abnormal and they are far from forming a confluent monolayer. In contrast, they are placed over the PDMS, gathering in clusters, minimizing the surface that they share with the degraded PDMS. This situation happens with most of the organic solvents commonly employed in biomedicine and one easy solution to solve this problem is, as was previously mentioned, coating the PDMS channels with sol-gel to confer the structure the chemical robustness of the glass. In this section, PDMS devices are coated with different sol-gel compositions by dip-coating technique to overcome the deterioration problem of the material. Human umbilical vein endothelial cells are cultured onto the different coated channels and the biocompatibility of each specific device is studied.

4.2.1. Sol-gel coating

The dip-coating technique is one of the easiest techniques to obtain coatings using a liquid deposition with a huge variety of inorganic, hybrid and nanocomposite materials. It allows depositing layers and coating different complex surfaces, for instance with holes or intricate shapes, enabling a flexibility that is not possible with other conventional techniques. By coating PDMS devices with sol-gel, the geometry of the devices can be preserved but the surface where cells are going to be cultured is modified and, therefore, cellular behaviour over the material will be different compared to the behaviour over non-coated PDMS.

In dip-coating technique, the substrate to be coated is immersed in a liquid and subsequently withdrawn at a constant withdrawal speed. This process takes place under well-controlled temperature and atmospheric conditions and normally a thermal treatment is necessary to obtain the final film. The film formation involves several steps but, nevertheless, the physical and chemical processes are mostly overlapped. A scheme of the dip-coating process is represented in Figure 4.5.

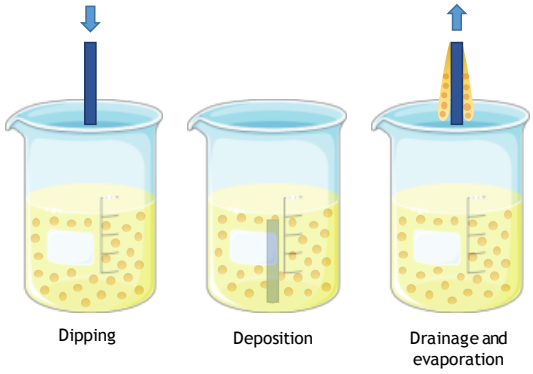

Figure 4.5: Scheme of dip-coating technique for the sol-gel coating deposition. First the PDMS is immersed into the sol precursor. Then, the substrate is withdrawn at a constant speed. Finally, solvent evaporation leads to the gelation of the film.

As it can be seen in Figure 4.5, basically the process starts with the immersion of the substrate in the coating bath. Next, the liquid film is entrained on removal the substrate from the liquid, which then consolidates by drying and accompanying chemical reactions. The consolidation step represents the sol-gel transition with associated processes of draining, evaporation and hydrolysis. The composition of the cover layers can be chosen to enhance the cell adhesion. Different silica and silica-titania sol-gel coatings are applied on PDMS channels by sol-gel dip-coating technique using methyltriethoxysilane (MTES) and tetraethylorthosilane (TEOS) as silicon dioxide precursors and titanium isopropoxide (TISP) as titanium dioxide precursor. In particular, 60MTES/40TEOS, 70MTES/30TISP and 80MTES/20TISP compositions are employed. Numbers indicate the ratio of each precursor in silica and silica titania coatings. The preparation procedures of the coatings were explained in detail in Chapter 2 and is summarised in the flow charts depicted in Figure 4.6.

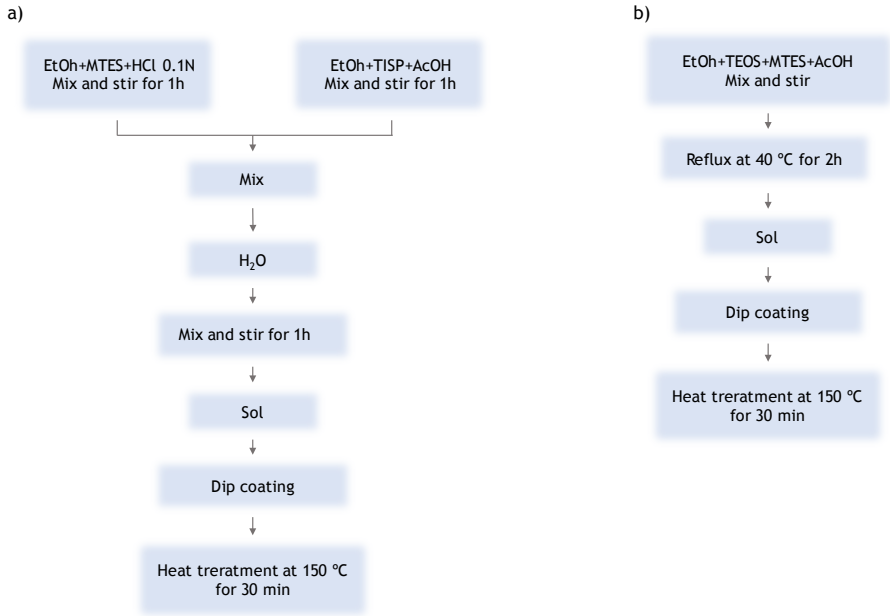

Figure 4.6: Flow charts of the preparation process of a) SiO_2-TiO_2 and b) SiO_2 layers.

As it was mentioned, the sol-gel deposition does not alter the channel morphology. Actually, its analysis by means of optical microscopy reveals the presence of some irregularities in the uncoated channel (Figure 4.7.a) that become softer after the deposition of sol-gel layers, improving the quality of the channel (Figure 4.7.b). Therefore, the sol-gel coating not only does not alter the channel structure but also enhances the surface.

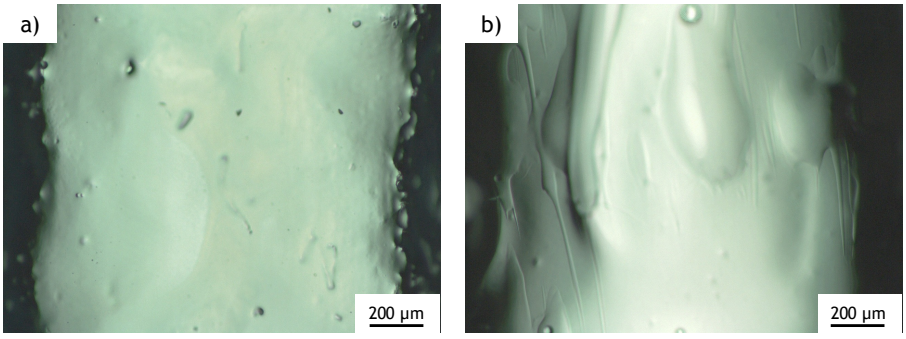

Figure 4.7: Microscope images of PDMS channel: a) uncoated and b) with sol-gel coating.

4.2.1. Cell culture over the coated devices

Once the PDMS channels are coated with sol-gel in order to increase their chemical robustness and to avoid their degradation, endothelial cell behaviour over the different coated surfaces is studied with the purpose of verifying its biocompatibility and determining which sol-gel coating is the most suitable for endothelial cell growth. For this reason, HUVECs are cultured over the three different coated channels following the protocol of Rodiño et al. [19]. As in previous cultures, cells are stained with calcein to analyse their viability. PDMS channels are immersed in endothelial growth medium for 30 minutes to enhance cell adhesion and then cells are seeded over the channels at a concentration of 10^6 cells/ml. They are incubated for one day at standard incubation conditions (37 ºC temperature, 80% humidity and 5% CO_2). After this time, channels are washed with medium in order to remove the cells that are not adhered to the surface. The samples

are observed under fluorescence microscopy and the results are shown in Figure 4.8.

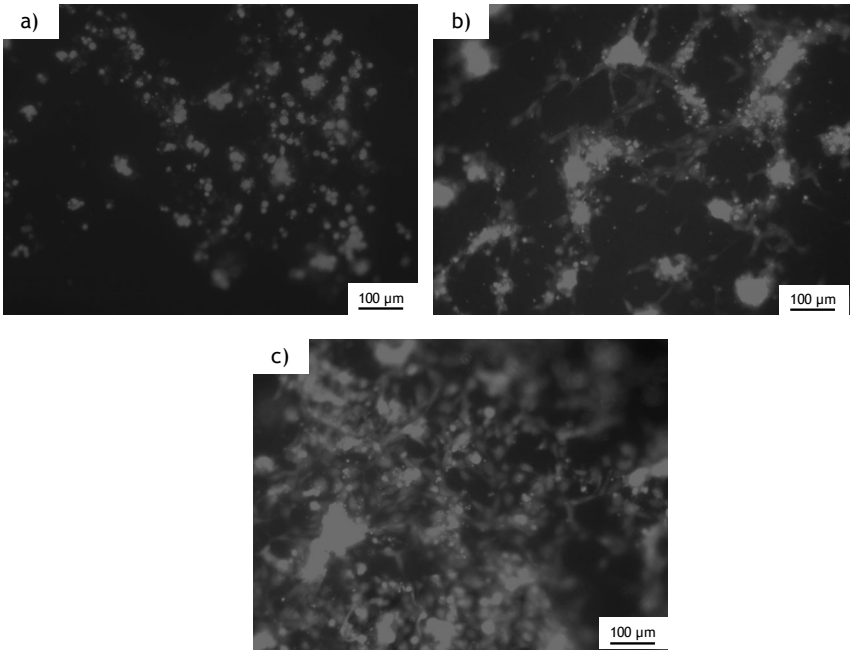

Figure 4.8: Representative fluorescence microscopy images of the HUVECs over PDMS channels with sol-gel coating of composition a) 60MTES/40TEOS, b) 70MTES/30TISP and c) 80MTES/20TISP, after one-day culture.

As it is shown in Figure 4.8, HUVECs grow over the three different coatings, since they emit fluorescent signal derived from calcein dye. Therefore, it can be determined that the sol-gel compositions employed in this work are all biocompatible. Nevertheless, significant differences in the growth and spread of the cells are observed between coatings [31]. Clearly, it can be seen in Figure 4.8.c, the 80MTES/20TISP sol-gel composition presents the most suitable environment for the growth and adherence of the HUVECs. Higher proliferation of cells compared with the other channels is observed. Moreover, they are more spread, tempting to form a monolayer of cells. On the other hand, 60MTES/40TEOS coating, shown in Figure 4.8.a, presents the most hostile medium for

HUVEC adhesion. Despite they are alive, cells do not spread over the surface and their morphology suggests a weak anchoring to the surface. 70MTES/30TISP coating, depicted in Figure 4.8.b, presents an intermediate situation, where some of the endothelial cells are attached and spread over the channel, but not as in the situation of the 80MTES/20TISP. In summary, despite showing that endothelial cells live over the three coatings, we can say that the 80MTES/20TISP sol-gel coating is the most appropriate composition of the three when working with HUVEC due to the stretched form of the cells and their attempt to form a monolayer, which indicates that cells are well attached to the surface. We can see in Figure 4.8 that even after washing the cell cultures with medium, there are still some remaining clusters of cells that attach to other cells instead to adhere to the surface of the material, generating an excess of fluorescent signal in the image. Experiments are carried several times in order to verify the result, washing the device with ethanol between usages.

Note that this experiment was performed with endothelial cells because a blood vessel like system was manufactured, but it has already been mentioned that the behaviour of the cells over a substrate depends on the kind of cultured cells, so a different cell line can grow on a different way over these coatings. This work is a first approach to the study of the biocompatibility of different sol-gel coatings and these results could vary as function of the kind of cell culture used. In the future, this study could be performed using different sorts of cells in order to establish the most suitable composition of the sol-gel coating for each cell type culture. This could provide medical and biological researchers the chance to choose the best sol-gel coating for their biological assays.

4.3. DETERMINATION OF LOW VELOCITY AREAS IN CORONARY BIFURCATIONS

The applications of preclinical devices, such as the fabricated in this work chapter, are numerous. As it was demonstrated, the chips can be functionalized with endothelial cells to perform in vitro

bioassays. In this way, cardiovascular environment can be simulated to study related pathologies in controlled laboratory conditions. Besides cell response, fluid dynamics can also be analysed. Hemodynamic factors regulate numerous aspects of vascular biology and physiology. They play a key role in vascular homeostasis and, as consequence, in the development of vascular problems like atherosclerosis, aneurysm or stenosis, which as it was mentioned, are leading cause of death in humans [32]. Therefore, the study of blood dynamics is crucial in order to unveil mechanism underlying these pathologies. Despite the fact that the entire arterial tree is exposed to systemic risk factors, it has been reported that atherosclerotic plaques are more prone to develop in geometrically predisposed areas, such as the vicinity of branch points, outer walls of bifurcations or inner walls of curvature. In this areas, shear stress and flow velocity are low and flow is turbulent or oscillating [33-35]. Endothelial shear stress, which is the frictional force per area exerted at the wall of the vessel by the bloodstream, is the most recognized force that plays a determinant role in plaque formation [36, 37]. For example, in coronary bifurcations the velocity profile changes when flow separates. At this point, flow detaches from the walls and normal blood dynamics is altered [38], particularly in the outer walls of branches. The analysis of fluid in these bifurcations would facilitate a more precise and clinically relevant study of geometry and shear stress in artery bifurcations, leading to better clinical results. It is not clear if hemodynamic parameters are themselves the cause of vascular disease, but they play a significant role in lesion development [39].

For analysing these conflictive areas, there have been reported several computational studies of fluid dynamics in blood vessels [40-41]. Nevertheless, these theoretical results should be experimentally validated. While in vivo studies are only possible in certain situations due to the practical and ethical limitations they present, in vitro experiments are a suitable method for carrying out numerical validations. In particular, the manufactured devices that imitate coronary bifurcations can be employed for this purpose. By performing flux assays in these channels, these conflictive low

velocity areas can be experimentally determined in different channel configurations with several bifurcation angles. In this section, these areas are determined by perfusing a coloured solution through the channel and treating the images recorded from the process. This experience is repeated for six different bifurcation angles, from 25º to 140º, and anomalies in normal flow are identified. In these low velocity areas flow remains during larger periods of time and therefore, low shear stress at the endothelium could actually make this zones more prone to disease.

4.3.1. Experimental validation of low velocity areas

For this purpose, PDMS channels with semi-circular profile (half-channel) are fabricated to facilitate visualization following the protocol described in Chapter 3. In particular, six structures are manufactured with different bifurcation angles. The main branch divides into two arms of same diameter that define the next angles: 25º, 45º, 60º, 90º, 120º and 140º. Channels have a radius of 1 mm. Figure 4.9 shows a general scheme of the bifurcation structure and the region of study.

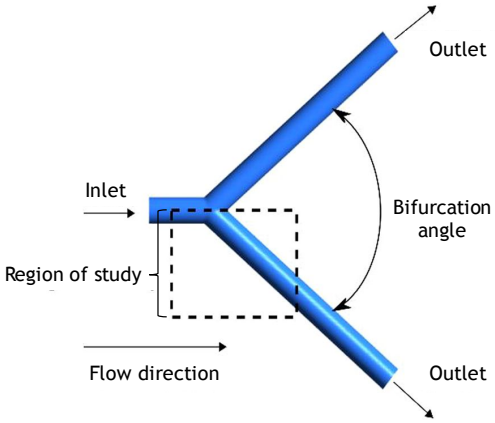

Figure 4.9: Scheme of the bifurcation of a vessel into two identical branches.

As it can be seen in Figure 4.9, the region of study is focused on the outer walls of the branches, just after the bifurcation of the main channel into the secondary ones because of velocity anomalies in this area [35]. Once the device is manufactured, it is incorporated to the experimental setup for the determination of low velocity areas. Two liquids are perfused through the channels. A sucrose solution is constantly circulated through the device with a peristaltic pump at a flow rate of 27 ml/min. Sucrose, at a concentration of 35%, has viscosity and density values similar to the blood ones. In particular, blood has a density of 1.060 g/cm^3 and viscosity of 4 mPa·s. For sucrose solution, density takes a value of 1.127 g/cm^3 and viscosity of 4.16 mPa·s. Since images obtained under these conditions are transparent, the areas cannot be determined only with this solution. In order to signal the velocities in the flow, another solution is injected during 10 seconds at a flow rate of 2.5 ml/min. It contains ferroin colorant that gradually changes the colour of the solution to a homogeneous red. The two outputs of the device are let open at atmospheric pressure. The device is illuminated from below with a LED and a CCD camera records the images from above. A scheme of the describer setup is shown in Figure 4.10.

The evolution of ferroin injection in the channel is recorded. When ferroin is charged into the channel, the colour gradually changes from clear to dark, reaching a situation where the channel is fully red and intensity in the camera decreases. After that, colorant starts to clear out and intensity in the camera increases until initial values when only sucrose was presented. In order to determine the different velocity profile in the channel, only images corresponded to the discharge of ferroin are selected. For this purpose, the evolution of average intensity in each frame with the time is plotted. An example of this graph is depicted in Figure 4.11.

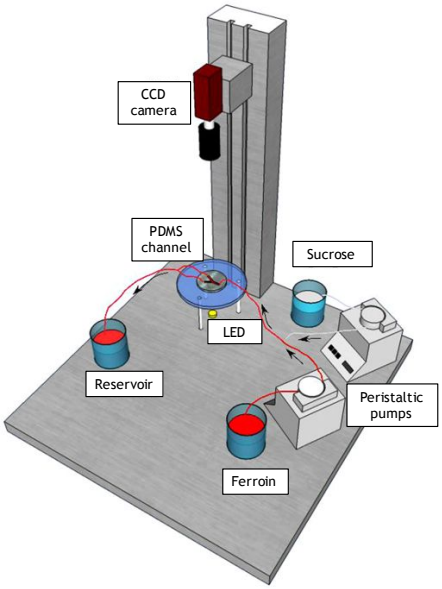

Figure 4.10: Scheme of the experimental setup for the determination of low velocity areas in bifurcations.

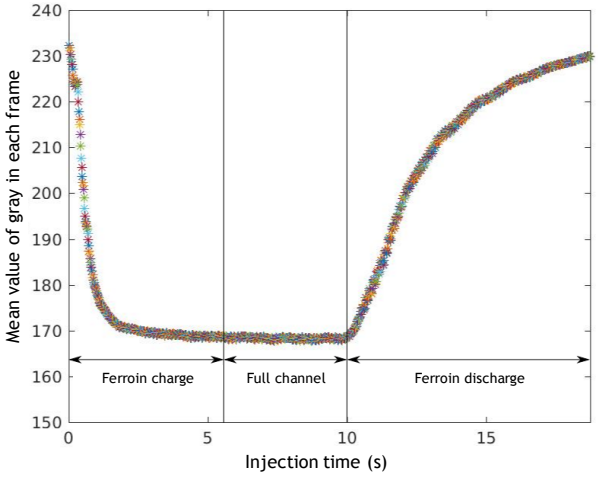

Figure 4.11: Evolution of the ferroin colorant in the region of study of the PDMS channel. The evolution of mean value of grey in each frame is considered within time for selecting the frames to analyse.

All images presented in the "ferroin discharge" zone are added pixel by pixel and average intensity is calculated in every point. This returns into an image in colour code, where blue tones correspond to darker areas and warm tones to the lighter ones. In areas where velocity value is low, it takes more time to clear off the ferroin during the discharge and therefore, the final value after the operation is darker (blue tones) than in other areas. An example of the results of this analysis, for the bifurcation angle of 25º, is shown in Figure 4.12.

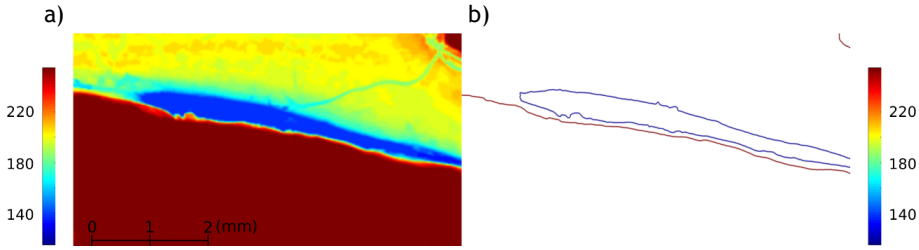

Figure 4.12: a) Representative image of the spatial distribution of ferroin in the PDMS channel with bifurcation angle of 25 °. Colour code indicates average value of grey after summing all frames, so blue tones indicates dark areas and red tones, the bright ones. b) Representation of wall contour in red and 160 grey contour in blue. The area inside the blue line corresponds to the low velocity area of this geometry.

Each experiment is carried out for five times and it is performed for the six different bifurcation angles. In this way, the low velocity areas, where anomalies of flux occur, can be characterised and measured regarding the total observation area. These results will be compared to the ones offered from the numerical simulation in next subsections.

4.3.2. Numerical simulation of low velocity areas

A coronary bifurcation is simulated considering an idealization of the left main coronary artery that separates into the left circumflex and the left anterior descending arteries. The control parameter is the bifurcation angle. Star-CCM+ software [42] is employed to design the geometries, convert these geometries into a grid and carry out

numerical simulations solving the fluid-dynamics equations using finite volume method. Blood dynamics is simulated by the three-dimensional incompressible Navier-Stokes equations. Reynolds number smaller than 200 is considered for each geometry thus laminar flow is ensured. Moreover, blood is considered as a Newtonian fluid with no-slip condition at the vessel rigid walls, meaning that the fluid have zero velocity relative to the boundary. In order to solve the Navier-Stokes equations, a 3D mesh is designed taking into account that low velocity areas are located close to the outer bifurcation vessel walls. The mesh is composed of tetrahedral prisms, being more accurate near the walls with hexahedral layers in order to study the low velocity zones with more precision. Grid has 144269 elements. The computations run until a steady state is reached.

Eight different configurations of Y-junction vessels are studied, with bifurcation angles from 25° to 180°. For the simulations, an inlet velocity condition consisting in a flat profile of 0.2 m/s [43] is considered in the main vessel. The density and viscosity of the circulating fluid is identical to the values of blood in human circulatory system. With these parameters, the obtained Reynolds number is similar to the one that results from the experimental setup, with the corresponding values of density and viscosity, ensuring a non-turbulent regime. Atmospheric pressure is set in the outlet of both branching vessels, as in the experimental setup. All geometries have identical diameter of 2 mm. In order to study the low velocity zones it is necessary to establish a velocity value below which a given zone is considered as a low velocity area. Zones with velocity values less than a 10% of the maximum velocity recorded are considered low velocity areas. Each simulation provides a complete spatial description of the flow velocities. The results are shown in the next subsection, together with the experimental ones. Numerical simulations were carried out in collaboration project with researchers working on the project MAT2015-71119-R.

4.3.3. Comparison of experimental and numerical results

A comparison of results derived from the experiments with PDMS channels and numerical simulations is shown in Figure 4.13. In particular, the analysis for bifurcation angles of 120º (Figure 4.13.a), 90º (Figure 4.13.b) and 25º (Figure 4.13.c) is depicted to shown three differentiated behaviours of flux regarding the geometry. Left column shows, colour coded, the spatial distribution of the ferroin solution during the discharge period for the three different bifurcation angles. Dark blue areas correspond to a higher concentration of colorant and relates with lower values of flow velocity and, thus, with regions where potentially pathological particles are more likely to deposit. Areas in red correspond with the extra vessel space, which has the higher intensity value when the image is recorded. The liquid always flows from left to right and only the lower branch after the bifurcation is presented since the other exhibits the symmetrical behaviour. As expected, the regions with lowest flow velocities are always located next to the external wall of the bifurcation. The corresponding numerical simulations are plotted in the right column. Colour code, in this case, represents the velocity values of flux in the vessel. Therefore, blue and red tones correspond to low and high velocity, respectively.

As it can be seen in Figure 4.13, similar results regarding the location of low velocity areas are obtained from experiments and simulations. As expected, these zones appear in the outer walls of daughter branches after flux separation. Clearly, the largest region in dark blue happens for the intermediate angle of 90° [44]. In Figure 4.14, the percentage of low velocity area regarding the total one is plotted for more geometries that are not so easy to visually analyse with the experimental design (45º, 60º and 140º). Low velocity area is plotted versus the bifurcation angle and each value is averaged over five realizations. The graph is compared with numerical results of eight vessel geometries with different bifurcation angles.

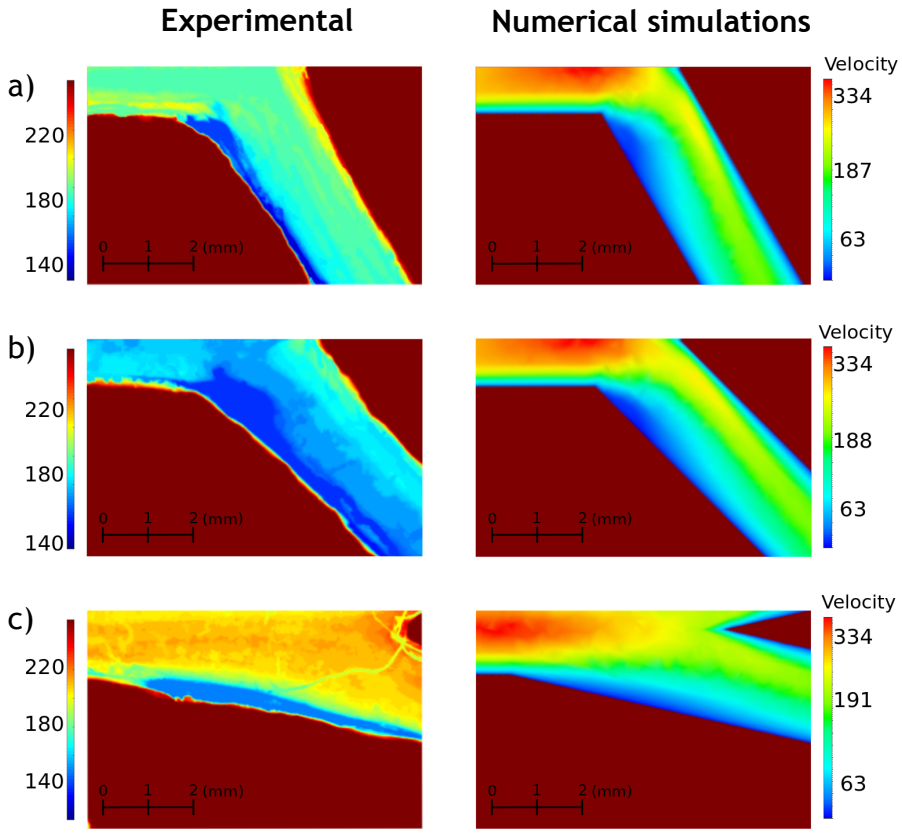

Figure 4.13: Comparison between experimental and numerical simulation results for three different bifurcation angles: a) 120°, b) 90° and c) 25°. First column presents, colour coded, the distribution of the low velocity flow areas in the channel. Second column shows the flow velocity magnitude.

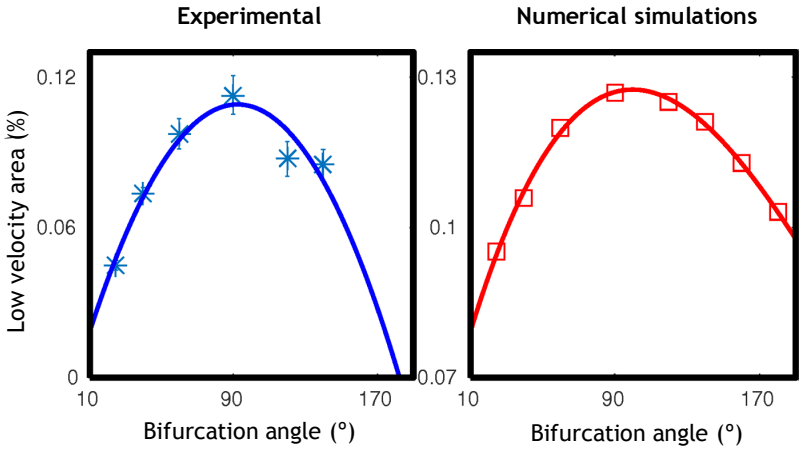

Figure 4.14: Comparison of the size of low velocity areas regarding the total observation area. The experiment was carried out for six different bifurcation angles in the experimental setups and eight in the numerical simulations.

As it was also shown in Figure 4.13, in Figure 4.14 it can be discerned that there is a value of the angle, around 90°, for which the region of low flow velocity reaches a maximum. The region where the flow slows down is significantly larger for this critical angle and therefore, the possibilities of vascular diseases derived from anomalous flow are higher than in other configurations. Moreover, these zones where flux stays more time could increase the probability of a pathogen particle to stablish a connection with the vessel wall and adhere, such as a circulating tumour cell that eventually could cross the endothelium and cause metastasis. Note that actual values of the low velocity areas are not the same for the experimental and numerical cases. This is due to the different methods used to determine these areas as described in the methods section. Also, numerical study of the problem indicated that increasing the inflow velocity is shown to shift the critical angle range into smaller values and more acute angles.

In some studies, the incidence of the bifurcation angle in plaque formation has been studied in in vitro models, reaching very similar conclusions [45]. However, although a wide consensus is found on the location of low velocity areas in the outer walls of the bifurcation, the

effect of the bifurcation angle is still unclear [46, 47]. Our experiment, that combines numerical simulations and experimental results, determines that angles around 90º exhibit a larger low velocity area and vascular disease will be more prone to appear in those zones. Of course, the experiences can be enhanced in the future by using pulsatile flow and deformable walls, both theoretically and experimentally, but these results are presented as a first approach to the problem that offers concordant findings. Moreover, biological assays could be performed to measure the impact of flow anomalies in endothelial cells, since it was demonstrated that can attach the PDMS device. Flux conditions in bioassays (10 ml/min), combined with viscosity and density of culture medium, leads to similar Reynolds numbers as the ones in these experiments. Also, pumping tumour cells through the channel and observing where they deposit could be a further step in this research line.

4.4. CONCLUSIONS

In this section, the applicability of the PDMS channels previously fabricated were shown. The device was biologically validated by culturing HUVEC cells in the totality of the inner walls. In this way, a functional model of a channel that imitates a blood vessel was obtained. The impact of the roughness of the devices in cell attachment was studied, since it is crucial for the proper development of flux bioassays. Endothelial cells were cultured over channels with different arithmetical average roughness values of the profile, obtained from thermal treatments of the soda-lime master at 590 ºC, 630 ºC and 670 ºC, as well as from the original master without any treatment. They corresponded to values of R_a of 1528.01±100.01 nm, 400.84±20.31 nm, 27.18±4.52 nm and 5285.01±304.56 nm respectively. It was found that cells grew and attached to all these devices, but significant differences were found when flux was perfused through the device. In masters with lower roughness values cells detached and do not remain in the channel walls. The device manufactured from the master with a treatment at 590 ºC and R_a=1528.01±100.01 nm was the one that avoided cell detachment

when performing flux experiments and also slightly reduced the roughness value in comparison with the original master helping in microscopy inspections.

The degradation problem of PDMS in contact with some organic solvents, commonly employed in bioassays and that led to anomalous cell growth, was overcame by coating the channels by using different sol-gel compositions (60MTES/40TEOS, 70MTES/30TISP and 80MTES/20TISP). They were coated by dip-coating technique and endothelial cells were seeded over them in order to evaluate their biocompatibility. By means of fluorescence microscopy, it was observed that all sol-gel coatings allow cells to live, but with important differences between them. Despite showing that all compositions are biocompatible, the 80MTES/20TISP sol-gel coating was the most appropriate composition when working with HUVECs due to the stretched form of the cells and their attempt to form a monolayer, which indicated that cells were well attached to the surface.

Finally, the devices were employed for experimentally verifying the presence of low velocity areas in the outer walls of the bifurcations, as well as their dependence with the bifurcation angle. Angles from 25º to 140º were tested in order to characterise the flow in these conflictive zones in a non-intrusive way. It was found that angles around 90º showed the larger areas where flow was anomalous, leading to possible vascular diseases and cell deposition. These results were validated with numerical simulations that found the same results as the experimental ones.

REFERENCES

[1] A. Hasan, A. Paul, A. Memic, and A. Khademhosseini, "A multilayered microfluidic blood vessel-like structure," *Biomed. Microdev.*, vol. 17, no. 5, pp. 88, 1-13 , 2015.

[2] C. A. Wilkens, C. J. Rivet, T. L. Akentjew, J. Alverio, M. Khoury, and J. P. Acevedo "Layer-by-layer approach for a uniformed fabrication of a cell patterned vessel-like construct," *Biofabrication,* vol. 9, pp. 015001, 1-17, 2017.

[3] Y. Zheng, J. Chen, M. Craven, N. Won, S. Totorica, A. Diaz-Santana, P. Kermani, P. B. Hempstead, C. Fishbach-Tesche, J. A. López, and A.D. Strook "In vitro microvessels for the study of angiogenesis and thrombosis," *PNAS,* vol. 109, no. 24, pp. 9342-9347, 2012.

[4] J. Ribas,H. Sadeghi, A. Manbachi, J. Leijten, K. Brinegar, Y. S. Zhang, L. Ferreira, and A. Khademhosseini, "Cardiovascular organ-on-a-chip platforms for frug discovery and development," *Appl. in vitro Toxicol.,* vol. 2, no. 2, pp. 82–96, 2016.

[5] D. Huh, G. A. Hamilton, and D. E. Ingber, "From 3D cell culture to organs-on-chips," Trends Cell Biol., vol. 21, no. 12, pp. 745–754, 2011.

[6] S. Kim, H. Lee, M. Chung, and N. L. Jeon, "Engineering of functional, perfusable 3D microvascular network on a chip," *Lab Chip*, vol.13, no. 8, pp. 1489–1500, 2013.

[7] S. H. Lee, "Microtechnology for fabricate lab-on-a-chip for biology applications," in *Lab on a chip technology. Volume 1: Fabrication and microfluidics,* K. H. Herold and A. Rasooly, Eds. Norfolk: Caister Academic Press, 2009, pp. 125-138.

[8] A. S. Hoffman, "Hydrogels for biomedical applications," *Adv. Drug Deliv. Rev*., vol. 64, pp. 18–23, 2012.

[9] A. Hasan, R. Walters, B. Roula, R. Dana, S. Yara, T. Alexandre, and A. Paul, "Engineered biomaterials to enhance stem cell-based cardiac tissue engineering and therapy," *Macromol. Biosci.,* vol. 16, no.7, pp. 958–977, 2016.

[10] Q. Smith and S. Gerecht, "Going with the flow: microfluidic platforms in vascular tissue engineering," *Curr. Opin. Chem. Eng*., vol. 3, pp. 42–50, 2014.

[11] S. Gonçalves, A. Leirós, T. van Kooten, F. Dourado, and L. R. Rodriguesa, "Physicochemical and biological evaluation of poly(ethylene glycol) methacrylate grafted onto poly(dimethyl siloxane) surfaces for prosthetic devices," *Colloids Surf.,* vol. 109, pp. 228-235, 2013.

[12] H. Aubin, J. W. Nichol, C. B. Hutson, H. Bae, A. L. Sieminski, D. M. Cropek, P. Akhyari, and A. Khademhosseini, "Biomaterials Directed 3D cell alignment and elongation in microengineered hydrogels," *Biomaterials*, vol. 31, no. 27, pp. 6941–6951, 2010.

[13] K. Yue, G. Trujillo-de Santiago, M. M. Álvarez, A. Tamayol, N. Annabi, and A. Khademhosseini, "Biomaterials Synthesis, properties, and biomedical applications of gelatin methacryloyl (GelMA) hydrogels," *Biomaterials,* vol. 73, pp. 254–271, 2015.

[14] C. Xu, F. Yang, S. Wang, and S. Ramakrishna, "In vitro study of human vascular endothelial cell function on materials with various surface roughness," *J. Biomed. Mat. Res.,* vol. 71, no. 1, pp. 154-161, 2004.

[15] A. M. Ross, Z. Jiang, M. Bastmeyer, and J. Lahann, "Physical aspects of cell culture substrates: Topography, roughness, and elasticity," *Small*, vol. 8, no. 3, pp. 336–355, 2012.

[16] S. P. Khan, G. G. Auner, and G. M. Newaz, "Influence of nanoscale surface roughness on neural cell attachment on silicon," *Nanomedicin: NBM,* vol. 1, no. 2, pp. 125–129, 2005.

[17] D. D. Deligianni, N. D. Katsala, P. G. Koutsoukos, and Y. F. Missirlis, "Effect of surface roughness of hydroxyapatite on human bone marrow cell adhesion, proliferation, differentiation and detachment strength," *Biomaterials,* vol. 22, no. 1, pp. 87–96, 2001.

[18] M. Lampin, R. Warocquier-Clerout, C. Legris, M. Degrange, and M. F. Sigout-Luizard, "Correlation between substratum roughness and wettability, cell adhesion, and cell migration," *J. Biomed. Mat. Res.,* vol. 36, no. 1, pp. 99-108, 1996.

[19] B. K. Rodiño-Janeiro, M. González-Peteiro, R. Ucieda-Somoza, J. R. González-Juanatey, and E. Álvarez, "Glycated albumin, a precursor of advanced glycation end-products, up-regulates NADPH oxidase and enhances oxidative stress in human endothelial cells: molecular correlate of diabetic vasculopathy," *Diabetes Metab. Res. Rev.,* vol. 26, no. 7, pp. 550-558, 2010.

[20] E. Leclerc, Y. Sakai, and T. Fujii, "Cell culture in 3-dimensional micro fuidic Structure of PDMS," *Biomed. Microdev.*, vol. 5, no. 2, pp. 109–114, 2003.

[21] M. Aymerich, E. Álvarez, C. Bao-Varela, I. Moscoso, J. R. González-Juanatey, and M. T. Flores-Arias, "Laser technique for the fabrication of blood vessels-like models for preclinical studies of pathologies under flow conditions," *Biofabrication*, vol. 9, no. 2, pp. 025033, 1-7, 2017.

[22] T. Chung, D. Liu, S. Wang, and S. Wang, "Enhancement of the growth of human endothelial cells by surface roughness at nanometer scale," *Biomaterials*, vol. 24, no. 25, pp. 4655–4661, 2003.

[23] B. I. T. Gabe, J. H. Gault, J. Ross, D. T. Mason, C. J. Millis, J. P. Schillingford, and E. Braunwald, "Measurement of instantaneous blood flow velocity and pressure in conscious man with a catheter-tip velocity probe," *Circulation,* vol. 40, no. 5, pp. 603-614, 1969.

[24] G. T. Roman and C. T. Culbertson, "Surface engineering of poly(dimethylsiloxane) microfluidic devices using transition metal sol-gel chemistry," *Langmuir*, vol. 22, no. 9, pp. 4445–4451, 2006

[25] A. R. Abate, D. Lee, T. Do, C. Holtze, and D. a Weitz, "Glass coating for PDMS microfluidic channels by sol-gel methods," *Lab Chip*, vol. 8, no. 4, pp. 516–518, 2008.

[26] J. N. Lee, C. Park, and G. M. Whitesides, "Solvent compatibility of poly(dimethylsiloxane)-based microfluidic devices," *Anal. Chem.,* vol. 75, no. 23, pp. 6544-6554, 2003.

[27] J. P. Rolland, R. M. Van Dam, D. A. Schorzman, S. R. Quake, and J. M. DeSimone "Solvent-resistant photocurable "liquid teflon" for microfluidic device fabrication," *J. Am. Chem. Soc.,* vol. 126, no. 8, pp. 2322-2323, 2004.

[28] G. T. Roman, T. Hlaus, K. J. Bass, T. G. Seelhammer, and C. T. Culbertson, "Sol-gel modified poly(dimethylsiloxane) microfluidic devices with high electroosmotic mobilities and hydrophilic channel wall characteristics," *Anal. Chem*., vol. 77, no. 5, pp. 1414–1422, 2005.

[29] R. Gomez-Sjoberg, A. a. Leyrat, B. T. Houseman, K. Shokat, and S. R. Quake, "Biocompatibility and reduced drug absorption of sol-gel-treated poly(dimethyl siloxane) for microfluidic cell culture applications," *Anal. Chem.*, vol. 82, no. 21, pp. 8954–8960, 2010.

[30] C. J. Brinker and G. W. Scherer, *Sol-Gel Science: The Physics and Chemistry of Sol-Gel Processing*. San Diego: Academic Press, Inc., 1990.

[31] M. Aymerich, A. I. Gómez-Varela, E. Álvarez, and M. T. Flores-Arias, "Study of different sol-gel coatings to enhance the lifetime of PDMS devices: evaluation of their biocompatibility," *Materials*, vol. 9, no. 9, pp. 728, 1-11, 2016.

[32] C. J. L. Murray et al., "Global, regional, and national life expectancy, all-cause mortality and cause-specific mortality for 249 causes of death, 1980–2015: a systematic analysis for the Global Burden of Disease Study 2015," *The Lancet,* vol. 388, no. 10053, pp. 1459–1544, 2016.

[33] C. Oviedo et al., "Intravascular ultrasound classification of plaque distribution in left main coronary artery bifurcations where is the plaque really located?," *Circ. Cardiovasc. Interv.,* vol. 3, no. 2, pp. 105-112, 2010.

[34] P. Eshtehardi, M. C. McDaniel, J. Suo, S. S. Dhawan, L. H. Timmins, J. N. G. Binongo, L. J. Golub, M. T. Corban, A. V. Finn, J. N. Oshinski, A. A. Quyyumi, D. P. Giddens, and Habib Samady, "Association of coronary wall shear stress with atherosclerotic," *J. Amer. Heart Association,* vol. 1, no. 4, pp. e0025431- e0025439, 2012.

[35] T. Asakura and T. Karino, "Flow patterns and spatial distribution of atherosclerotic lesions in human coronary arteries," *Circ. Res.,* vol. 66, no. 4, pp. 1045–1066, 1990.

[36] R. Vergallo, M. I. Papafaklis, T. Yonetsu, C. V. Bourantas, I. Andreou, Z. Wang, J. G. Fujimoto, I. McNulty, H. Lee, L. M. Biasucci, F. Crea, C. L. Feldman, L. K. Michalis, P. H. Stone, and I. K. Jang, "Endothelial shear stress and coronary plaque characteristics in humans," *Circ. Cardiovasc. Imaging,* vol. 7, no. 6, pp. 905–911, 2014.

[37] K. C. Koskinas, C. L. Feldman, Y. S. Chatzizisis, A. U. Coskun, M. Jonas, C. Maynard, A. B. Baker, M. I. Papafaklis, E. R. Edelman, and P. H. Stone, "Natural history of experimental coronary atherosclerosis and vascular remodelling in Relation to endothelial shear stress a serial, in vivo intravascular ultrasound study," *Circulation,* vol. 121, no. 19, pp. 2092-2102, 2010.

[38] U. Morbiducci, A. M. Kok, B. R. Kwak, P. H. Stone, D. A. Steinman, and J. J. Wentzel, "Atherosclerosis at arterial bifurcations: evidence for the role of haemodynamics and geometry," *Thromb. Haemost.,* vol. 115, no. 3, pp. 482-492, 2016.

[39] P. A. Vanderlaan, C. A. Reardon, G. S. Getz, P. A. Vanderlaan, C. A. Reardon, and G. S. Getz, "Site specificity of atherosclerosis site-selective responses to atherosclerotic modulators," *Arterioscler. Thromb. Vasc. Biol.,* vol. 24, no. 1, pp. 12–22, 2004.

[40] J. Dong, Z. Sun, K. Inthavong, and J. Tu, "Fluid–structure interaction analysis of the left coronary artery with variable angulation," *Comp. Meth. Biomech. Biomed. Eng.,* vol. 18, no. 14, pp 1500-1508, 2015.

[41] S. E. Razavi, A. A. Omidi, and M. S. Zanjani, "Numerical investigation of blood flow in a deformable coronary bifurcation and non-planar branch," *Bioimpacts,* vol. 4, no. 4, pp. 199–204, 2014.

[42] https://mdx.plm.automation.siemens.com/star-ccm-plus

[43] K. J. Chodzyński, K. Z. Boudjeltia, J. Lalmand, A. Aminian, L. Vanhamme, D. Ribeiro de Sousa, S. Gremmo, L. Bricteux, C. Renotte, G. Courbebaisse, and G. Coussement, "An in vitro test bench reproducing coronary blood flow signals," *Biomed. Eng*., vol. 4, no. 77, pp. 1–26, 2015.

[44] A. Otero-Cacho, M. Aymerich, M. T. Flores-Arias, M. Abal, E. Álvarez, V. Pérez-Muñuzuri, and A. P. Muñuzuri, "Determination of

hemodynamic risk for vascular disease in planar artery bifurcations," *Sci. Rep.*, vol. 8, no. 1, pp. 2795, 1-7, 2018.

[45] Y. Zhang, N. V. Menon, C. Li, V. Chan, and Y. Kang, "The role of bifurcation angles on collective smooth muscle cell biomechanics and the implication in atherosclerosis development," *Biomater. Sci.,* vol. 4, no. 3, pp. 430-438, 2015.

[46] C. Chiastra, D. Gallo, P. Tasio, F. Iannaccone, F. Migliavacca, J. J. Wentzel, and U. Morbiducci, "Healthy and diseased coronary bifurcation geometries influence near- wall and intravascular flow: A computational exploration of the hemodynamic risk," *J. Biomech*., vol. 58, pp. 79–88, 2017.

[47] T. Chaichana, Z. Sun, and J. Jewkes, "Computation of hemodynamics in the left coronary artery with variable angulations," *J. Biomech*., vol. 44, no. 10, pp. 1869–1878, 2011.

5. OTHER APPLICATIONS OF LASER STRUCTURING IN BIOMEDICINE

In the previous chapters, this thesis was mainly devoted to the fabrication of channels by laser ablation for developing organ-on-a-chip and microfluidic devices. In particular, blood vessel-like models were created and biologically validated. Nevertheless, thanks to its versatility, numerous structures can be manufactured by laser technologies over different substrates. Also, since coronary bifurcation models were fabricated, the applications of the chips were primarily focused on cardiovascular field. However, the applications of laser multistructuring are presented in many other fields. In particular, in this chapter laser technologies will be employed for two different aims in biomedicine. The first one is to pattern biocompatible materials by Talbot effect for prosthesis applications. In this case, the foci of a microlens array is going to be used as object for the Talbot effect, for patterning titanium and tantalum, which are commonly used in the fabrication of prosthesis. The obtained structures will be employed as culture substrates for endothelial cells, studying the different cellular behaviour over them and analysing the impact of topography factors like growth and spreading. The second one is a chip for capturing circulating tumour cells (CTCs) that are presented in the bloodstream. In this case, a microfluidic device with a particular structure is fabricated by laser-induced plasma-assisted ablation on soda-lime glass. This chip is formed by microposts that will be functionalized with epithelial cell adhesion molecule (EpCAM) antibodies, which will enhance the effectiveness of the device. Trapping efficiency of the chip, as well as yield escape of CTCs, will be studied.

5.1. LASER SURFACE MICROSTRUCTURING OF BIOCOMPATIBLE MATERIALS USING A MICROLENS ARRAY AND THE TALBOT EFFECT

The surface modification of different materials is a widely-studied procedure in both industry and biomedicine due to the numerous applications it presents in these fields [1, 2]. Some industrial examples are the modification of tribological properties of substrates to alter wettability or friction parameters of materials [3, 4]. In the biomedical field, surface modification has applications in tissue engineering [5], prosthesis research [6] or biosensing [7], among others. As it was already commented and shown through this thesis, it has been reported that aspects like roughness [8] or elasticity [9] of the substrate has a direct impact in cell growth and attachment to the surfaces, having different responses depending on the type of cell and culture material. Other determinant physical factor in cell behaviour is the topography of the substrate [10, 11] that can be modified in order to enhance cell proliferation and anchoring. In particular, tantalum and titanium are two of the most employed elements in biomedicine due to their numerous applications in orthopaedics and cardiovascular implants [12-14]. Proper cell attachment is key factor for the success of these prostheses and there exist plenty of works that show that the surface modification in the micron scale of these materials leads to a higher cell adhesion [15-18].

As it was presented in Chapter 1, there are numerous techniques for structuring materials, but laser technologies is presented as an excellent option thanks to the versatility of the technique, process speed, accuracy and non-contact nature. In particular, femtosecond lasers have been employed for the surface microstructuring of titanium plates, improving the biocompatibility of the material [19]. Moreover, the use of the foci of a microlens array in combination with laser technologies was shown efficient for multistructuring surfaces by laser direct writing [20]. Materials like stainless steel, coper, polymers or aluminium can be micropatterned by placing the material at the focal length of the array. The microlens array is illuminated by the laser beam and the energy is concentrated in each focus of the array,

leading to a very effective process of microstructuring. Therefore, microlenses are presented as a well-suited element for improving the efficiency of laser texturing technique and the cost of the process [21]. Nevertheless, it was shown that this procedure leads to a rapid deterioration of the matrix of microlenses since expelled material from the target reach the array due to their short focal distance [22]. The structure is irreversibly damaged and the useful life of microlenses results drastically reduced. One solution to overcome this problem is to employ the Talbot effect using one the self-images as patterns to multistructure the substrate. In this way, the distance between the array and the target is increased. Talbot effect consists in the repetition of the complex amplitude distribution of a periodic object along the light propagation axis when it is illuminated by a coherent beam, such a laser [23]. In this situation, the foci of the microlenses can be considered as the periodic object that repeats its image at several integer distances from the array. These Talbot image distances depend on the wavelength of the beam, the kind of illumination employed and the period of the object. Moreover, the images can appear at a fractional value of the Talbot distance and with a minor period from the original, which is proportional to a fraction, called fractional Talbot effect [24]. The capability of microstructure different substrates using the Talbot effect and laser irradiation has been studied some years ago [22,25,26]. In this section, biocompatible materials, such as titanium and tantalum, will be surface microstructured by direct laser writing using the foci of an array of microlenses and the integer and fractional Talbot effect to avoid the deterioration of the array and to obtain patterns with a minor period. Once surfaces are patterned, cell adhesion over the biocompatible substrates will be studied in order to determine the effect of the structuring in the cell behaviour as well as the impact of the topography.

5.1.1. Laser structuring of titanium and tantalum

In this subsection, a method for microstructuring the surfaces of biocompatible materials by a costless and effective hybrid method is presented. It is composed by a direct laser writing technique using a

microlens array and the Talbot effect or self-image phenomenon. First, a brief introduction to the integer and fractional Talbot effect is presented. Then, before ablating the substrates, an experimental validation of the Talbot distances is carried out. Once the positions are verified, the structuring of tantalum and titanium is performed.

5.1.1.1. Integer and fractional Talbot effect

The Talbot phenomenon is a diffraction effect that consists in the image repetition of a periodic object when it is illuminated by a coherent source of illumination, like a laser beam. The repetition of the image along the longitudinal axis of propagation of light occurs without the need of optical elements, such as lens or mirrors. It was demonstrated that not only periodic objects cause this phenomenon, the Talbot effect also occurs for objects that satisfy the called Montgomery conditions [27]. In particular, periodic objects, such as the foci of a microlens array, are the most employed subgroup of the Montgomery objects [28]. The Talbot distances depend on the wavelength of the beam, the periodicity of the object and the kind of illumination employed. When a plane wave is chosen as illumination front, the Talbot distances can be calculated by following [23]

$$z_T = n\frac{p^2}{\lambda} \tag{5.1}$$

where z_T is the distance between the periodic object and the complex amplitude distribution or Talbot image, n is a real number, p is the period of the object and λ is the wavelength of illumination. When the number n is an integer number (integer Talbot effect), the image of the periodic object is repeated at integer multiples of the Talbot distance and the period p_T matches the object one. When n is a fractional number (fractional Talbot effect) the replicas are found at fractional multiples of the integer distance and the period is proportional to the period of the object [29]. The expressions for fractional Talbot distances and periods are as follows

$$z_T = \frac{u}{v}\frac{p^2}{\lambda} \tag{5.2}$$

$$p_T = \frac{p}{v} \tag{5.3}$$

being u and v integer coprime numbers.

In this section, the foci of a microlens array is considered as the periodic object that repeats its complex amplitude distribution according to the integer and fractional Talbot effect. When a microlens array is employed to produce the Talbot effect, the value of the focal length of the array must be added to the Talbot distance in order to obtain the total distance between the object and the image [30]. This total distance is given by

$$z = f_{ML} + z_T \tag{5.4}$$

where f_{ML} is the focal length of the microlenses and z_T is the integer or fractional Talbot distance.

5.1.1.2. Experimental validation of the Talbot distances

Prior to the ablation of the substrates, the self-images of the foci of the microlenses are experimentally verified, checking its appearance in the positions predicted by the equations above presented. The Talbot planes where the foci show a more uniform irradiance profile are chosen for the further microstructuring of the substrates. The microlens array employed in this work has 90 μm period and 1.04±0.03 mm focal length, experimentally verified. These microlenses, made of fused silica, were fabricated by reactive-ion etching technique and have a diameter of 80 μm and a height of 3 μm. Figure 5.1 shows a 3D confocal image of the array.

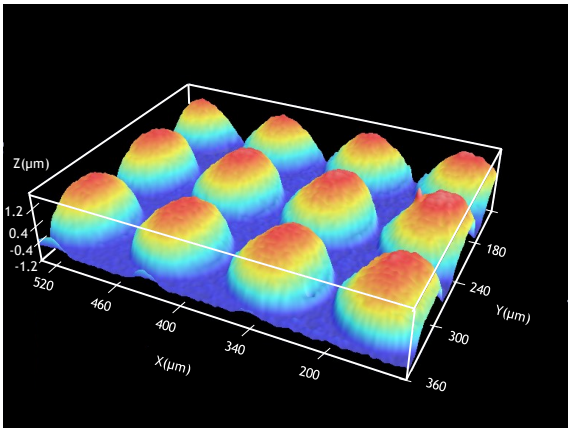

Figure 5.1: 3D confocal image of the microlens array with 90 μm of period.

Through this study, a Spectra Physics Quanta Ray Nd:YAG laser is employed. It was already presented in Chapter 2 but briefly, it works in its second harmonic (λ=532 nm) and has a nanosecond pulse duration and fixed repetition rate of 50 Hz. It can operate both in continuous wave and Q-switch mode. For the identification of the self-images it is employed in continuous wave operation mode. Since the divergence of the beam is negligible, the output of the laser is considered as a plane wave and equations previously presented can be applied. The acquisition system for the images consists of a CCD camera and a microscope objective. The objective is longitudinally moved along the propagation axis, forming the Talbot images. The CCD camera records the intensity distribution of each position. The setup for the identification of the Talbot planes is depicted in Figure 5.2.

In this work, the first Talbot distance and the fractional Talbot distances 3/2 and 5/3 are chosen. These images occur at theoretical positions of z_1=16.27 mm, $z_{3/2}$=23.89 mm and $z_{5/3}$=26.42 mm from the array, respectively. Figure 5.3 depicts the Talbot images recorded with the CCD camera. These images are found at experimental positions of z_1=16.21±0.01 mm, $z_{3/2}$=23.85±0.01 mm and $z_{5/3}$=26.42±0.01 mm

from the array. Therefore, theoretical positions are in good agreement with experimental measurements. It can be appreciated that the fractional plane that corresponds to the 5/3 Talbot image is less intense than the others. This is because the light is distributed between more points than in the other cases, resulting in less intense foci images than in the integer pattern. This fact will be also noticed in the ablation of titanium and tantalum substrates. Also, as it was expected, the period of fractional self-images decrease as occurs in fractional Talbot distances.

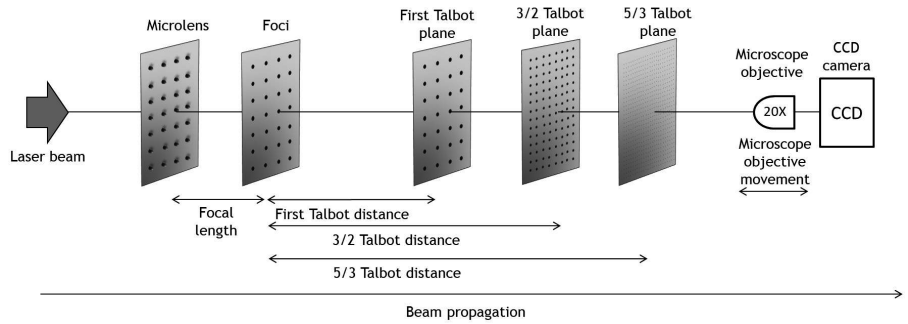

Figure 5.2: Experimental setup for the identification of the Talbot distances of the foci of a microlens array when it is illuminated by a Nd:YAG laser operating in continuous wave. The image acquisition system for recording the Talbot images is formed by a 20X microscope objective and a CCD camera.

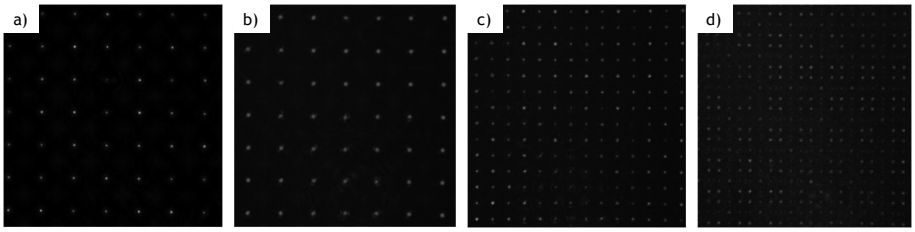

Figure 5.3: CCD images obtained from the setup depicted in Figure 5.3 of the a) foci of the microlenses, b) first Talbot plane, c) 3/2 Talbot plane and d) 5/3 Talbot plane. All images are in the same scale.

5.1.1.3. Titanium and tantalum ablation

Once Talbot images are selected and their positions are experimentally verified, we proceed to the ablation of biocompatible surfaces at these planes. The targets employed are one foil of titanium (99,6% purity) of 0.7 mm thickness and another of tantalum (99,9% purity) of 0.5 mm thickness, provided by Goodfellow. There are several studies that demonstrate the impact of surface roughness in cell behaviour [31-33], so before ablation the roughness of both materials is reduced to similar values by polishing the surface. In this way, the influence of initial roughness in cell growth and attachment is minimized. The samples are polished with a Logitech PM2A polisher. Figure 5.4 shows the change of tantalum surface after being polished.

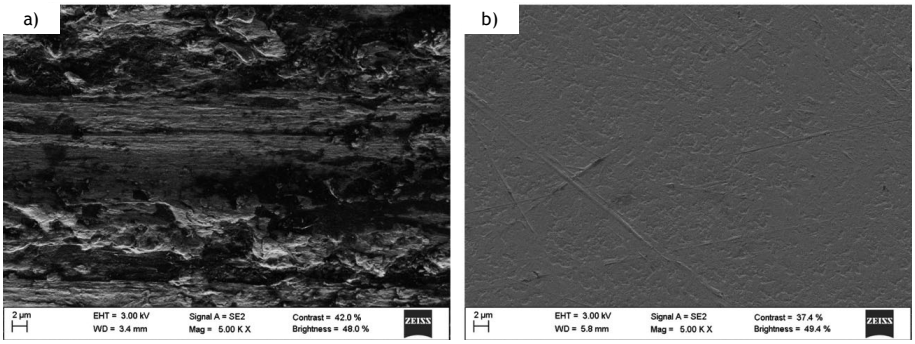

Figure 5.4: Illustrative SEM images of tantalum substrate a) before and b) after being polished. Average profile roughness value decreases from 565.71 nm to 7.81 nm.

The non-polished tantalum surface has an average profile roughness (R_a) of 565.71±62.76 nm and it decreases to a value of 7.81±0.91 nm. Titanium R_a is reduced from 639.42±33.87 nm to 9.26±1.39 nm. After polishing, both surfaces have a similar average roughness and a controlled multistructuring can be performed. The setup for the microstructuring is depicted in Figure 5.5.

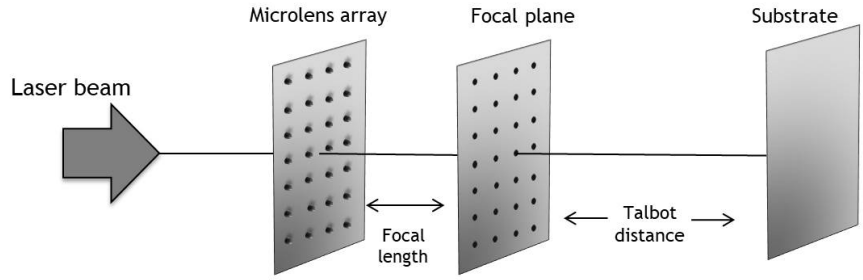

Figure 5.5: Experimental setup for the ablation of materials using the foci of a microlens array and a pulsed Nd:YAG laser. The material is placed at a Talbot distance from the foci.

For multistructuring, the Nd:YAG laser works in pulsed mode, at a wavelength of 532 nm. The laser beam illuminates the array and the substrates are place at the Talbot positions that were previously verified. Structures performed at the first integer Talbot plane and at 3/2 and 5/3 fractional self-images are shown for titanium and tantalum in Figure 5.6 and 5.7, respectively.

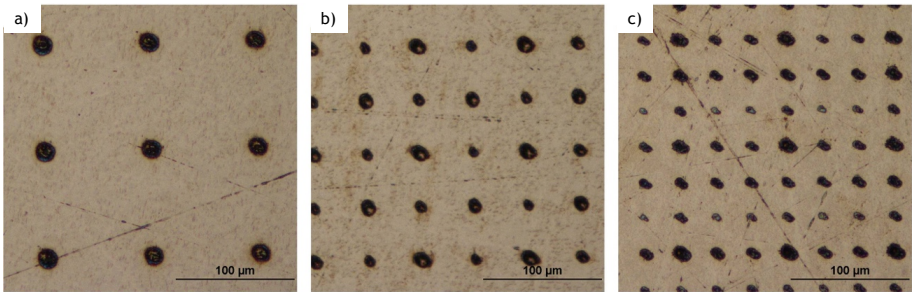

Figure 5.6: Optical microscope images of the micropattern over a titanium foil of 0.7 mm thickness obtained after ablation using the foci of the microlenses. The surface is placed at a) the first Talbot distance, b) the 3/2 Talbot distance and c) the 5/3 Talbot distance.

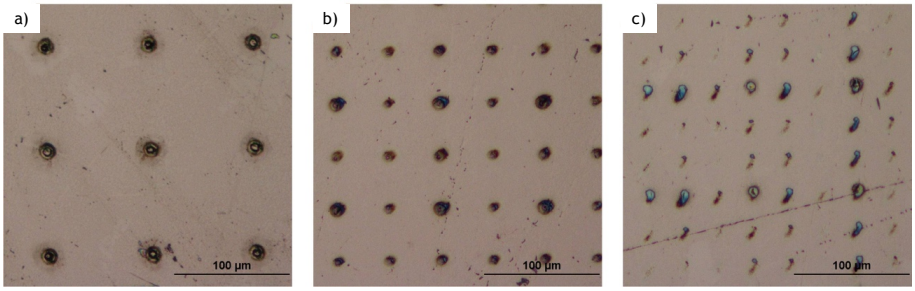

Figure 5.7: Optical microscope images of the micropattern over a tantalum foil of 0.5 mm thickness obtained after ablation using the foci of the microlenses. The surface is placed at a) the first Talbot distance, b) the 3/2 Talbot distance and c) the 5/3 Talbot distance.

Table 5.1 records the experimental values of different parameters of the resulting patterns of both substrates. According to Talbot theoretical formulas, the original period of 90 µm remains the same for the first integer Talbot image and decreases to 45 µm at the 3/2 plane and to 30 µm at the 5/3 fractional Talbot distance. As it can be seen in the figures and table, the period of the patterns is reduced as expected. The integer planes lead to deeper holes than fractional positions because each focus carries more energy than in the fractional case. The results show that, working with the same laser parameters, less material is removed from the tantalum than from the titanium during the ablation process. This make sense if we take into account that tantalum presents a higher hardness value than titanium. The exposure times needed for homogeneously microstructuring the surfaces are not the same for each plane. They correspond to 8 s for the first Talbot plane, 40 s for the 3/2 and 360 s for the 5/3. The 5/3 plane needs more exposure time than the others because there is less energy per focus than in the case of the first Talbot image, since the light redistributed through the image and through each unit cell. Actually, in the case of the tantalum there is not enough energy per focus to ablate the substrate homogeneously. In this case, it is tested an ablation trial with more exposure time but no differences are observed and no more material is removed. Therefore, there is a maximum quantity of material that can be removed by ablation using

these laser parameters and the Talbot effect. Figure 5.8 shows SEM images of a detail of every micropattern.

	Titanium			Tantalum		
	1st Talbot plane	3/2 Talbot plane	5/3 Talbot plane	1st Talbot plane	3/2 Talbot plane	5/3 Talbot plane
Microlens-substrate distance (mm)	16.21±0.01	23.85±0.01	26.42±0.01	16.21±0.01	23.85±0.01	26.42±0.01
Period (μm)	90.28±0.10	45.14±0.10	29.62±0.10	89.84±0.10	45.61±0.10	29.92±0.10
Spot diameter (μm)	16.15±0.10	12.20±0.10	5.52±0.10	13.26±0.10	10.77±0.10	5.44±0.10
Spot depth (μm)	3.1±0.3	2.2±0.3	0.8±0.3	2.3±0.3	1.7±0.3	0.6±0.3

Table 5.1: Experimental parameters of the patterns fabricated over titanium and tantalum substrates. All values are the mean of ten measurements ± the accuracy of the measurement, since standard deviation of the mean is negligible.

In Figure 5.8 a detail of a randomly chosen microhole of each of the fabricated microstructures is presented. As it can be seen in the SEM images, the size of the microhole decreases as the period of the Talbot plane decreases. The spot diameters of the different planes over titanium and tantalum are indicated in Table 5.1. In the case of 5/3 fractional planes, the diameter is comparable to the initial roughness of the surfaces. In this situation, the polishing of the substrates is not only crucial for minimizing the roughness effects in cells but also to differentiate the microholes through the sample. In these SEM images the difference in the ablation between materials, tantalum and titanium, can be also appreciated. More material is removed during the ablation process over titanium than in the tantalum process, leading to less deep structures in this last case. Finally, Figure 5.9 shows a representative SEM image of a microlens when ablating in a Talbot plane (Figure 5.9.a) and in the foci (Figure 5.9.b) in order to show the deterioration of the structure when working at a short distance from the array and to show the benefits of using the Talbot effect.

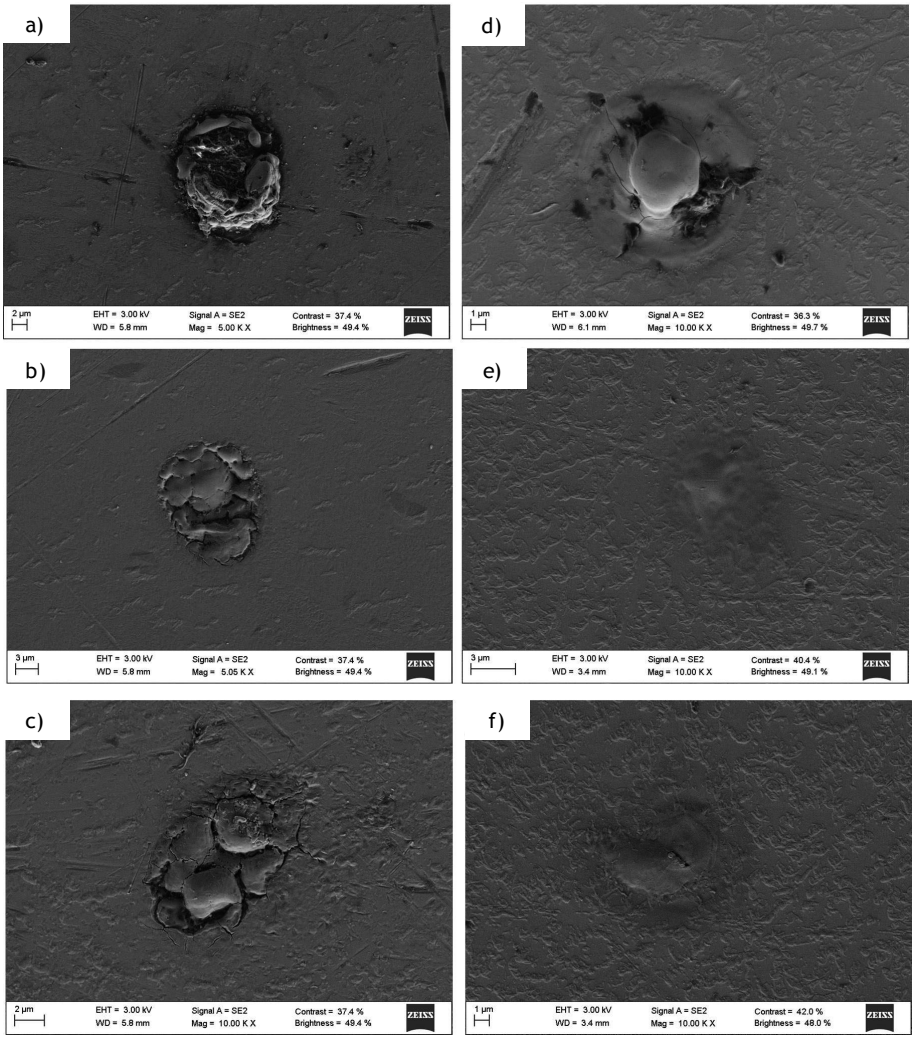

Figure 5.8: SEM images of the microholes obtained after laser ablation with a microlens array using the Talbot effect. Figures a) to c) show the patterns over titanium when working at the first, 3/2 and 5/3 Talbot distances, respectively. Figures d) to f) depict the holes over tantalum at the first, 3/2 and 5/3 sel-images, respectively.

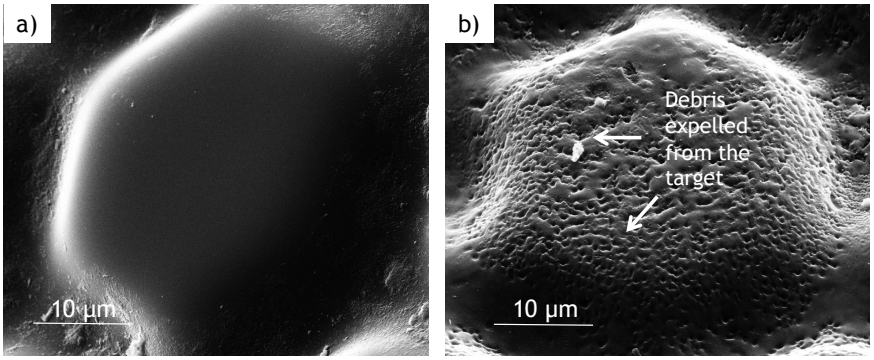

Figure 5.9: SEM images of a microlens employed for microstructuring after several usages when working a) in a Talbot plane and b) in the focal plane.

5.1.2. Evaluation of cell adhesion to the structured surfaces

Once the biocompatible materials are micropatterned by the technique presented above, human umbilical vein endothelial cells are cultured over them in order to observe differences in cell behaviour and spreading on structured and non-structured material, as well as differences among the patterns. HUVECs are cultured by following the same protocol as in Chapter 4 [34]. They are also stained with calcein, the viability indicator that emits green fluorescence when cells are alive. Titanium and tantalum foils are sterilized in an autoclave (120 ºC for 30 minutes) and immersed in endothelial growth medium (EGM-2) for 20 minutes before the cell deposition as a surface pre-treatment. Endothelial cells are seeded over the substrates at a concentration of $2 \cdot 10^5$ cells/1.5 ml and incubated for 17 hours at standard culture conditions (37 ºC temperature, more than 80% humidity and 5% CO_2 level). After this time, the foils are washed to remove the non-adherent cells and HUVECs are observed under fluorescence microscopy. Figure 5.10 shows representative fluorescence images of the obtained results.

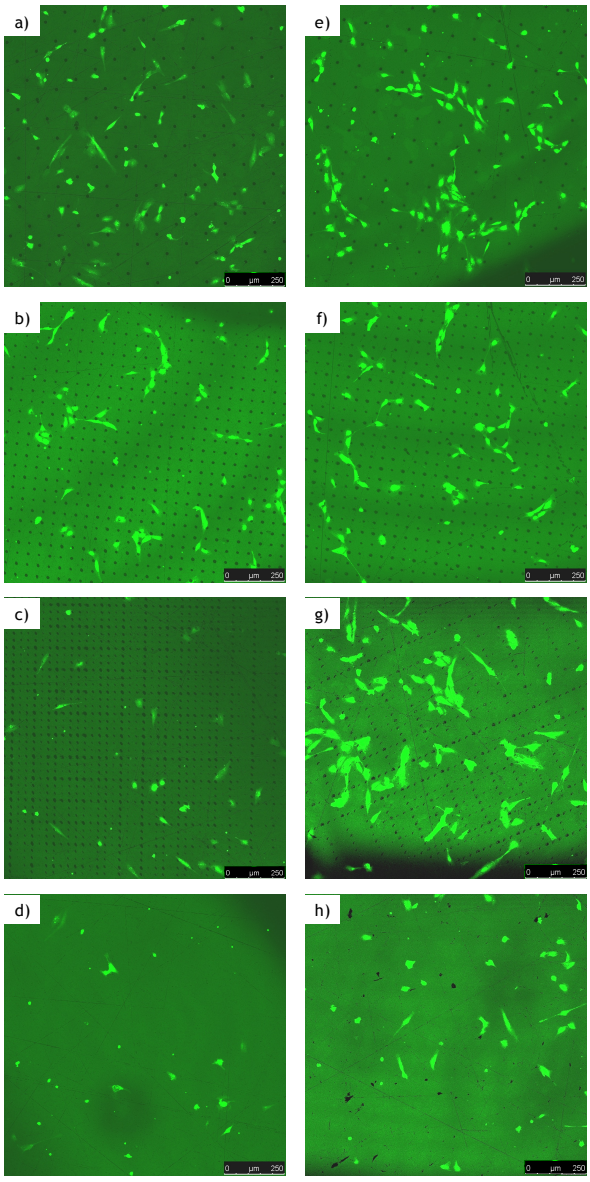

Figure 5.10: Fluorescence microscopy images of human umbilical vein endothelial cells over the different patterns after 17 h culture. Figures a) to c) show the cell attachment to the titanium surface when the period of the structure is 90 μm, 45 μm and 30 μm, respectively. Figures d) to h) depict the cellular spread over structured titanium with periods of is 90 μm, 45 μm and 30 μm, respectively.

In Figure 5.10, endothelial cell attachment to the different patterned and non-patterned surfaces can be seen. As calcein is a viability indicator, we can conclude that HUVECs are alive in all cases but interesting differences in cell growth and spreading can be observed between flat and structured surfaces. While in flat surfaces cells initially adhere randomly, in the patterned ones they attached to the holes rather than to the smooth substrate. Five random fields are counted per substrate area of interest and two different researchers made the count independently to get the experimental result. Experiments are conducted in triplicate and repeated three different times. The mean value and the standard error mean are calculated with these data. A Student's t-test is also performed to compare the data from the structured surfaces with those from the non-structured ones. A histogram that represents the number of alive cells per mm^2 in each pattern and for both titanium and tantalum is shown in Figure 5.11.

From figure 5.11 we can say that there is certain cell adhesion to the flat surfaces, due to their biocompatible nature, but the number of cells attached is quantitatively less than in the microstructured case. All the microstructured surfaces show a tendency to improve cell adhesion. However, only on the patterns of 30 μm and 90 μm in tantalum, and on 45 μm and 90 μm in titanium, cell adhesion is statistically higher in comparison with non-structured surface. Comparing both substrates, titanium and tantalum, we can say that in general, tantalum seemed to present a higher adhesion than titanium. Whereas in non-structured surfaces the cell spread is totally random, we observe that cells attached to the structures fabricated with laser and then spread and anchor around the holes. In Figure 12, detailed images of the adhesion of endothelial cells are shown in order to a better appreciation of the anchoring effect that microholes have in cell growth.

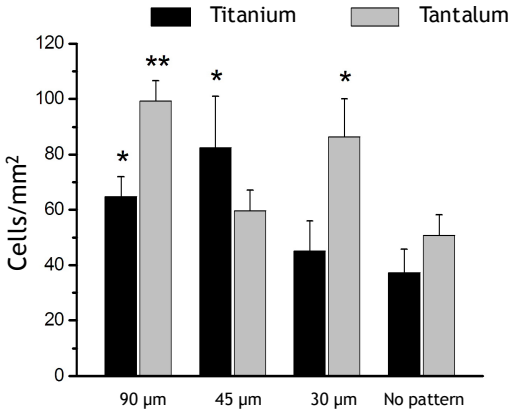

Figure 5.11: Histogram representing the number of cells per mm^2 of material (mean ± standard error of the mean in vertical bars) over the different structured and non-structured surfaces. *p<0.05 and **p<0.005 with respect to non-patterned surfaces.

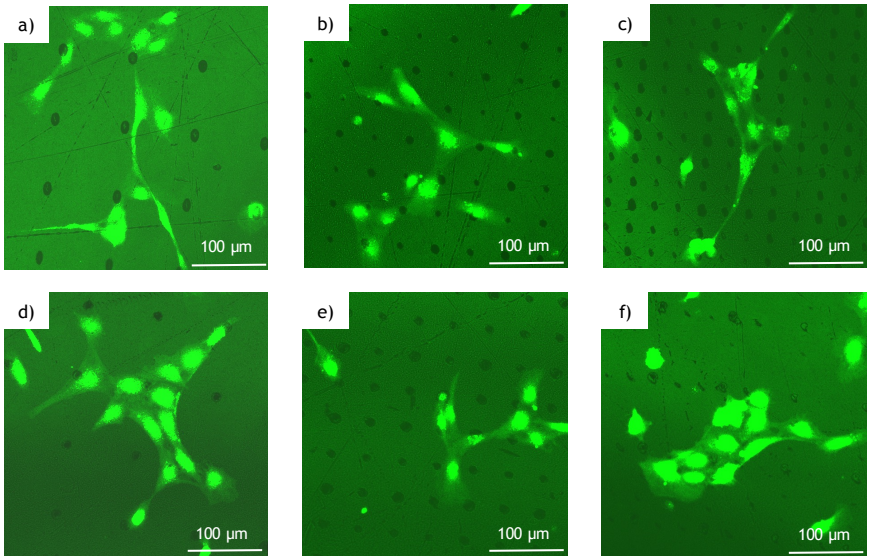

Figure 5.12: Fluorescence microscopy images of the HUVECs over the patterned surfaces after a culture of 17 h. Figures a) to c) show the endothelial cell attachment to the holes fabricated over titanium with period of 90 µm, 45 µm and 30 µm, respectively. Figures d) to f) depict cells over tantalum structures with pitch of 90 µm, 45 µm and 30 µm, respectively.

Figure 5.12 shows magnified fluorescence images of the human endothelial cells over the patterns. In the first hours of cell culture over both materials, HUVECs mainly adhere to the laser-generated holes rather than to the non-structured surface. Cells also prefer to attach to another cell that is already in contact with a microhole, and eventually spread to another structure, instead of adhering to the flat surface. It can be noticed how cells are placed over one or more holes or in contact with them. As it was already mentioned, several works demonstrate that a surface modification of the substrate on the micron scale affects to the cell adhesion and can regulate cellular functions [35]. SEM images of the cells spread over the patterned substrates is presented in Figure 5.13, where the effect discussed above can be clearly appreciated.

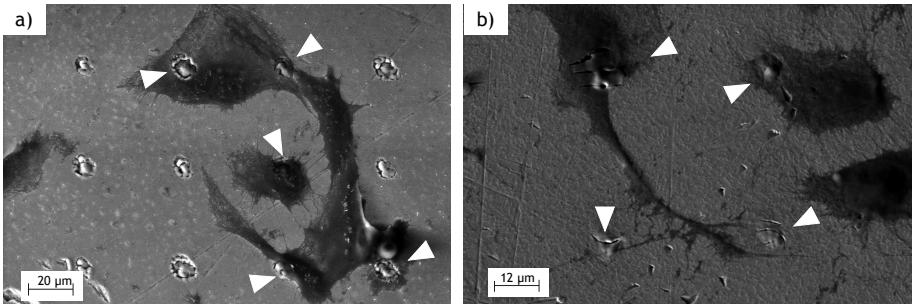

Figure 5.13: SEM images of the patterns of 45 µm on both a) titanium and b) tantalum, where the cellular guiding is shown. Arrow heads indicate the fabricated microholes that act as anchor points for cells.

Besides the guiding effect that microholes have in the endothelial cells, in Figure 5.13 it can be seen that there is a local modification of the average roughness inside the microhole in comparison with the flat surface. Roughness, as mentioned, is another physical factor that can control the cell adhesion. In conclusion, the fabrication of these structures alters the surface topography in the micron scale and also modifies the roughness inside the hole, leading microholes to act as anchor points for cells, increasing the number of cells adhered [36].

This work is a first approach to the biocompatibility of different structured material and to the cell response to them. In the future,

long-term biocompatibility tests could be performed in order to find the most suitable pattern for enhancing cell adhesion over different materials. The response of different kinds of cells over different substrates could also be evaluated.

5.2. LASER FABRICATION AND VALIDATION OF A MICROFLUIDIC DEVICE FOR CIRCULATING TUMOUR CELL CAPTURE

Laser technologies, as it was already mentioned, allows the fabrication of very different fluidic devices thanks to its design versatility and accuracy. Through this thesis, the applications of the manufactured structured were devoted to cardiovascular applications. Both the blood vessel-like device and the patterned titanium and tantalum were tested and validated with human umbilical vein endothelial cells. This makes sense since the final aim of the PDMS devices was the imitation of a coronary bifurcation and the biocompatible materials are commonly employed in prosthesis that need to be vascularized.

Nevertheless, and as it was noticed along this work, microfluidic devices have numerous application in different biomedical areas and disciplines. One example is the employment of microfluidic chips for the detection of tumour cells, which have emerged as promising and minimally invasive diagnostic tools [37]. Circulating tumour cells (CTCs) from cancerous tumours enter into the circulatory system, migrate to distant organs through the vascular tree and ultimately form metastases in other organs. With these devices, CTCs can be identified and studied, challenging task due to the heterogeneous characteristics of cancers [38]. The isolation of circulating tumour cells has become a central topic in cancer research. Thanks to the convergence of engineering and medical science, it is possible to capture rare cell types in liquid biopsies as a starting point for early diagnostic and the development of single cell analysis systems [39]. Several designs have been tried in PDMS [40] and glass substrates [41] leading to various features and arrangements able to trap cells that are flowing to the device. Different approach can be taken for this purpose, from size filtration of cells [42, 43] to dielectric properties separation [44]. One

interesting approach is the concept of binding cells to biomarkers [45, 46]. In these devices, tumour cells attach to a functionalized surface. Microposts are one of the designs developed for capturing circulating tumour cells in this way [47-49]. In order to enhance the specificity and sensibility of these systems, most of CTC isolation techniques rely on antibody-based capture of CTCs, which express epithelial cell surface markers. Among these, epithelial cell adhesion molecule (EpCAM) antibodies seem to be the first choice for developing a coating. EpCAM are transmembrane glycoproteins expressed in the epithelium and are the most employed molecules in antibody-based cell capture since its expression is practically universal, but it is absent in blood cells [50]. Functionalization and coating with antibodies against EpCAM is commonly used when capturing CTS, which are EpCAM-expressing cells.

In this section, a microfluidic device for capturing circulating tumour cells is fabricated over soda-lime glass. It is composed by and array of microposts and is manufactured via laser-induced plasma-assisted ablation using the Nd:YVO_4 laser. A posterior thermal treatment with the CO_2 laser combined with the roller furnace is applied to enhance the quality of the device. The applicability of the chips is tested by functionalizing the posts with an EpCAM antibody able to trap tumour cells, in particular, an endometrial cancer line.

5.2.1. Fabrication of the device

For the fabrication of the microfluidic chip over soda-lime glass, the Rofin PowerLine E Nd:YVO_4 laser is employed. Its specifications have been already presented, but briefly, its fundamental wavelength is 1064 nm and has a pulse duration of 20 ns. A system of mirrors addresses the beam and allows the design of the desired patterns. A flat field lens of 100 mm focal length is employed for focusing the laser beam. Laser-induced plasma-assisted ablation is the technique employed for the fabrication of the structures. This procedure has been presented in previous chapters in this thesis. Summarizing, the laser beam is focused over a metal foil that is placed below the glass

substrate. This metal initiates the ablation and material is removed from the rear side of the glass thanks to the generated plasma and expelled particles from the metal foil. In this way, bigger structures can be obtained than in direct laser ablation of the glass (the spot of the laser beam with this setup over glass does not reach 20 µm as it was indicated in Chapter 3). The manufactured structures for capturing CTCs consists in a set of microposts hexagonally packaged with 420 µm of diameter and pitch of 245 µm. Depth of microposts is 250 µm. These dimensions ensure that no cells will be trapped in between posts and allows having a high number of structures in a small area. Each cylindrical post is obtained by the ablation of a circular trench by moving the laser beam with the galvanometer mirror system and maintaining the glass in the same position. Laser operation parameters for this device are average power of 8 W, repetition rate of 10 kHz and scan speed of 500 mm/s. These values are relatively similar to the ones employed for the fabrication of the blood vessel-like structure in Chapter 3. A scheme of the experimental setup for the fabrication, as well as a scheme of the design is depicted in Figure 5.14.

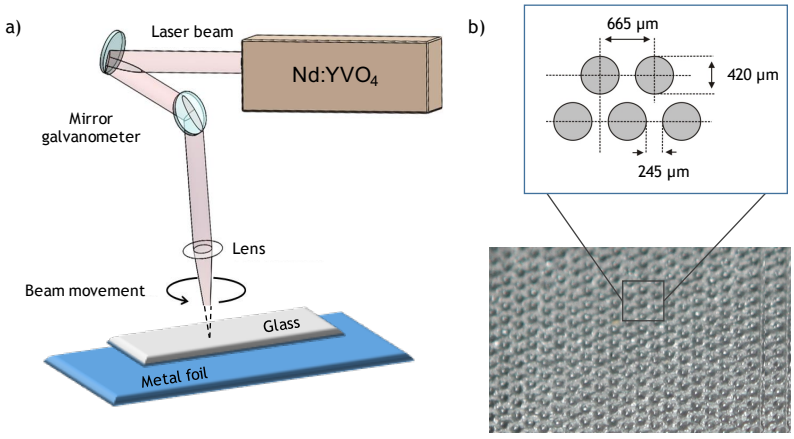

Figure 5.14: a) Scheme of the setup for the fabrication of the device via laser-induced plasma-assisted ablation. b) Arrangement of the microposts in the glass device, with a diameter of 420 µm and pich of 245 µm.

Laser-induced plasma-assisted ablation leads to very rough structures due to the explosive nature of the process. In order to enhance the quality of the sample by reducing its roughness and therefore, obtaining a more transparent device, which is key factor for further microscopic inspections, a thermal treatment is applied. It is performed with the Easy Mark 100 CO_2 laser in combination with the Nannetti ER20 roller furnace. Specifications of both systems can be found in Chapter 2. They were employed in Chapter 3 for reducing the roughness of the vessel-like channels. In that case, it was not the best choice due to the big dimensions of the channel and the number of times that the process had to be repeated in order to observe significant changes in the sample. Nevertheless, in this situation it is presented as a good option for the microposts, which are in the order of microns. The CO_2 laser has 10.6 μm wavelength with pulse duration of 10 μs. Laser parameters are repetition rate of 10 kHz, scan speed of 350 cm/s and 92 W power. The laser treatment is combined with a roller furnace that gradually heats the sample at 500 ºC to avoid cracks due to thermal shocks when the laser is focused over the glass. Through the furnace, the sample moves at a speed of 1000 mm/s. There is no need to repeat the process, contrary to the big dimension channels situation in Chapter 3. In this way, glass transition temperature of soda-lime glass is only exceeded in the surface of the sample, avoiding melting the whole piece. The thermal treatment applied with the laser reduces the damage created during the ablation in terms of roughness and transparency, leading to an improvement of morphological and optical quality of microposts. In figure 5.15 we can appreciate the morphological aspect of the posts before and after the thermal treatment.

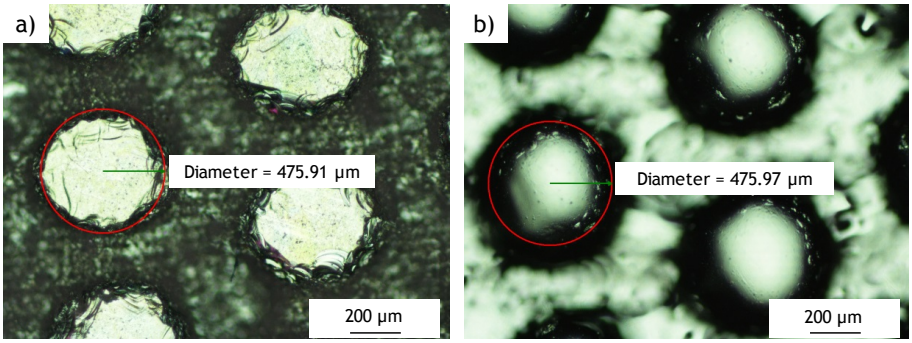

Figure 5.15: Microscope images of some micropost a) before and b) after the thermal treatment assisted by laser. Average profile roughness is reduced from 1230 nm to 159 nm.

Once the final structures are obtained over glass, the device must be closed in order to perform biological experiments. Besides the matrix of microposts, the device consists in an input channel for media perfusion and two output channels for its removal. They are performed by the same laser technologies as the array. The chip is covered with a microscope cover slide of 100 µm thickness. Holes of 0.5 mm are fabricated in the cover slide for connecting the tubes that will allow fluid perfusion through the chip. To properly attach the slide to the chip surface, optical quality UV curing adhesive is employed. The bonding takes place after 25 minutes at room temperature. Figure 5.16 shows an image of the appearance of the microfluidic device before being enclosed.

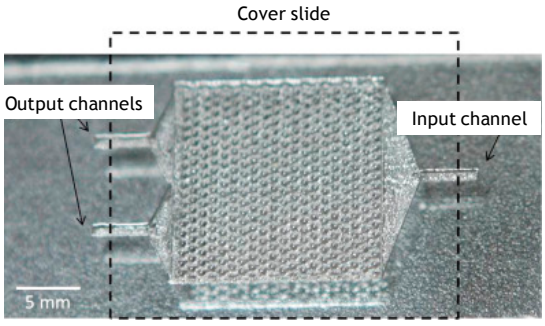

Figure 5.16: Appearance of the microfluidic device over soda-lime glass prior to its enclosure whit a cover slide.

5.2.2. Device validation

Once the device is completely closed and the connections are performed, the microposts are functionalized with EpCAM antibody for enhancing cell capture. To chemically modify the device, a variation of the protocol by Stott et al. [40] is carried out. The microfluidic device is treated with 4% concentrated solution of 3-mercaptopropyl trimethoxysilane in absolute ethanol for one hour at room temperature. Then, it is incubated in 0.01 μmol/ml N-y-maleimidobutyryloxysuccinimide ester in absolute ethanol for half an hour. Immediately after, the chip is treated with 10 μg/ml of NeutrAvidin solution in phosphate-buffered saline (PBS) for 45 minutes. The resulting functionalized device is soaked in avidin and placed overnight at 4 ºC. Next day, biotinylated goat antihuman EpCAM solution from R and D Systems at a concentration of 15 μg/ml in PBS supplemented with 1% bovine serum albumin (BSA) and 0.10 % sodium azide are added to the chip. Non-bonded molecules are rinsed out of the device after each step with an ethanol wash. Chips are finally cleared with 3% BSA with 0.05% Tween20 in ultrapure water. Figure 5.17 shows fluorescence microscopy images of the functionalization of the device with the antibody coating at different heights of the post. In this case, Alexa 488 is employed as secondary antibody that attach to the primary one and emits fluorescence signal. As it can be seen in the images, most of the surface has been coated with antobodies.

Once the device is functionalized, circulating tumour cells are perfused through it. An endometrial cancer line, HEC-1A, is cultured at 37 ºC, 5% CO_2 and more than 80% humidity in McCoy's-5A growth medium containing 1.5 ml L-glutamine supplemented with 10% fetal bovine serum (FBS) and 1% penicilin/streptomycin. The medium is changed every two days. Prior to the perfusing of the cells through the device, cells are labelled with a fluorescent cellular dye, DiO from Invitrogen, following the manufacturer recommended protocol. The experiments are carried out by using HEC-1A cells suspended in serum-free medium. Samples containing around 300

cells are loaded in 30 ml of medium and perfused through it with a peristaltic pump with a flow rate of 90 µl/min.

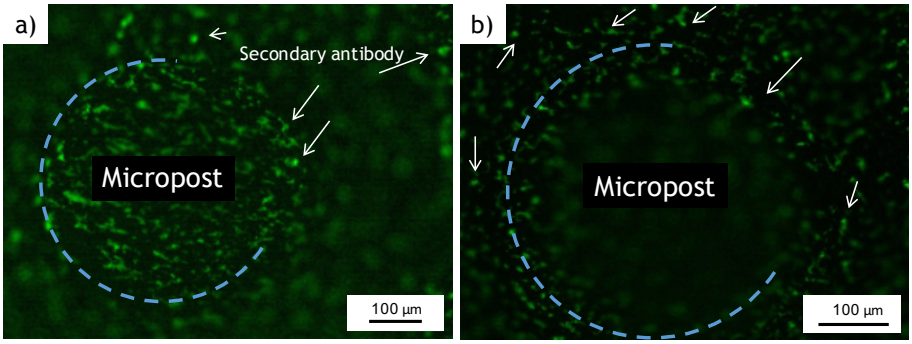

Figure 5.17: Fluorescence microscopy images of a) top and b) bottom planes of a micropost showing the antibody coating of the structures. Green signal is collected from the secondary antibody, providing an idea of the coating efficiency. White arrows denote secondary antibody distribution (green signal).

Experiments with the chips are observed under fluorescence microscopy in order to obtain a measurement of the attached cells to the microposts. The experiment is carried out seven times and three random areas of the device are randomly chosen in each case. Fluorescent CTCs are counted under fluorescence microscopy with a 20x magnification objective. The images are processed using the imaging software ImageJ. Fluorescent impurities that can come from residuals formed during the functionalization process or from dust are eliminated from the count by comparing the size and fluorescence intensity with the average characteristics of the manually identified CTCs, avoiding the alteration of the final result. The escape yield value is considered as the number of cells that do not attach to the posts and is counted as the number of cells presented in the collected flow after going through the device. The percentages are calculated from total number of cells injected in the device. For this reason and due to the uncertainty in the measurement of the initial amount of CTCs, the sum of trapping efficiency and escape yield can be higher than 100%. In Figure 5.18 a graphic that presents the trapping efficiency and escape yield for each event is plotted.

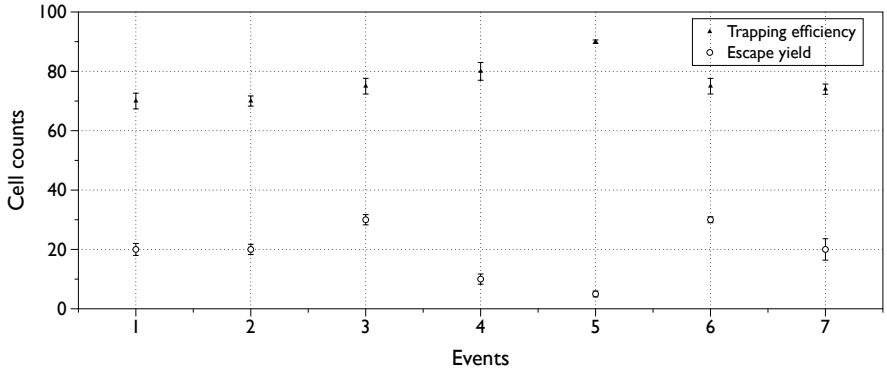

Figure 5.18: Cell trapping efficiency and escape yield of the device. The cell capture efficiency is calculated as the percentage ratio of circulating tumour cells captured by the microposts overt the total number of cells processed through the chip. Number of events is seven and three different areas of the device are randomly chosen to count the number of cells in each event.

As it can be seen in Figure 5.18, in every event at least 70% of the loaded cells are captured by the fabricated microposts. The number of cells that escape from the device have a maximum value through the events of 30% of the total perfused CTCs. Averaging all the events, a trapping efficiency of the 76.29±4,98% is obtained with the device, with a escaping yield of 19.29±6.73%. Representative fluorescence images of the attached HEC-1A cells to the microposts are shown in Figure 5.19.

Therefore, it is shown that a functional microfluidic device for capturing circulating tumour cells can be fabricated by laser technologies [51]. The coating with EpCAM antibody results satisfactory for enhancing trapping and cells remain attached to the structures during the whole flux experiment, proving a stable bond to the coating of the posts. This glass based microfluidic device presents exceptional optical quality features not related to the preparation protocols when compared to polymeric devices. This fact relies on the thermal treatment selected for this sample that does not alter the whole sample, but only the surface of the material where the structure is written on. Moreover, the chip does not exhibit hydrophobicity when perfusing the flux through it, like happens when working in small

scales with materials like PDMS that require of additional protocol steps to modify the wettability of the device. Also, the stiffness of the glass avoids the deformation of the structures, allowing consistent and stable flow conditions for long term experiments. Surface chemistry done over glass is easy to perform since this material is resistant to these treatments, making it an ideal substrate when using functionalization. Therefore, the presented glass substrates can provide a good starting point to develop more complex systems devoted to single cell analysis and isolation. Further work could be carried in order to explore additional architectures and chips modifications with different antibodies, allowing a satisfactory isolation of CTCs based on different ligands.

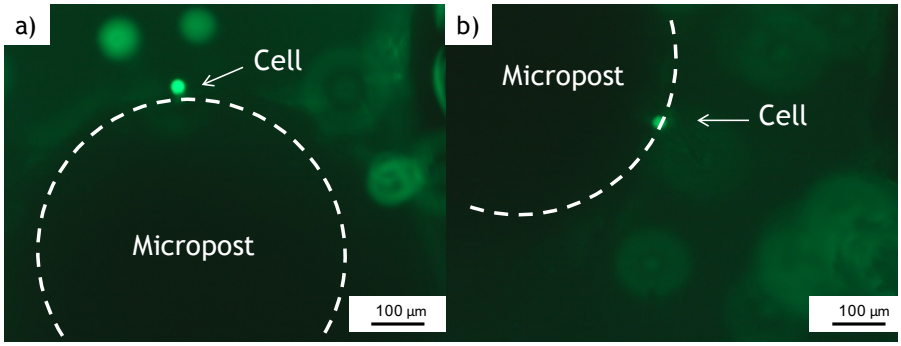

Figure 5.19: Fluorescence microscopy images of cell attachment to the functionalized surface of the micropost. Cells are strongly attached to the secondary antibodies and do not detach under flow conditions.

5.3. CONCLUSIONS

In this chapter, two different applications of laser structuring in biomedicine have been presented. First, a low cost method for fabricating periodic patterns over biocompatible materials, like titanium and tantalum, was introduced. These surfaces were microstructured in one single step by using the Talbot effect in combination with a microlens array. This is a rapid method for obtaining different patterns in an easy and fast way, just by varying the distance between the microlens array and the target. Moreover,

when working at a Talbot distance from the array, microlenses do not result as damaged as when placing them at the focal lenght. Talbot effect extend the work life of microlens arrays as it can be used as periodic object that reproduces the microlens focii instead of directly using the focii of the microlenses. This small difference in the separation of the array and the target is enough to avoid the deposition of expelled material on the microlenses and their damage. Cell adhesion of human umbilical vein endothelial cells over these microsturctured materials was studied. It was found that the manufactured structures acted as anchor points for the cells, such that preferentially adhered to the patterns and then spread toward other holes or attached cells. In this first approach, it was found that the 90 μm period pattern promoted cell adhesion on tantalum and the 45 μm period pattern did the same on titanium.

Second, by laser-induced plasma-assisted ablation, a microfluidic device for trapping circulating tumour cells was fabricated over soda-lime glass. The technique was combined with a CO_2 laser thermal treatment that improved the optical quality of the device as well as its morphological properties. This approach was a rapid and effective procedure to obtain glass microstructures that can be chemically modified, leading to the possibility of performing surface modification with EpCAM antibodies to successfully stop circulating tumour cells. Trapping efficiency with this device when endometrial cancer cells were perfused through it was more than the 75%.

REFERENCES

[1] V. Romano, H. P. Weber, G. Dumitru, S. M. Pimenov, T. V. Kononenko, V. I. Konov, H. Haefke, Y. Gerbig, M. Sentis, J. Hermann, S. Bruneau, and W. Marine, "Laser surface microstructuring to improve tribological systems," In *Laser Processing Adv. Materials Laser Microtech.*, vol. 5121, 2003, pp. 199–211.

[2] X. Liu, P.K. Chu, and C. Ding, "Surface modification of titanium alloys, and related materials for biomedical applications," *Mat, Sci. Eng.,* vol. 47, no. 3-4, pp. 49-121, 2004.

[3] D. E. Weibel, A. F. Michels, A. F. Feil, L. Amaral, S. R. Teixeira and F. Horowitz, "Adjustable hydrophobicity of Al substrates by chemical surface functionalization of nano/microstructures," *J. Phys. Chem. C*, vol. 114, pp. 13219–13225, 2010.

[4] N. C. Tien, S. Jeong, L. M. Phinney, K. Fushinobu, and J. Bokor, "Surface adhesion reduction in silicon microstructures using femtosecond laser pulses," *Appl. Phys. Lett*., vol. 68, no. 2, 197–199 1996.

[5] S. J. Hollister, "Porous scaffold design for tissue engineering," *Nature Materials,* vol. 4, no.7, pp. 518-524, 2005.

[6] L. Li, M. Mirhosseini, A. Michael, Z. Liu, and T. Wang, "Enhancement of endothelialisation of coronary stents," *Lasers Surgery Medicine,* vol. 45, no. 9, pp. 608-616, 2013.

[7] W. Koh and M. V Pishko, "Fabrication of cell-containing hydrogel microstructures inside microfluidic devices that can be used as cell-based biosensors," *Anal. Bioanal. Chem.*, vol. 385, no. 8, pp. 1389–1397, 2006.

[8] H. H. Huang, C. T. Ho, T. H. Lee, T. L. Lee, K. K. Liao, and F. L. Chen, "Effect of surface roughness of ground titanium on initial cell adhesion," *Biomol. Eng*., vol. 21, no. 3–5, pp. 93–97, 2004.

[9] R. J. Pelham and Y. Wang. "Cell locomotion and focal adhesions are regulated by substrate flexibility," *Proceedings of the National Academy of Sciences,* vol. 94, no. 25, pp. 13661-13665, 1997.

[10] H. G. Craighead, S. W. Turner, R. C: Davis, C. James, A. M: Perez, P. M. St John, and M. S. Isaacson, "Chemical and topographical surface modification for control of central nervous system cell adhesion," *Biomed. Microdevices,* vol. 1, no. 1, pp. 49–64, 1998.

[11] A. M. P. Turner, N. Dowell, S. W. P. Turner, L. Kann, M. Isaacson, J. N. Turner, H. G. Craighead, and W. Shain, "Attachment of astroglial cells to microfabricated pillar arrays of different geometries," *J. Biomed. Mat. Res.*, vol. 51, no 3, pp. 430-441, 2000.

[12] T. Ziebart, A. Schnell, C. Walter, P. W. Kämmerer, A. Pabst, K. M. Lehmann, J. Ziebart, M. O. Klein, and B. Al-Nawas, "Interactions between endothelial progenitor cells (EPC) and titanium implant surfaces," *Clin. Oral Invest.,* vol. 17, no. 1, pp. 301–309, 2013.

[13] D. Cristea, I. Ghiuta, and D. Munteanu, "Tantanlum based materials for implants and prostheses applications," *Bulletin of the Transilvania University of Brasov,* vol. 8, no. 2, pp. 151-158, 2015.

[14] M. Stiehler, M. Lind, T. Mygind, A. Baatrup, A. Dolatshahi-Pirouz, H. Li, M. Foss, F. Blesenbacher, M. Kassem, and C. Bunger, "Morphology, proliferation, and osteogenic differentiation of mesenchymal stem cells cultured on titanium, tantalum, and chromium surfaces," *J. Biomed. Mater. Res. A*, vol. 86, no. 2, pp. 448–458, 2008.

[15] D. Khang, J. Lu, C. Yao, K. M. Haberstroh, and T. J. Webster, "The role of nanometer and sub-micron surface features on vascular and bone cell adhesion on titanium," *Biomaterials*, vol. 29, no. 8, pp. 970–983, 2008.

[16] J. Lu, M.R. Rao, N.C. MacDonald, D. Khang, and T.J. Webster, "Improved endothelial cell adhesion and proliferation on patterned titanium surfaces with rationally designed, micrometer to nanometer features," *Acta Biomaterialia,* vol. 4, no. 1, pp. 192-201 2007.

[17] P. Vandrangi, S. C. Gott, R. Kozaka, V. G. J. Rodgers, and M. P. Rao, "Comparative endothelial cell response on topographically patterned titanium and silicon substrates with micrometer to sub-micrometer feature sizes," *PLoS One*, vol. 9, no. 10, pp. 1-13, 2014.

[18] J. Justesen, M. Lorentzen, L. K. Andersen, O. Hansen, J. Chevalier, C. Modin, A. Füchtbauer, M. Foss, F. Besenbacher, M. Duch, and F. S. Pedersen, "Spatial and temporal changes in the morphology of preosteoblastic cells seeded on microstructured tantalum surfaces," *J. Biomed. Mater. Res. A*, vol. 89, no. 4, pp. 885–894, 2008.

[19] Y. Yang, J. Yang, C. Liang, H. Wang, X. Zhu, and N. Zhang, "Surface microstructuring of Ti plates by femtosecond lasers in liquid ambiences : a new approach to improving biocompatibility," *Opt. Express,* vol. 17, no. 23, pp. 5694–5696, 2009.

[20] D. Nieto, G. Vara, J.A. Díez, G. M. O'Connor, J. Arines, C. Gómez-Reino, and M.T. Flores-Arias, "Laser-based microstructuring of surfaces using low-cost microlens arrays," *J. Micro/Nanolithography, MEMS MOEMS*, vol. 11, no. 2, p. 23014, 1-7, 2012.

[21] M. He, X. C. Yuan, N. Ngo, J. Bu, and S. Tao, "Low-cost and efficient coupling technique using reflowed sol- gel microlens," *Opt. Express,* vol. 11, no. 14, pp. 1621–1627, 2003.

[22] M. Aymerich, D. Nieto, and M. T. Flores-Arias, "Laser-based surface multistructuring using optical elements and the Talbot effect," *Opt. Express*, vol. 23, no. 19, pp. 24369-24382, 2015.

[23] E. Wolf, Ed., *The Self-Imaging Phenomenon and its applications*, Rochester: Progress in Optics Vol. 27, 1989.

[24] M.V. Berry and S. Klein, "Integer, fractional and fractal Talbot effects," *J. Mod. Opt.,* vol. 43, no. 10, pp. 2139-2164, 1996.

[25] Y. Lin, M. H. Hong, G. X. Chen, C. S. Lim, Z. B. Wang, L. S. Tan, L. P. Shi, and T. C. Chong, "Patterning of phase change films with microlens arrays," *J. Alloys Compd*., vol. 449, no. 1-2, pp. 253–257, 2008.

[26] C. S. Lim, M. H. Hong, Y. Lin, G. X. Chen, A. Senthil Kumar, M. Rahman, L. S. Tan, J. Y. H. Fuh, and G. C. Lim, "Sub-micron surface patterning by laser irradiation through microlens arrays," *J. Mater. Process. Technol.,* vol. 192, pp. 328–333 2007.

[27] A. W. Lohmann, D. Mendlovic, and G. Shabtay, "Talbot (1836), Montgomery (1967), Lau (1948) and Wolf (1955) on periodicity in optics," *Pure Appl. Opt.,* vol. 7, no. 5, pp. 1121–1124 1998.

[28] W. D. Montgomery, "Self-Imaging Objects on Infinite Aperture," *J. Opt. Soc. Am.,* vol. 57, no. 6, pp. 772–778, 1967.

[29] C. Gómez-Reino, M.V. Pérez and C. Bao, *Gradient-Index Optics. Fundamentals and Applications,* Springer, 2002.

[30] B. Besold and N. Lindlein, "Fractional Talbot effect for periodic microlens arrays," *Opt. Eng.,* vol. 36, no. 4, pp. 1099-1105 1997.

[31] D. D. Deligianni, N. Katsala, S. Ladas, D. Sotiropoulou, J. Amedee, and Y. F. Missirlis, "Effect of surface roughness of the

titanium alloy Ti–6Al–4V on human bone marrow cell response and on protein adsorption," *Biomaterials,* vol. 22, no. 11, pp. 1241-1251, 2001.

[32] M. O. Klein, A. Bijelic, T. Ziebart, F. Koch, P. W. Kämmerer, M. Wieland, and B. Al-Nawas, "Submicron scale-structured hydrophilic titanium surfaces promote early osteogenic gene response for cell adhesion and cell differentiation," *Clin. Implant Dent. Relat. Res.*, vol. 15, no. 2, pp. 166-175, 2013.

[33] K. Anselme and M. Bigerelle, "On the relation between surface roughness of metallic substrates and adhesion of human primary bone cells," *Scanning,* vol. 36, no. 1, pp. 11-20 2014.

[34] B. K. Rodiño-Janeiro, M. González-Peteiro, R. Ucieda-Somoza, J. R. González-Juanatey, and E. Álvarez, "Glycated albumin, a precursor of advanced glycation end-products, up-regulates NADPH oxidase and enhances oxidative stress in human endothelial cells: molecular correlate of diabetic vasculopathy," *Diabetes Metab. Res. Rev.,* vol. 26, pp. 550-558, 2010.

[35] Lim, J. Yul, and H. J. Donahue. "Cell sensing and response to micro-and nanostructured surfaces produced by chemical and topographic patterning," *Tissue Eng.,* vol. 13, no. 8, 1879-1891 2007.

[36] M. Aymerich, D. Nieto, E. Álvarez, and M. T. Flores-Arias, "Laser surface microstructuring of biocompatible materials using a microlens array and the Talbot effect: evaluation of the cell adhesion," *Materials*, vol. 10, no. 2, pp. 214, 1-13. 2017.

[37] A. van de Stolpe, K. Pantel, S. Sleijfer, L. W. Terstappen, and J. M. Den Toonder, "Circulating tumor cell isolation and diagnostics: toward routine clinical use," *Cancer Res,* vol. 71, no. 18, pp. 1-6, 2011.

[38] Y. Dong, A.M. Skelley, K.D. Merdek, K.M. Sprott, and C. Jiang, "Microfluidics and circulating tumor cells," *J. Mol. Diagn.,* vol. 15, no. 2, pp. 149-157, 2013.

[39] C. Wyatt Shields, C.E. Livingston, B.B. Yellen, G.P. López, and D.M. Murdoch, "Magnetographic array for the capture and enumeration of single cells and cell pairs," *Biomicrofluidics,* vol. 8, no. 4, pp. 041101-041104, 2014.

[40] S. L. Stott, C. H. Hsu, D. I. Tsukrov, M. Yu, D. T. Miyamoto, B. A. Waltman, S. M. Rothenberg, A. M. Shah, M. E. Smas, G. K. Korir, F. P. Floyd, Anna J. Gilman, J. B. Lord, D. Winokur, S. Springer, S. Irimia, S. Nagrath, L. V. Sequist, R. J. Lee, K J. Isselbacher, S. Maheswaran, D. A. Haber, and Mehmet Toner, "Isolation of circulating tumor cells using a microvortex-generating herringbone-chip," *PNAS,* vol. 107, no. 43, pp. 18392-18397, 2010.

[41] S. Dochow, C. Krafft, U. Neugebauer, T. Bocklitz, T. Henkel, G. Mayer , J. Albert and J. Popp, "Lab on a Chip Tumour cell identification by means of Raman spectroscopy in combination with optical traps and microfluidic environments," *Lab Chip*, vol. 11, no.8 pp. 1484–1490, 2011.

[42] H. Mohamed, M. Murray, J. N. Turner, and M. Caggana, "Isolation of tumor cells using size and deformation," *J. Chromatography A,* vol. 1216, no. 47, pp. 8289–8295, 2009.

[43] S. J. Tan, L. Yobas, G. Yew, H. Lee, C. N. Omg, and C. T. Lim "Microdevice for the isolation and enumeration of cancer cells from blood," *Biomed. Microdevices,* vol. 11, no. 4, pp. 883–892, 2009.

[44] F. F. Becker, X. Wang, Y. Huang, R. Pethigt, J. Vykoukal, and P. R. C. Gascoyne, "Separation of human breast cancer cells from blood by differential dielectric affinity," *Proc. Natl. Aca. Sci. USA,* vol. 92, no. 3, pp. 860–864, 1995.

[45] A. D. Hughes and M. R. King, "Use of naturally occurring halloysite nanotubes for enhanced capture of flowing cells," *Langmuir*, vol. 26, no. 14, pp. 12155-12164, 2010

[46] S. Mittal, I. Y. Wong, W. M. Deen, and M. Toner, "Antibody-Functionalized Fluid-Permeable Surfaces for Rolling Cell Capture at High Flow Rates," Biophysj, vol. 102, no. 4, pp. 721–730, 2012

[47] S. Nagrath, L.V. Sequist, S. Maheswaran, D.W. Bell, D. Irimia, L. Ulkus, M.R.Smith, E.L. Kwak, S. Digumarthy, A. Muzikansky, P. Ryan, U.J. Balis, R.G.Tompkins, D.A. Haber, and M. Toner,, "Isolation of rare circulating tumour cells in cancer patients by microchip technology," *Nature,* vol. 450, no 7173, pp. 1235-1239, 2007.

[48] L.S. Stott, C.H. Hsu, D.I. Tsukrov, M. Yu, and D.T. Miyamoto, "Isolation and characterization of circulating tumor cells from patients with localized and metastatic prostate cancer," *Sci. Translational Medicine,* vol. 2, no. 25, pp. 25ra23, 1-11, 2010.

[49] L. V Sequist, S. Nagrath, M. Toner, D. A. Haber, and T. J. Lynch, "The CTC-Chip," JTO Acquis., vol. 4, no. 3, pp. 281–283, 2009.

[50] M. Yu, S. Stott, M. Toner, S. Maheswaran, and D. A. Haber, "Circulating tumor cells : approaches to isolation and characterization," vol. 192, no. 3, pp. 373–382, 2011.

[51] D. Nieto, R. Couceiro, M. Aymerich, R. Lopez-Lopez, M. Abal, and M. T. Flores-arias, "A laser-based technology for fabricating a soda-lime glass based microfluidic device for circulating tumour cell capture," *Colloids Surf. B*, vol. 134, pp. 363–369, 2015.

CONCLUSIONS

This thesis presents the structuring of materials by laser technologies for applications in the biomedical field. Most of the structures were performed over soda-lime glass. In particular, microchannels for microfluidic applications with different laser systems, masters for preclinical devices that imitated a coronary bifurcation and microfluidic chips that captured tumour cells. The main conclusions derived from this work are summarized as follows:

- Laser ablation in the infrared spectral range was presented as an effective method for the fabrication of devices for the biomedical field by the ablation of transparent materials, like soda-lime glass, via direct ablation methods or indirect ones, like laser-induced plasma-assisted ablation.

- Microchannels for microfluidic applications were fabricated by laser direct writing over soda-lime glass with lasers working in three different temporal regimes: nanosecond, picosecond and femtosecond, all of them with infrared operating wavelengths. For comparison, optimal laser parameters and scans were determined to obtain channels with semi-circular profiles with each pulse duration. It was demonstrated that with the three laser systems, microchannels with similar dimensions were obtained. In particular, we fabricated structures with 20 μm diameter and 10 μm depth.

- It was found that tin impurities that were presented only in one side of soda-lime glass, derived from the fabrication process of the material, played a key role in the proper ablation of quality microchannels. In the nanosecond process, they were responsible for the initialization of ablation, acting as seed

electrons in the avalanche ionization process. If these dopants were not presented in the surface, ablation would not occur. For picosecond and femtosecond pulse durations, due to the physical phenomena involved in absorption, ablation took place in both sides of the glass, but with significant differences between the surfaces. Whilst when working in the doped side good channels were obtained, when ablating the non-doped surface, cracks and edge chirping appeared. This was related to the thermal diffusivity of the material, which resulted increased with the presence of tin impurities, avoiding the creation of imperfections in the structure.

- Arithmetical average surface roughness (S_a) obtained from the bottom of the microchannels was significant different regarding the pulse duration of the laser employed for the fabrication. Microchannels manufactured with the nanosecond laser had 178.7±15.6 nm surface roughness. With the picosecond 1028.3±198.4 nm surface roughness was achieved and 1016.3±123.8 nm with the femtosecond system. These roughness values were modified in a controlled way by applying thermal treatments with a static furnace, reducing the value up to 12.1±1.7 nm. Therefore, suitable microchannels were obtained for several microfluidics applications that require of specific roughness values for their proper development, like high surface roughness for cell culture or low roughness for fluid dynamics.

- Channels with millimetre depth were manufactured by laser-induced plasma-assisted ablation in the infrared spectral range and nanosecond pulse duration over soda-lime glass. Laser optimal parameters were determined as 8 W average power, 12 kHz repetition rate, 1000 mm/s speed and 25 μm distance between consecutive scans. Arithmetical average profile roughness (R_a) of the channel bottom was measured, obtaining 5285.01±304.56 nm.

- Shape and profile roughness of the channels were modified by means of thermal treatments. CO_2 laser irradiation combined with a roller furnace was shown as a non-optimal procedure for the modification of the topography. Thermal treatments with a static furnace were more suitable for altering the profile and roughness of the channels, reducing R_a up to 27.18±4.52 nm.

- The millimetre glass channels were employed as master for fabricating a device that mimicked a blood coronary bifurcation. The structure was replicated in PDMS via soft-lithography techniques. Two procedures for replica and sealing were carried out. One consisted in different PDMS compositions for the different components of the chip. Nevertheless, this technique was more delicate and had a higher probability of failure due to the handling of soft materials. The other one was presented as a more robust technique, and it was based on oxygen plasma activation of the surfaces for bonding the device.

- The final PDMS device was biologically validated by culturing human umbilical vein endothelial cells (HUVECs) over their inner walls. For ensuring the presence of cells in the totality of the structure, a two-step culture process was carried out. First, cells were cultured over the bottom of the channel. Second, after several hours, it was turned around and more HUVECs were cultured over the other surface. By this technique, cells were presented not only on the top and bottom of the device but also in the laterals.

- Cell attachment to the surface of the device was evaluated regarding the roughness of the inner walls. For this purpose, four devices with different arithmetical average profile roughness were fabricated from glass masters with different thermal treatments. After culturing HUVECs in the devices and perfusing flux through them at a velocity of 1 ml/min, it

was found that the device with R_a of 1528.01±100.01 nm presented the optimal roughness for avoiding cell detachment in dynamic flow conditions. This device was validated with flow velocities up to 10 ml/min.

- Sol-gel chemistry was employed for coating the PDMS channels in order to avoid the deterioration of PDMS when it is in contact with some organic solvents, like ethanol. Three compositions were employed: 60MTES/40TEOS, 70MTES/30TISP and 80MTES/20TISP. While the three types demonstrated to be biocompatible and allowed HUVEC culture in their surfaces, 80MTES/20TISP was the best of the three since the cells cultured over this coating attempted of to form a monolayer instead of remaining in a cluster.

- PDMS devices with different geometries were employed for determining fluid dynamics in coronary bifurcations. Low velocity areas, where pathologies like vascular disease or deposition of circulating tumour cells (CTCs) are more prone to occur, were experimentally determined in the devices and compared with numerical simulations. In both cases, it was found that the area of these low velocity zones is bigger in geometries with 90º degree bifurcation angle.

- Titanium and tantalum surfaces were microstructured by laser technologies using a microlens array in combination with the Talbot effect. Using integer and fractional Talbot effects, identical patterns to the focii of the array or with minor period can be achieved at larger distances than the focal length of the microlens array. By doing this, the particles expelled during the ablation of the target did not reach the array and it did not result damaged, extending the working lifetime of the microlenses.

- Endothelial cell attachment to the different patterns previously manufactured on titanium and tantalum was evaluated. It was

determined that cell adhesion was enhanced over the patterns in contrast with the flat surface. In particular, it had a maximum adhesion for values of the period of the pattern equal to 45 μm on titanium and 90 μm over the tantalum, respectively. It was concluded that the manufactured holes over the surfaces acted as anchor points to the cells that first attached to them and then spread toward other structure or to an already anchored cell.

- A microfluidic device for capturing circulating tumour cells was manufactured by laser-induced plasma-assisted ablation over soda-lime glass. The device consisted in an array of microposts that were functionalized with EpCAM antibodies, trapping CTCs when in contact with them. The chip was validated with endometrial tumour cells that were flown through the device, demonstrating a trapping efficiency higher than the 75%.

PUBLICATIONS

- M. Aymerich, D. Nieto, and M. T. Flores-Arias, "Laser-based surface multistructuring using optical elements and the Talbot effect," *Opt. Express*, vol. 23, no. 19, pp. 24369-24382, 2015.

- D. Nieto, R. Couceiro, M. Aymerich, R. Lopez-Lopez, M. Abal, and M. T. Flores-arias, "A laser-based technology for fabricating a soda-lime glass based microfluidic device for circulating tumour cell capture," *Colloids Surf. B*, vol. 134, pp. 363–369, 2015.

- A. Gargallo, A. I. Gómez-Varela, H. Nuñez, T. Delgado, C. Almaguer, F. Cambronero-López, A. Sánchez, D. Pallarés, M. Aymerich, A. L. Aragón-Beloso, and M. T. Flores-Arias, "Spreading Optics in the Primary School", *J. Phys. Conf. Ser.*, vol. 605, no. 1, pp. 012040-012046, 2015.

- M. Aymerich, A. I. Gómez-Varela, E. Álvarez, and M. T. Flores-Arias, "Study of different sol-gel coatings to enhance the lifetime of PDMS devices: evaluation of their biocompatibility," *Materials*, vol. 9, no. 9, pp. 728, 1-11, 2016.

- M. Aymerich, D. Nieto, E. Álvarez, and M. T. Flores-Arias, "Laser surface microstructuring of biocompatible materials using a microlens array and the Talbot effect: evaluation of the cell adhesion," *Materials*, vol. 10, no. 2, pp. 214, 1-13. 2017.

- M. Aymerich, E. Álvarez, C. Bao-Varela, I. Moscoso, J. R. González-Juanatey, and M. T. Flores-Arias, "Laser technique for the fabrication of blood vessels-like models for preclinical

studies of pathologies under flow conditions," *Biofabrication*, vol. 9, no. 2, pp. 025033, 1-7, 2017.

- A. I. Gómez-Varela, M. Aymerich, D. Nieto Y Castro Martin, P. A. A. de Beule, E, Álvarez, C. Bao-Varela, and M. T. Flores-Arias, "Sol-Gel glass coating synthesis for different applications: Active Gradient-Index materials, microlens arrays and biocompatible channels," in *Recent Applications in Sol-Gel Synthesis*, U. Chandra, Ed. InTech, 2017.

- A. Otero-Cacho, M. Aymerich, M. T. Flores-Arias, M. Abal, E. Álvarez, V. Pérez-Muñuzuri, and A. P. Muñuzuri, "Determination of hemodynamic risk for vascular disease in planar artery bifurcations," *Sci. Rep.*, vol. 8, no. 1, pp. 2795, 1-7, 2018.

- M. Aymerich, D. Canteli, J. R. Vázquez de Aldana, C. Molpeceres and M. T. Flores-Arias "Comparative study of high-quality microchannels fabricated over soda-lime glass with near-infrared nano, pico and femtosecond pulses," Under preparation.

CONTRIBUTIONS TO CONFERENCES

- R. Couceiro, C. Tubio, V. Calviño, M. Aymerich, B. L. Bouzo, and R. López-López, Aproximación traslacional a patologías clínicas por medio de modelización 3D en sistemas altamente personalizables, *Biointegrasaúde 2015*, 16 June 2015, Vigo (Spain).

- M. Aymerich, Daniel Nieto, and M. T. Flores-Arias, Aplicación del efecto Talbot para el microestructurado de superficies empleando un objeto periódico, *OPTOEL 2015*, 13-15 July 2015, Salamanca (Spain).

- A. Gargallo, A. I. Gómez-Varela, F. Cambronero, T. Delgado, M. Aymerich; A. Luis Aragón, A. García-Sánchez, and M. T. Flores-Arias, Actividades divulgativas para el Año Internacional de la Luz de USC-OSA y USC-EPS, *XI Reunión Nacional de Óptica*, 1-3 September 2015, Salamanca (Spain).

- M. Aymerich, Daniel Nieto, and M. T. Flores-Arias, Multiestructurado de superficies de materiales biocompatibles con láser utilizando una matriz de microlentes y el efecto Talbot, *IV Encontro Mocidade Investigadora*, 9-10 June 2016, Santiago de Compostela (Spain).

- A. I. Gómez-Varela, C. Bao-Varela, A. Gargallo, F. Cambronero, M. Aymerich, T. Delgado, A. L. Aragón, A. Sánchez-García, S. Williamson, and M. T. Flores-Arias, Talleres de experimentación de color para las enseñanzas de educación primaria, *XI Congreso Nacional del Color*, 19-22 July 2016, Ourense (Spain).

- M. Aymerich, Daniel Nieto, R. Couceiro, and M. T. Flores-Arias, Fabricación y validación de dispositivos de microfluídica sobre vidrio con tecnología láser, *XII Workshop on Materials Processing with Laser Technology*, 29-30 September 2016, O Porriño (Spain).

- A. Otero-Cacho, M. Aymerich, M. Abal, C. Bao-Varela, E. Álvarez, M. T. Flores-Arias, J. Guiu-Souto, A. P. Muñuzuri, and V. Pérez-Muñuzuri, Prediction of atherosclerosis risk from a numerical investigation of blood flow in models of coronary artery bifurcations, *Global Engage 2nd Microfluidic Congress*, 20-21 October 2016, London (United Kingdom).

- M. Aymerich, E. Álvarez, C. Bao-Varela, D. Nieto, A. P. Muñuzuri, M. Abal, and M. T. Flores-Arias, Fabrication and design of channels with laser technologies to mimic blood vessels, *Global Engage 2nd Microfluidic Congress*, 20-21 October 2016, London (United Kingdom).

- M. Aymerich, F. Cambronero, A. Aragón, T. Delgado, M. Blanco, A. I. Gómez-Varela, A. Gargallo, S. Williamson, A. Amorín, A. Sánchez-García, C. Bao-Varela, and M. T. Flores-Arias, The USC-OSA-EPS section activities in optics, *Applications in Optics and Photonics*, 8-12 May 2017, Faro (Portugal).

- M. Aymerich, A. I. Gómez-Varela, E. Álvarez, and M. T. Flores-Arias, Laser based manufacturing of channels and improvement of their life time with sol-gel coatings, *Applications in Optics and Photonics*, 8-12 May 2017, Faro (Portugal).

- M. Aymerich, F. Cambronero, A. Aragón, T. Delgado, M. Blanco, A. I. Gómez-Varela, A. Gargallo, S. Williamson, A. Amorín, A. Sánchez-García, C. Bao-Varela, and M. T. Flores-Arias, The USC-EPS Young Minds Section Activities in

Optics, *6th Young Minds Leadership*, 12-13 May 2017, Naples (Italy).

- M. Aymerich, D. Nieto, E. Álvarez, and M. T. Flores-Arias, Laser surface multistructuring of biocompatible materials using a microlens array and the Talbot Effect, *CLEO Europe*, 25-29 June 2017, Munich (Germany).

- M. Aymerich, E. Álvarez, C. Bao-Varela, and M. T. Flores-Arias, Laser based fabrication of preclinical devices for fluidic experiments, *CLEO Europe*, 25-29 June 2017, Munich (Germany).

- M. T. Flores-Arias, C. Bao-Varela, J. Arines, M. Blanco, M. Aymerich, A. Aragón, and F. Cambronero, STELA (Santiago Terawatt Laser): instalación y características de sus líneas de baja y alta potencia, *X Reunión Nacional de Optoelectrónica (OPTOEL17)*, 12-14 July 2017, Santiago de Compostela (Spain).

- M. Aymerich, F. Cambronero, A. Aragón, T. Delgado, M. Blanco, A. I. Gómez-Varela, A. Gargallo, S. Williamson, A. Amorín, A. Sánchez-García, C. Bao-Varela, and M. T. Flores-Arias, La actividad del grupo USC-OSA-EPS Student Chapter en la divulgación de la Óptica, *X Reunión Nacional de Optoelectrónica (OPTOEL17)*, 12-14 July 2017, Santiago de Compostela (Spain).

- M. Aymerich, E. Álvarez, C. Bao-Varela, I. Moscoso, J. R. González-Juanatey, and M. T. Flores-Arias, Fabricación mediante láser de dispositivos preclínicos funcionales para el estudio de patologías in-vitro bajo condiciones de flujo, *X Reunión Nacional de Optoelectrónica (OPTOEL17)*, 12-14 July 2017, Santiago de Compostela (Spain).

- A. Otero-Cacho, M. Aymerich, M. T. Flores-Arias, E. Álvarez, A. P. Muñuzuri, and V. Pérez-Muñuzuri, Experimental validation of numerical models for atherosclerosis risk prediction using preclinical devices fabricated with laser, *X Reunión Nacional de Optoelectrónica (OPTOEL17)*, 12-14 July 2017, Santiago de Compostela (Spain).

- M. Aymerich, C. Bao-Varela, M. T. Flores-Arias, E. López-Lago, M. J. Pérez-Comeñas, and E. Calvo, Una física en cada cole, *XXXVI Bienal del Física*, 17-21 July 2017, Santiago de Compostela (Spain).

- M. Aymerich, M. T. Flores-Arias, C. Molpeceres, D. Canteli, and J. R. Vázquez de Aldana, Comparison among microchannels fabricated by nano, pico and femtosecond-laser technologies for microfluidic applications, *OSA Frontiers in Optics Laser Science (FiO/LS)*, 17-21 September 2017, Washington (USA).

- M. Aymerich, E. Álvarez, D. Nieto, and M. T. Flores-Arias, Microestructurado de materiales biocompatibles con láser basado en el efecto Talbot, *XIII Jornadas de Procesado de Materiales con Tecnología Láser*, 19-20 October 2017, O Porriño (Spain).

- M. Aymerich, D. Canteli, C. Molpeceres, J. R. Vázquez de Aldana, and M. T. Flores-Arias, Microchannels devices fabricated on soda-lime by laser technologies, *Ultrafast Science and Technology Spain (USTS 2017)*, 22-24 November 2017, Salamanca (Spain).

- M. Aymerich, E. Álvarez, C. Bao-Varela, I. Moscoso, J. R. González-Juanatey, and M. T. Flores-Arias, Fabrication technique of blood vessel like preclinical devices by laser technologies, *SelectBio Lab-on-a-chip and Microfluidics Europe*, 5-6 June 2018, Rotterdam (Netherlands).

- A. Otero-Cacho, M. Aymerich, M. T. Flores-Arias, M. Abal, E. Álvarez, P. Taboada, A. P. Muñuzuri, and V. Pérez-Muñuzuri, Experimental and CFD numerical simulations of stenosis and atherosclerosis occuring in vessel branches, *SelectBio Lab-on-a-chip and Microfluidics Europe*, 5-6 June 2018, Rotterdam (Netherlands).

- M. Aymerich, G. Frigentti, D. Farnesi, A. Cosci, M. Cerminara, S. Pelli, G. C. Righini, G. Nunzi Conti, M. T. Flores-Arias, and S. Soria, Microbubble and disc resonators as physical sensors, *Advanced Photonics Congress*, 2-5 July 2018, Zurich (Switzerland).

- M. Aymerich, F. Cambronero, A. L. Aragón, M. Blanco, D. Rodríguez, A. Amorín, S. Williamson, S. López, V. Mieites, C. Bao-Varela, and M. T. Flores-Arias, Actividades realizadas por el grupo USC-OSAUSC-EPS para acercar la óptica yla fotónica a nuestra sociedad, *XII Reunión Nacional de Óptica*, 3-7 July 2018, Castellón (Spain).

- M. Aymerich, D. Canteli, J. R. Vázquez de Aldana, C. Molpeceres, and M. T. Flores-Arias, Fabrication of microhannels over soda-lime glass by laser direct writing in the IR spectral range: comparison among nano, pico and femtosecond temporal regimes, *XII Reunión Nacional de Óptica*, 3-7 July 2018, Castellón (Spain). Prize for best student oral contribution.

- A. Otero-Cacho, M. Aymerich, M. T. Flores-Arias, M. Abal, E. Álvarez, P. Taboada, A. P. Muñuzuri, and V. Pérez-Muñuzuri, Experimental and CFD numerical simulations of stenosis and atherosclerosis occuring in vessel branches, *11th European Conference on Mathematical and Theoretical Biology*, 23-27 July, 2018, Lisbon (Portugal).